RARE-EARTH DOPED YTTRIUM ALUMINUM GARNET SINGLE CRYSTAL FIBERS FOR HIGH POWER LASER APPLICATIONS

by

SUBHABRATA BERA

A dissertation submitted to the

School of Graduate Studies

Rutgers, The State University of New Jersey

In partial fulfillment of the requirements

For the degree of

Doctor of Philosophy

Graduate Program in Materials Science and Engineering

Written under the direction of

James A. Harrington

And approved by

_____

_____

_____

_____

_____

New Brunswick, New Jersey

May, 2018

ABSTRACT OF THE DISSERTATION

Rare-Earth Doped Yttrium Aluminum Garnet Single Crystal Fibers for High Power Laser Applications

By SUBHABRATA BERA

Dissertation Director:

James A. Harrington

Single crystal (SC) fibers provide an interesting alternative to conventional glass fibers for high power laser applications. The limitations in power scaling in silica glass fibers arising from thermal lensing, onset of nonlinear phenomena, thermal shock and degradation of the fiber core, etc. hinder performance at high power densities. Since most of these are related to the amorphous structure of the silica glass in the active fiber gain medium, there has been a considerable push to move the fiber laser architecture to a crystalline material. High thermal conductivity and low nonlinear gain coefficients of the crystalline material, along with the high surface-area-to-volume ratio of the fiber geometry make yttrium aluminum garnet (YAG) SC fibers suitable for application involving high optical power density. The work presented in this dissertation discusses the growth and characterization of different YAG SC fibers grown by the laser heated pedestal growth technique.

While SC fibers have theoretically been shown to have high power handling capabilities, in reality their application in practical devices has been severely limited by the high transmission losses involved in such waveguides. In this work, transmission losses in coil-able YAG SC fibers have been lowered to less than 0.8 dB/m at 1064 nm by optimizing growth conditions and fine-tuning the alignment of the optical components of the growth apparatus.

One of the major obstacles in the development of SC fibers as effective laser medium is the difficulty in fabricating a core-clad structure like conventional glass fibers. Since SC fibers are grown from a melt, which is a true liquid, no cross-sectional geometry can be transferred from the preform to the final fiber. A few approaches to cladding have been discussed, including both post-cladding and in-situ cladding. Post-cladding techniques like sol-gel cladding, liquid phase deposition, and hydrothermal crystal growth have been explored. Among in-situ approaches, controlled radial distribution of dopant ions has been investigated as potential route to achieve a graded index profile. Er:YAG SC fibers from rod-in-tube preforms have been grown and the dopant distribution has been studied as a function of growth speed. Radial self-segregation of ions was also explored as a potential means to achieve an in-situ cladding. Such behavior of Nd ions in Nd:YAG SC fibers have been observed and reported.

A sol-gel-based low-cost approach has been developed to vary the dopant concentration of YAG SC fibers. Using this technique Ho:YAG SC fibers of varying dopant concentration were grown and lasing was reported at 2090 nm. A maximum optical-to-optical slope efficiency of 58.5% was demonstrated in such fibers.

Finally, the crystal quality of the YAG SC fibers was characterized by synchrotron white beam X-ray topography. This non-destructive characterization technique for large single crystal samples allowed the study of the strain and defect distribution of different YAG SC fibers.

Acknowledgements

During my time as a graduate student at Rutgers University, I had the opportunity to work with and learn from so many wonderful individuals. First and foremost, I would like to express my sincerest gratitude to my PhD supervisor Prof. James A. Harrington, for being a great guide and helping me realize my love for research. It was a real honor and privilege working for an amazing person and expert professional like you. I would like to thank my dissertation committee members at the Materials Science and Engineering Department, Prof. Lisa Klein, Prof. John Matthewson and Prof. Deirdre O'Carroll, for your valuable advice and inputs to my research. Large thanks to Prof. Eric Johnson from Clemson University for your expert contribution to the single crystal fiber laser project and for taking the time off to review my written dissertation.

I would like to acknowledge the contribution from all my colleagues in the Fiber Optics group: Dr. Craig Nie, Jeffrey Melzer, Carlos Bledt III and Michael Soskind. It was a great experience working with you in doing this research. In particular, I have to appreciate the impact of Dr. Nie, working with him was one of the joys of graduate school.

This project was a highly collaborative effort and I was very fortunate to work with some highly talented and motivated people during its time. Dr. Yuan Li and Prof. Eric Johnson from Clemson University, for the amazing efforts with the lasing experiments; Long Cheng, Theresa Chick, and Prof. Stephen Rand from University

of Michigan, for the excellent work with the modeling and fluorescence measurements; Dr. Balaji Raghothamachar from Stony Brook University, for your expert work on X-ray topography; Brad Stradelman and Prof. Joseph Kolis, for your innovative work on hydrothermal cladding; Dr. Thomas Emge from Rutgers University, for you detailed work on single-crystal diffraction; Dr. Juliane Gross from Rutgers University, for your work on Electron Probe Micro-Analysis: I would like to thank you all for making this project such an enjoyable learning experience for me.

In my four-and-half years at Rutgers, I have met some really special people who have made this time one of the best periods of my life. Rahul, Nick, Ross, Ajay, Shawn, and Craig, thank you for making life as a graduate student so enjoyable ! Thanks also to my close friends from school and college, who despite the distance and time-difference, have been there with me through my ups and downs.

And lastly, and mostly importantly, I would like to thank my family for your love, support and encouragement. Dada, Ma, and Baba, everything I am today, I owe it to you. Thank you for teaching me, inspiring me and being there for me when I needed the support. I am truly blessed to be able to call you family.

List of Abbreviations

AFM: atomic force microscopy

AR: anti-reflective

ASB: aluminum *sec*-butoxide

CCD: charge-coupled device

CDLHPG: co-drawing laser heated pedestal growth

CVD: chemical vapor deposition

cw: continuous-wave

EFG: edge-defined film-fed growth

EPMA: electron probe micro-analysis

FWHM: full with at half maximum

HR: high reflective

HoAG: holmium aluminum garnet

IR: infrared

LHPG: laser heated pedestal growth

LPD: liquid phase deposition

LPE: liquid phase epitaxy

NA: numerical aperture

NIR: near infrared

OVD: outside vapor deposition

PID: proportional integral differential

PVA: poly-vinyl alcohol

RE: rare-earth

RiT: rod-in-tube

SBS: stimulated Brillouin scattering

SC: single-crystal

SEM: scanning electron microscope

SRS: stimulated Raman scattering

SWBXT: synchrotron white-beam x-ray topography

TEM_{00}: fundamental transverse electromagnetic mode

UV: ultraviolet

YAG: yttrium aluminum garnet

α_t: total loss coefficient

α_s: scattering loss coefficient

μ-PD: micro pulling-down

Contents

List of Figures

List of Tables

Part I

Introduction

Chapter 1

Motivation

Since the invention of lasers in the 1960s, a staggering amount of research has been done on near infrared laser sources. Demands in different applications such as medical surgery [1], remote sensing [2], free space communication [3], telecommunication [4], lidar systems [5], etc. in the 0.9-3.0 μm range have led to an explosive growth in the lasers operating in this range. While quite a few different types of lasers cater to this wavelength range, the most common type are rare-earth (RE) doped solid state lasers. These lasers are based on *4f-4f* transitions in RE ions which typically produce emission lines in the short wave infrared region. A wide range of crystals, ceramic materials and glasses are used as host matrix for such laser systems. Among these, RE doped glass fiber lasers have seen a lot of development over the last five decades. Fiber lasers are solid-state lasers which use a double-clad glass fiber doped with trivalent RE ions as their gain medium. A fiber based gain medium provides a number of special qualities that are very attractive for certain applications. For fiber lasers, the laser resonator can be built entirely out of fiber components, eliminating the need for free space optical components, and hence allowing the system to be compact and rugged. Laser transitions are strongly broadened in glass hosts, allowing for large gain bandwidths. This, in turn, allows greater wavelength tunability and generation

of ultrashort pulses. Several low phonon energy glasses like fluoride and chalcogenide glasses allow for transmission in the mid infrared region [6]. The strong optical confinement in doped fibers make them high gain media which allows operation even at low pump powers. The high surface-to-volume ratio of the fiber geometry also allows for more efficient extraction of heat, thus allowing operation at high power densities.

At present, almost all RE doped fiber lasers available commercially are glass-based. Fiber lasers can deliver single-mode output with very high output power in either pulsed or cw mode. However, for some military applications requiring output power levels beyond tens of kW in continuous mode or for precision material or plasma processing applications requiring high energy per pulse, the conventional glass fiber laser technology is not suitable due to limitations inherent in the material properties of the glasses used to make the fiber gain media. At such high operating powers, high power density in the fibers can limit their performance. Limitations to power scaling in glass fibers arise from thermal self-focusing, nonlinear effects, facet damage etc.

As operating power of a laser increases, loss mechanisms generate heat in the gain medium. For solid state gain media, the absence of an effective heat extraction mechanism, leads to the generation of a thermal gradient in the medium. The thermal gradient, in turn, creates thermal stresses in the medium. High operating powers can exaggerate the effects of thermal stress and lead to catastrophic thermal fracture of the gain medium. For glass fiber gain media, in extreme cases, the heat can cause the melting of the fiber core. Heating of the solid-state gain medium can also lead to thermal lensing [7]. The temperature gradient across the fiber cross-section sets up transverse refractive index gradient across the fiber. This thermally induced refractive index gradient competes with the refractive index profile of the fiber and affects waveguiding of the medium. High optical power associated with both pump and laser wavelengths can also lead to loss of power by nonlinear phenomena.

Processes like stimulated Brillouin scattering (SBS) and stimulated Raman scattering (SRS) can limit the continuous power handling capability of a medium and give rise to a power dependent loss mechanism [8]. Lasers operating over narrow spectral lines are limited by SBS, while lasers with broad bandwidth are limited by SRS [9]. Especially for amorphous media like silica, the backward propagating wave gives rise to a considerable SBS derived loss at high power.

Although the output power of the fiber lasers can be maximized by tuning fiber parameters like length, dopant concentration, and mode area, it is ultimately limited by the material properties of the glass fiber. Limitations of the glass fiber architecture have shifted the focus of the research to develop new materials for active fiber applications.

Crystalline materials are another class of laser host materials that have been particularly well studied. Over the years, a huge number of crystals have been grown and used as host materials for solid-state lasers. These crystals have included different classes of materials, including oxides, halides and chalcogenides, etc. Excellent power handling capabilities of doped single-crystal (SC) like Ti:sapphire [10], Nd:YAG [11], etc have been well-documented. Thermal conductivities of amorphous substances are generally lower than that of crystalline substances as heat transport in such substances are affected by elastic scattering of phonons at lattice imperfections. Since glasses lack any long-range lattice ordering, the phonon mean free path in such substances is smaller compared to that in crystals, leading to lower thermal conductivity. Among crystalline materials, the absence of grain boundaries in SC fibers result in longer phonon mean free paths and hence higher thermal conductivity. A higher value of thermal conductivity would result in better dissipation of heat from the gain medium. This, in turn, would mitigate the limitations on power scaling arising from thermal effects. The long-range ordering in crystals also effect the nonlinear scattering thresholds in the media. Both SBS and SRS gain coefficients in crystals are a few

orders of magnitude less than in glasses.

Oxides crystals like garnets [12], perovskites [13], sesquioxides [14], vanadates [15], tungstates [16], etc. have especially been subject to extensive research due to their versatile properties and ease of processing. Among these, the most studied group of laser crystals are perhaps the garnet crystals. While crystals of the garnet structure exist naturally, our knowledge of these crystals have been greatly enhanced due to the emergence of various synthetic garnet crystals. Yttrium aluminum garnet ($Y_3Al_5O_{12}$, YAG) has been particularly well studied due to its excellent optical properties. The garnet structure can accommodate a large variety of cations in its different cation sites. In the dodecahedral or *c*-sites, the Y^{3+} ions in YAG can be easily substituted to a varying degree by trivalent RE ions, leading to its use as a laser host material. YAG has a broad transmission window from the UV to mid IR (about 210 nm to 5.5 μm). It is mechanically tough, chemically stable and thermally durable. Being isotropic and congruent melting, it is relatively straight-forward to grow SC YAG from a melt. Additionally, YAG has low nonlinear scattering (SBS and SRS) coefficients and better thermo-mechanical properties compared to glass laser hosts. Its high thermal conductivity, melting point, and low thermo-elastic coefficients make it ideal for handling high power densities associated with high power lasers. A comparison of the different properties of YAG and silica glass is given in Table 1 [17].

	Transmission Range (μm)	**T_p (℃)**	**Thermal conductivity (W/mK)**	**Young's Modulus (GPa)**	**Hardness (kg/mm²)**	**Refractive index @1.06 μm**	**SBS Gain Coefficient (m/W)**
Silica glass	0.18-2.2	1000	1.38	73	500	1.45	5×10^{-11}
YAG	0.21-5.5	1940	10	300	1350	1.81	$<1 \times 10^{-13}$

Table 1.1: Comparison of different properties between silica glass and YAG. [17]

However, despite their better thermal conductivity, solid-state crystal lasers have

a serious challenge of managing heat dissipation at high power density. This problem can be addressed by modifying the geometry of the crystal to increase the surface-to-volume ratio for improved heat extraction. Thin disk lasers [18] and slab lasers [19] are two configurations that have been developed to overcome the thermal limitations. Although these systems can be designed for high output power, often of the order of kilowatts, they are relatively complex, using complicated multi-pass systems or beam shaping schemes. An alternative to these configurations is growing the crystalline host material in the form of a fiber. Not only does the cylindrical geometry provide a better surface-to-volume ratio for enhanced cooling, it also provides tighter optical confinement for better interaction of the pump beam with the lasing ions in the host. The fiber laser medium is relative straightforward to pump and produces output beams of high quality without the need of sophisticated beam shaping arrangements. Another advantage the fiber geometry offers is that the pump spot size and device length are truly independent. This allows the freedom to vary doping concentration and device length while still keeping the lasing output same. Hence, there has been a resurgence in the research on doped crystal fibers as potential high-power laser gain medium.

The origins of the growth of SC fibers can be traced back to the late 1950s when these materials were investigated for their mechanical properties. Compared to bulk crystals, SC fibers could be grown with a very high degree of crystallinity, leading researchers to explore the relations between crystalline purity and superior mechanical behavior. Interest was driven by the possibility of using these fibers to strengthen composite mechanical structures. However, a limited interest in the subsequent years led to a temporary decline in the 1960s. But the field saw a resurgence in the early 1970s when Haggerty *et al.* [20] developed the first micro-float zone apparatus for the growth of SC fibers. This technique would serve as the precursor to the laser heated pedestal growth (LHPG) technique, which even now is one of the most widely

used crystal fiber growth techniques. Using this set-up Haggerty and colleagues grew oxide crystal fibers to study their mechanical properties. It was during this period that Burrus and Stone adapted this technique to grow the first optical crystal fibers. They were able to grow Nd:YAG crystals in the form of fibers and demonstrate lasing [21]. However, it wasn't until the early 1980s, that SC fibers received widespread research attention. Feigelson, Fejer and others at Stanford led a comprehensive study into the exploration of potential applications of SC fibers for passive, active and nonlinear applications, in the process establishing much that we now know about these materials [22] [23].

In its early stages, most of the research on optical applications of SC fibers was focused towards the development of laser power delivery systems. Sapphire SC fibers were grown for the delivery of Er:YAG laser radiation at 2.94 μm for medical applications [24]. However, the use of such an architecture never caught on and by the early 2000s, the focus was shifted to the growth of RE doped YAG SC fibers for laser applications. The SC fiber provided a hybrid laser architecture between bulk crystals and active fibers, allowing higher average powers than with conventional crystals and higher energy than with fibers in pulsed regime. The four-level laser system of Nd:YAG, being previously very well established for bulk crystal was the first system to be studied in the SC fiber geometry [25]. In the following years, numerous research groups have investigated YAG SC fibers doped with various lasing ions like erbium [26], ytterbium [27], holmium [28], thulium, chromium [29], etc.

Dawson *et al.* [30] and Parthasarathy *et al.* [17] have discussed the effect of different factors that limit the maximum cw output power of fiber lasers. There are seven physical limits to the power scaling in fiber lasers. These are thermal fracture, melting, thermal lensing, optical damage, pump-power limitations, and nonlinear scattering. Based on these physical limits, contour plots of output power were constructed for different materials. In both studies, the authors found that the maximum power

that can be obtained from a YAG-based fiber laser is about one order of magnitude more than that of conventional silica-glass based fiber lasers. The results obtained by Dawson *et al.* [31] are shown in Fig. 1.1. It can be seen that under a single frequency cw operation, the maximum output power of a Yb:YAG fiber laser is 16.9 kW compared to 1.89 kW obtained from a Yb doped silica fiber.

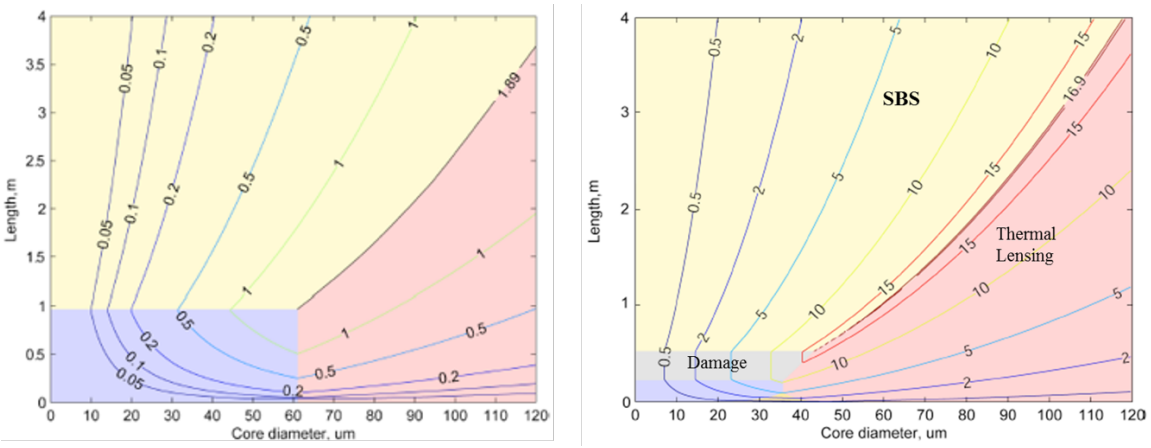

Figure 1.1: Maximum output power from silica glass fiber laser (left) vs YAG fiber laser (right). (Reprinted with permission) [31]

However, despite the promising figures, at present the maximum output power of single-crystal based fiber laser is much lower than that of glass fiber lasers. While the most advanced commercially available glass-based fiber lasers routinely produce output powers above 1 kW, the maximum output of SC fibers have not exceeded a few hundred watts [32]. Two major obstacles in scaling up the power of crystal-based fiber lasers are the high propagation losses and the absence of a proper cladding.

Conventional glass fiber fibers have benefitted tremendously from the development of low-loss silica glass fibers for long-haul optical communication. Demand for low-loss fibers for fiber optic communications networks has produced extensive research in this domain [33]. Current commercial optical fibers have a loss of less than 0.2 dB/km at 1.55 μm, which is less than 1 dB/km at 1 μm [34]. At such low numbers, background losses can be, for all practical purposes, ignored when fabricating a laser device. On the other hand, the total attenuation losses in crystal fibers had been

reported to be much higher, of the order of a few tens of dB/m [35]. At such losses, a considerable amount of pump and laser power is lost as heat, severely limiting the power output of these lasers. Thus, lowering the attenuation losses in crystal fibers is a major hurdle that needs to be overcome if crystal based fiber lasers are to be practically realized.

The total attenuation losses through a waveguide are a combination of both intrinsic and extrinsic losses. The intrinsic losses are inherent in a material and are unavoidable due to its fundamental properties. On the other hand, extrinsic losses are introduced during fabrication and can be reduced by refining the processing techniques. The presence of defects and contaminants in the bulk of the crystal can lead to absorption or scattering of propagating light. Extrinsic losses also originate from waveguide losses which result from imperfections in the fiber geometry. A major focus of the work presented in this dissertation is on the reduction of extrinsic losses in the SC fiber waveguides by improving the processing techniques.

In order to preserve the output beam quality without sacrificing higher pumping power, fiber lasers use fiber with a double clad structure. The cladding helps lower the scattering losses at the fiber surface by modifying the critical angle for the total internal reflection. Hence it is desirable to have a small core diameter fiber with a thick inner cladding. However, SCFs are grown without cladding and putting a cladding on them is much more difficult than that in glass fibers. The melt from which the fiber is drawn is a true liquid which has very low viscosity and it is very difficult to maintain and transfer a pre-defined core-cladding structure from a preform to the final fiber. Glasses have been explored, to limited success, as potential cladding materials for crystal fibers. However, glasses and crystals are fundamentally different classes of materials and have vastly different thermal and mechanical properties. For high power applications, these differences are exaggerated and lead to significant losses and ultimately catastrophic device failure. To preserve the homogeneity of material

and exploit the advantages of a crystalline phase, our attention in this work has been restricted to growing a crystalline cladding only.

Part II

Background and Theory

Chapter 2

Crystal Growth from Melt

The rise of instrumentation technology in the early and mid-20th century has moved crystal growth from the realm of artistry and jewelry to an active area of research. Newer synthetic crystals have been developed for applications ranging from electronics, optics to electrical, magnetic and radiation-based devices. As the demand for high quality defect free crystals with tailored shapes, sizes and morphology grew, crystal growth transformed into a multi-disciplinary field of research, driven by scientific principles.

Essentially crystal growth is the science and engineering of the transformation and evolution of a solid phase from either a solid, liquid or gas phase. While crystal growth from solid is quite rare, crystal growth from liquid and gas phases are rather common and have very well studied throughout the last century. Between these two, liquid based crystal growth is the most popular and widely investigated. All crystal growth from liquids are comprised of essentially the same three steps. The first step involves the supercooling or supersaturation of the liquid phase, followed by nucleation which can be either spontaneous or stimulated. The final stage is the growth of the crystals at the nucleated sites. Depending on the number of phases in the liquid stage, liquid based crystal growth techniques are of two major categories.

In solution growth, the chemical component for the desired crystal is dissolved in a liquid medium, either aqueous or flux, and the crystal growth is triggered by supersaturation of the solution. Growth from melt, on the other hand, is accomplished by supercooling the liquid phase of a material to initiate crystal growth.

Between these two approaches, growth from melt is more widely practiced. Large crystals with desired orientation and morphology can be grown at high growth rates in a relatively straightforward manner by employing high temperature. The melt is usually solidified by carefully manipulating the temperature. In most cases, a seed crystal is used to obtain a crystal with some desired orientation. Based on the phase diagram of the material, it is very important to carefully consider the thermodynamics of the growth process to grow high quality single crystals. For a crystal to be grown successfully from a melt, the material has to follow certain restrictions.

- The material should be congruent melting.
- It should not have a polymorphic phase transition between the crystallization temperature and the melt temperature.
- The material should not decompose before it reaches its melting point.
- It is also required that the material should have a low vapor pressure at its melting point.

If all these criteria are not simultaneously satisfied, other crystal growing techniques need to be explored.

Despite these restrictions, growth from melt is the most popular form of crystal growth, accounting to almost half of the technologically important crystal grown this way. There is a wide variety of melt-based crystal growth techniques at present and the choice of the particular technique depends on the physical and chemical properties of the material being grown and shape dimension of the crystal that is

sought. Among these numerous techniques we will discuss the basics of a few crystal pulling techniques. These techniques involve the growth of usually axisymmetric quasi-unidimensional crystals whose size in the other dimensions can be controlled. Since the crystals are drawn from a melt, the formed crystal is not in contact with the crucible. This reduces the possibility of contamination from the crucible and also the stress introduced due to solidification on another surface (as in Bridgman growth).

The Czochralski method of crystal growth is named after Polish chemist Jan Czochralski who developed this process in 1917. It is a versatile technique by which single crystals of semiconductors, metals, salts and oxides can be grown from a molten charge [36]. A typical Czochralski growth apparatus, as shown is Fig. 2.1, consists of a crucible housing the molten material and a seed pulling mechanism. The seed is placed along the vertical symmetry axis of the crucible. At initiation of growth, the seed is dipped into the molten charge. Due to surface tension of the melt, it forms a meniscus at the contact of the seed. The seed is then slowly drawn up, carefully controlling its speed, in the process forming a crystal. In order to homogenize the heat distribution about the grown crystal, the seed is also rotated axially as it is drawn up. The uniform heating of the molten zone is a major factor for this growth method as convectional currents in the melt give rise to stress and related defects in the crystal. Hence, to mitigate this issue, some Czochralski growth apparatus have been modified to have the crucible rotate about its symmetry axis.

The skull melting technique and the closely related cold crucible technique were developed independently by French and Russian scientists in the 1960s for the growth of refractory materials. In this technique, only the center of a charge in a crucible is melted using radio-frequency heating while the material in contact with the crucible remains solid due to cooling of the crucible walls [38]. In this manner the melt is housed in its own crucible and does not come in contact with the original crucible material. The skull is the solid layer of the material that forms a boundary between

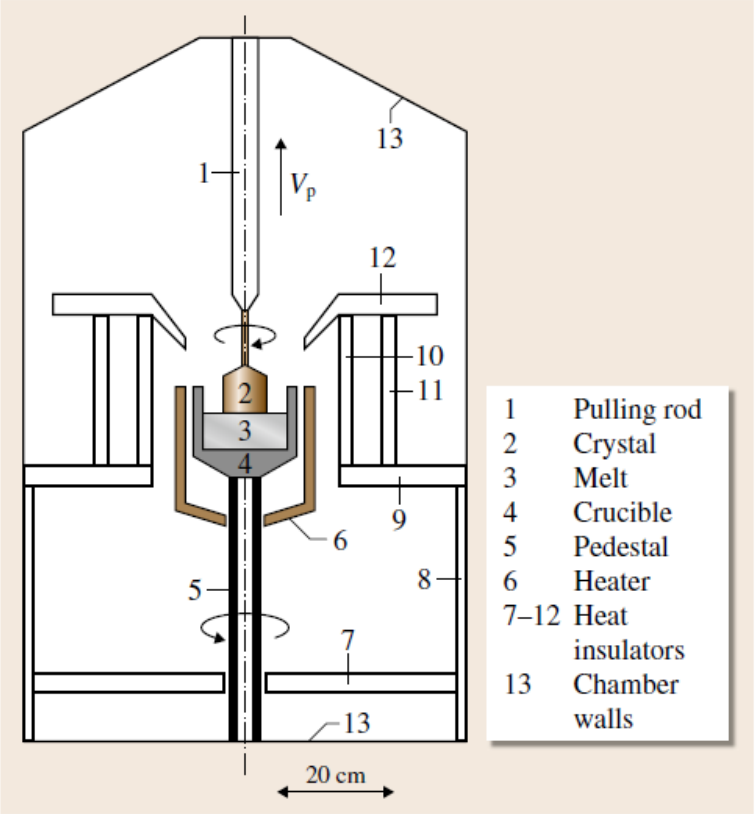

Figure 2.1: Typical geometry of a Czochralski growth apparatus for growing silicon. Adapted from [37]. (Reprinted with permission)

the melt and the crucible. This technique allows for the growth of ultra-pure single crystals by virtue of this principle. Due to this aspect, some researchers have modified the skull melting technique to allow for the growth of pulled fibers in a process not very dissimilar from the Czochralski method. A schematic of such an apparatus is shown in Fig. 2.2. Despite of the interest in growth of pulled fibers using skull melting technique, it is associated with a number of challenges. The most important among of these issues is the homogeneity of the heat distribution in the melt. The isotherm patterns at the surface of the melt control the quality of the pulled single crystal. In skull melting technique, obtaining a highly axi-symmetric heat distribution by optimizing the positions of the radio-frequency heating elements, hence pulling crystal fibers, making crystal pulling really challenging.

The Verneuil process is the oldest commercial crystal growth technique, developed

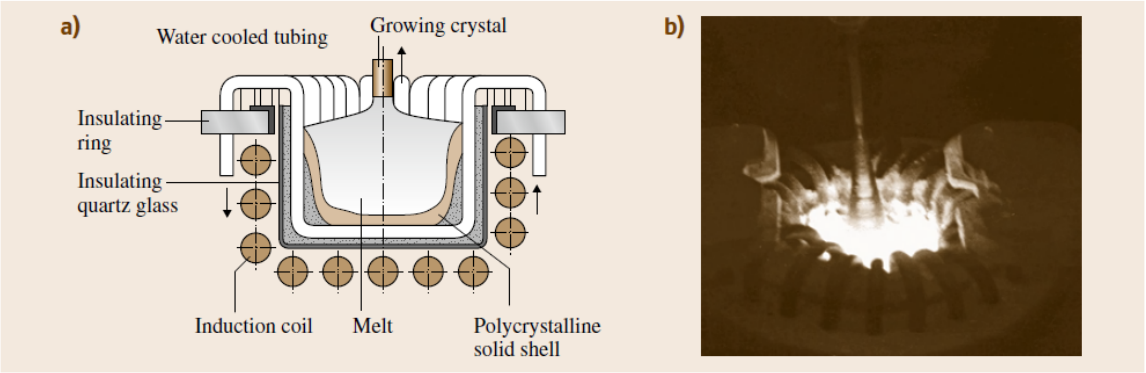

Figure 2.2: a) Typical geometry of a skull melting apparatus for growing Al_2O_3. b) Actual photograph of crystal growth by skull-melting. Adapted from [38]. (Reprinted with permission)

by French chemist Auguste Verneuil in the late 19th century. In a typical Verneuil set-up, as shown in Fig. 2.3, the charge is allowed to fall onto a seed crystal through an oxy-hydrogen flame. The charge is introduced using a vibrating hopper to ensure its continuous flow. The exit orifice of the hopper has to be not too small to restrict free flowing of the charge but not too big to allow incomplete fusion of the charge as it falls through the flame. The seed at the bottom is often rotated to obtain an axi-symmetric growth. Although it is not technically a crystal pulling technique, it has most of the characteristics of such a technique. Despite the absence of a crucible, crystals grown by other techniques like Czochralski method produce higher quality crystals [40]. Another downside of this method is that the growth interface cannot be controlled and most often this leads to curved lines of growth and strong faceting.

While the techniques introduced in the few preceding sections discuss different methods of crystal pulling, dimensions of the crystals grown by these techniques do not qualify them as fibers. Fibers are quasi-unidimensional structures very high aspect ratios, characterized by small diameters, in the region of a few tens of microns to a millimeter. Crystals grown by the techniques described previously have diameters ranging from a few centimeters up to about 40-50 centimeters. To grow crystals of smaller diameters, there are two groups of fiber pulling techniques that are used:

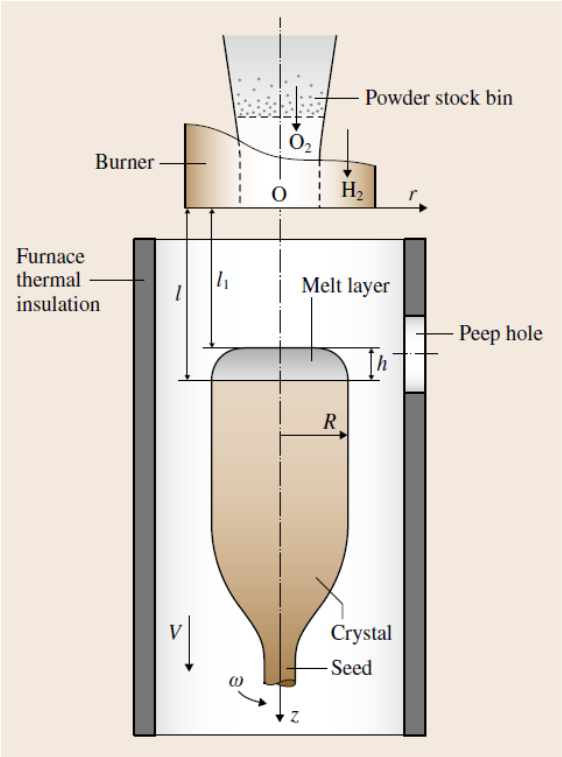

Figure 2.3: Typical geometry of a Verneuil apparatus for growing Al_2O_3. Adapted from [39]. (Reprinted with permission)

a) Unidirectional crystallization by pulling through a die

b) Growth from a floating micro-melt

While the diameter of the crystal grown using by Czochralski method can be varied by changing the crystal pulling parameters, diameters less than a few millimeters cannot be achieved due to some fundamental restrictions imposed by the growth technique itself. Due to the effect of surface tension, convective currents, and temperature oscillation in the melt, small diameter Czochralski growths are inherently very unstable. Under such conditions, stable small diameter growth is possible with the use of die capillaries. Two crystal growing techniques based on the principal of pulling a crystal through a small channel are:

i) Edge-defined Film-fed Growth (EFG)

ii) Micro-pulling Down technique (μ-PD)

In the EFG technique the crystals are drawn from the melt film produced on top of a die capillary. This process was developed to grow thin rods and sheets of materials like germanium, aluminum etc by using a shaping die made of tungsten [41] [42]. In the early 1980s, Saphikon (now Photran) commercialized the growth of sapphire profiles using a floating orifice technique that used a molybdenum shaper. The capillary forces between the solid shaper elements force the melt up through the channels forming shaped liquid columns. As it rises above the top of the shaper elements, it forms a fluid film. When a seed crystal is brought into contact with this liquid film, the wetting properties of the melt help form a column by which the crystal can be grown. A schematic diagram of the EFG technique is shown in Fig. 2.4.

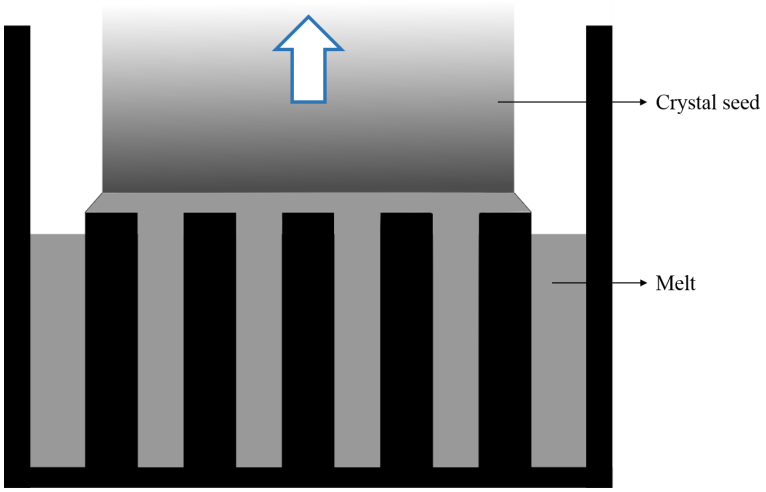

Figure 2.4: A schematic diagram of the EFG technique

However, at present, the EFG procedure has fallen into disuse and is scarcely used to grow crystal fibers and has been replaced by the μ-PD growth technique. In μ-PD growth, fibers are drawn from a melt by drawing it through shaped capillaries at the bottom of the crucible [43] [44]. These shaped capillaries or nozzles allow the transport of the liquid melt to form growth meniscus below the crucible bottom. Under non-growing condition, the liquid does not leak out from the bottom of the crucible through the nozzles, but is rather held inside the crucible by surface tension at the nozzle. However, when a denser body is brought in contact with the crucible

bottom, the melt flow through the micro-channels. As it flows out of the crucible, cooling leads to the growth of columnar crystals from the melt. A schematic of the μ-PD growth technique is shown in Fig. 2.5.

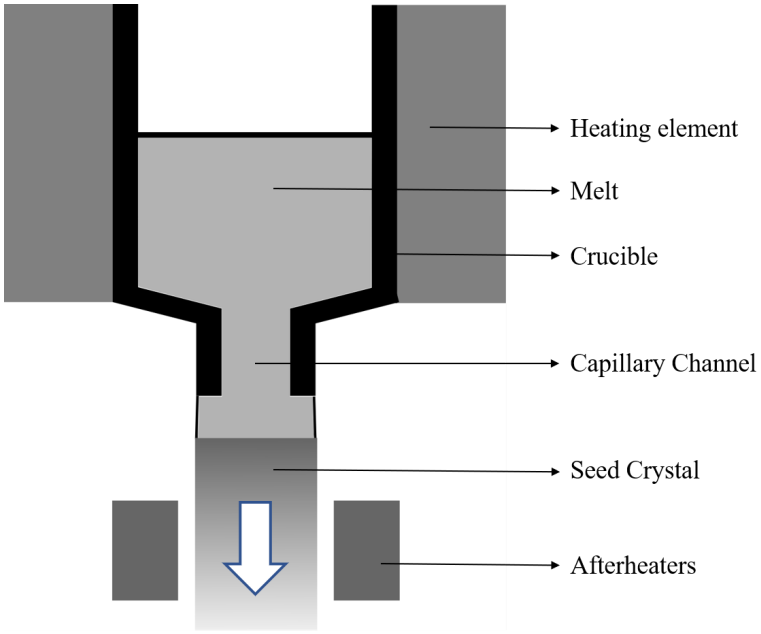

Figure 2.5: A schematic diagram of Micro-pulling down technique

In the μ-PD technique, since the fiber is drawn from the bottom of the crucible, the likelihood of incorporation of bubbles in the crystal is low. However, crystals grown by this technique are susceptible to inclusion of heavier impurities which tend to settle at the bottom of the crucible. The EFG technique is complementary to the μ-PD technique and the crystals grown by this technique are affected by the inclusion of air bubbles but free from heavier impurities. Since both the μ-PD and the EFG techniques involve the pulling of the crystal through a die, both techniques allow for the cross-sectional shape of the crystal to be controlled, allowing for the growth crystals in various forms like tubes, columns, ribbons, etc.

While these techniques allow for the growth of uniform quasi-one-dimensional single crystals with high aspect ratios, fibers with diameters less 500 μm cannot be grown by these methods. The diameter of the crystals grown by the EFG and μ-PD

techniques are limited by surface tension in the die capillary and most of the crystals grown by these techniques are about a millimeter in diameter. However, at these dimensions, the single crystals are closer to being mini-rods rather than being flexible fibers [45] [46]. On the other hand, the diameter of the SC fibers grown by the float-zone techniques can be reduced with each successive growth. SC fibers with diameters less than 100 μm have been grown with consistently good quality with diameters as small as 20 μm being reported in the literature [47].

Additionally, both the EFG and μ-PD techniques use a crucible to house the molten charge. That, along with the presence of the shaper element for EFG introduce a considerable risk of contamination from the refractory materials. The float zone techniques are superior in this regard as they are crucible-less techniques where the heating element does not come in physical contact with the melt.

Compared to crystal growth by pulling through a die, float zone techniques allow for the growth of high quality crystals with very high aspect ratio. In such techniques, a heat source, usually an arc lamp or a laser, is focused on a source material pedestal to form a mini-melt [48] [49]. A seed crystal is dipped into this melt and the crystal is grown by pulling the seed. The focus of the heat source is kept fixed between the source rod and the grown crystal and the growth is achieved by translating the seed and the feedstock. The principal advantage offered by float zone techniques is that the melt does not come in contact with any crucible, hence precluding any possibility of contamination from the crucible material. This enables the growth of crystals of materials which are highly reactive or materials with very high melting point. Figure 2.6 shows a schematic of a Optical Float Zone using halogen lamps as the heat source. Lasers are very useful as heat sources as they can provide small regions of very high energy density for the formation of the melt. The first usage of laser in an optical float-zone technique was demonstrated by Haggerty in 1972 who used two focused laser beams to create a mini-melt and draw SC fibers of materials like aluminum oxide,

yttrium oxide, etc [20]. Since then, this technique has been modified by different researchers, adapting it to grow crystal fibers of a wide range of materials, including semiconductors, inter-metallic and inorganic compounds, refractory materials, and oxides.

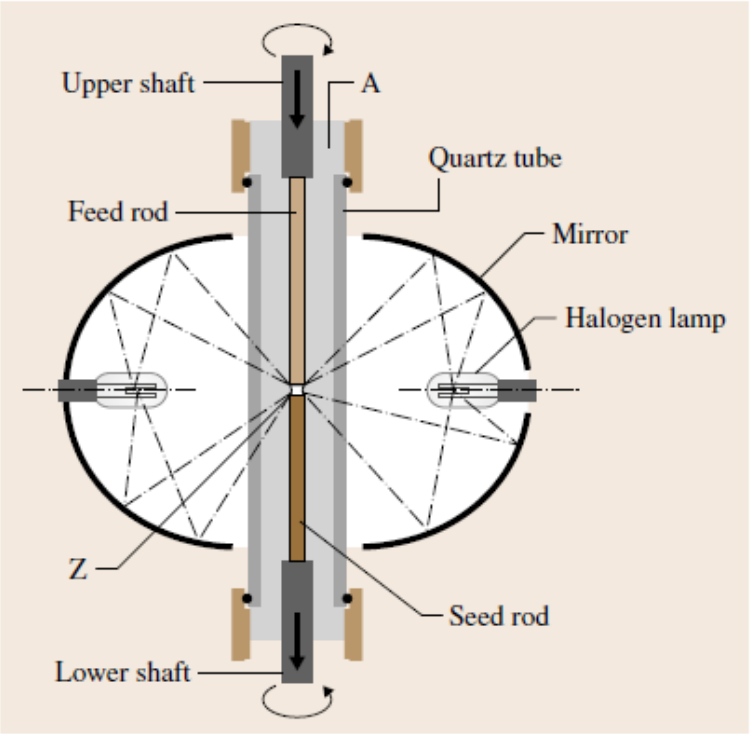

Figure 2.6: A schematic diagram of Optical Float Zone technique. (A - Atmosphere, Z - Zone) Adapted from [50]. (Reprinted with permission)

Chapter 3

Attenuation Losses in Crystal Fibers

Given their excellent material characteristics, SC fibers have great potential as laser gain medium for high power applications. However, despite the promise, the SC fiber architecture has not been widely adopted for practical application. The main obstacle that has prevented the development of this technology is the very high transmission losses in SC fibers. The development of silica based glass fiber lasers have benefitted tremendously from the advancement of silica optical fiber processing in the 1970s and 80s. During this period, the extensive research capital invested in the development of low-loss silica glass fibers for long haul telecommunication had indirectly aided the growth of all glass fiber based technologies. Fiber losses have been reduced from more than 20 dB/km in 1970 to less than 0.5 dB/km in the currently available commercial single mode fibers [34]. Compared to that number, at present, the very best YAG SC fiber waveguides have a transmission loss of about 0.1 dB/m [51]. Hence to make SC based fiber devices a realizable technology, it is very important to refine processing techniques to reduce the losses in such waveguides. For that, it is very important to understand the origin of these losses so that steps have been taken to address them.

The losses in any waveguide are a combination of intrinsic losses and extrinsic losses. Intrinsic losses arise from the material properties of the waveguide material and cannot be affected by processing improvements. Once a material has been chosen, the losses in the waveguide can only be reduced by reducing the extrinsic losses. These losses can arise from a variety of different factors like impurities in the material and imperfections in the crystal and waveguide. Before discussing these extrinsic loss mechanisms, it is worth taking a look at the fundamental loss mechanisms in SC fiber waveguides.

3.1 Intrinsic Loss mechanisms

The intrinsic losses in a material originate from different absorption and scattering mechanisms that exist in a perfect sample of a pure substances. These losses represent the minimum loss that can be achieved in a particular material. For any dielectric material, the intrinsic losses arise from absorption in the ultraviolet and infrared regions and scattering in the intermediate region. These mechanisms can be expressed in a combined form in the following equation [52]

$$\alpha_t = Ae^{a/\lambda} + B/\lambda^4 + Ce^{-c/\lambda} \tag{3.1}$$

The first term describes the optical absorption at short wavelengths, in the UV region. Such a process is a result of photon absorption due to electronic or excitonic transitions, when the energy of the photon is of the order of the bandgap of the material. When the photon energy is greater than the bandgap of the material, the light is absorbed, leading to absorption near the bandgap of the material. This phenomenon provides the lower limit of the wavelengths that can transmit through material and produces what is called the Urbach tail of absorption at short wavelengths.

The second term arises from the scattering of photons in a medium. If the scat-

tering is an elastic process, it is Rayleigh scattering; while if it is an inelastic process, it is Brillouin scattering. While both Rayleigh and Brillouin scattering occur due to fluctuations in the density, composition and orientation of molecules within the transmitting medium, Rayleigh scattering involves random incoherent fluctuations. For this reason, in crystals having perfect long-range ordering demonstrate no Rayleigh scattering and the transmission in such materials is limited by Brillouin scattering. The periodic ordering of the lattice in crystals scatters photons by low frequency phonons. Despite their predominance in different classes of materials, both Rayleigh and Brillouin scattering show the same dependence on wavelength.

The third and final term in the intrinsic loss mechanism is due to multiphonon absorption in the infrared. The strong absorption at lower frequencies arises from the coupling of photons to the lattice vibration. If the photon energy is low enough, the lattice can absorb it and create one or more phonons. The coupling of the phonons with the transverse optical vibration modes of the lattice is very strong and effectively limits transmission through the material.

3.2 Extrinsic Loss Mechanisms

In practice, the losses measured in almost all materials is much higher than the limits imposed by intrinsic loss mechanisms. For all practical purposes the losses that are measured for different materials result from extrinsic losses in the medium. These result from different aspects of material processing and can be greatly reduced by improving and optimizing processing techniques. Extrinsic losses in waveguides can be broadly characterized into two broad categories, absorption and scattering. Extrinsic absorption losses are due to the presence of impurities in the material. These impurities can be transition metals, RE metals or water related impurities and can be easily identified by their characteristic absorption peaks. In general, for crystal fiber

waveguides, the main impurities are metallic in nature and are mostly incorporated from the source material. Apart from the starting material, contamination may occur from the melt crucible, growth atmosphere etc. While it is possible to reduce the amount of impurities by optimizing procedures like starting with ultra-pure source bars, using crucible-less growth techniques and growing in cleanroom environment, it is almost impossible to entirely eliminate this problem.

The major contribution to extrinsic losses comes from scattering losses. These losses which include scattering from defects, dislocations, micro-bubbles, localized strain fields, and waveguide imperfections can be mostly eliminated by refining waveguide fabricating procedures. These scattering centers cause light to be coupled into lossy higher order modes which subsequently leak out of the waveguide.

In general, the extrinsic scattering losses in a sample assumes the form [52]

$$\alpha_{sc} = A + \frac{B}{\lambda^2} + \frac{C}{\lambda^4} \tag{3.2}$$

The first term on the right-hand side is a wavelength independent phenomenon called anomalous diffraction, which arises from scattering centers that are large compared to the wavelength and introduce a large phase difference. It takes place due to coherent interference of light scattered from all volume elements of the scattering center. The second term is due to Rayleigh-Gans scattering which occurs due to scattering centers that are large compared to the optical wavelength but contribute small phase differences. Scattering occurs predominantly due to local fluctuation in refractive index [53]. These can be induced by stress, voids, dislocations, micropores, grain boundaries, etc. In this regime of scattering, light is coupled into neighboring modes and eventually into higher order modes. Since higher order modes have higher losses, Rayleigh-Gans scattering increases losses in fiber; increasing the value of α_{total} with the length of the fiber. Rayleigh Gans scattering is also characterized by strong

scattering in the forward direction. This forward scattering also contributes strongly to the length dependence of the total losses. The final term is due to Rayleigh scattering. It occurs due to scattering centers which are small compared to the wavelength. In practice for most SC fibers, the contribution from this mechanism is smaller compared to the other two mechanisms and only plays a significant role for fibers with exceptionally good optical quality.

A major factor affecting the attenuation losses in fibers is waveguide imperfections and non-uniformities. Waveguide imperfections can be in the form of microbends, diameter fluctuations, waveguide surface imperfections etc. Fluctuations in waveguide diameter and imperfections of the fiber surface lead to significant deviations from the axisymmetric propagation of meridional rays and gives rise to skew rays. Due to their highly asymmetric propagation, these rays have a high tendency to leak out of the waveguide. Such propagation also leads to redistribution of power among different modes propagating in the fiber and ultimately power is lost via radiation. Micro-bending causes attenuation due the presence of high frequency longitudinal perturbations in the fiber. The radius of curvature of microbends are less than a millimeter and usually originate from the transverse movement of a fiber during growth. Similar to variation in diameter, microbends couple power to higher order modes which have higher losses, leading to attenuation losses which increase with length of fiber.

The effect of waveguide imperfections on the transfer of power between different modes can be explained by invoking the mode theory of electromagnetic waves. For highly multi-mode fibers, like the SC fibers grown for the study, such an analysis becomes highly complicated. However, the loss of power via radiation can be understood using simple geometrical optics. Such an approach is well-described in Snyder and Love [54], and a brief summary of it follows.

Consider the propagation function of a bound ray in a waveguide, as shown in

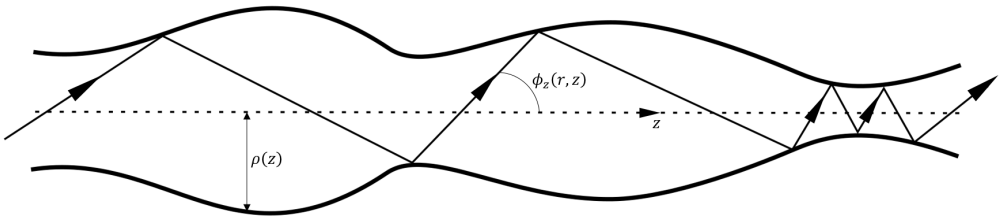

Figure 3.1: Exaggerated representation of fiber diameter fluctuations

Fig. 3.1. The propagation function depends on the local wavelength of the medium and the angle the ray makes with the optic axis of the waveguide.

$$\beta(z) = n(r,z)\phi_z(r,z) = n(r,z)\frac{dz}{ds} \tag{3.3}$$

Where n(r,z) defines the local refractive index of the waveguide medium and ϕ_z is the angle the ray makes with the optic axis of the waveguide. For a uniform and circular fiber, we can assume that the propagation constant remains invariant. Hence, at any particular length along the fiber,

$$\begin{aligned} n(z)\varrho(z)\sin\vartheta_z(z) &= n(0)\varrho(0)\sin\vartheta_z(0) \\ \sin\vartheta_z(z) &= \frac{\varrho(0)}{\varrho(z)}\sin\vartheta_z(0) \end{aligned} \tag{3.4}$$

For a ray to remain bound in a fiber waveguide, the angle of reflection at fiber surface should be less than the critical angle for the waveguide material with its surrounding medium. Hence,

$$\begin{aligned} 0 \le \sin\vartheta_z(z) &\le \sin\vartheta_c \\ 0 \le \sin\vartheta_z(0) &\le \frac{\varrho(z)}{\varrho(0)}\sin\vartheta_c \end{aligned} \tag{3.5}$$

Only rays satisfying the above condition at launch will be bound in the waveguide.

The total power associated with such bound rays varies as the square of the waveguide radius. With respect to the total power in bound rays, the power lost as radiation, under such conditions, assumes the following form

$$\frac{P_{rad}}{P_{bound}} = 1 - \frac{{\varrho_{min}}^2}{{\varrho_0}^2} \tag{3.6}$$

When the variation in diameter is small compared to the average diameter of the fiber, it can be assumed that

$$\frac{P_{rad}}{P_{bound}} = 2\left(1 - \frac{\varrho_{min}}{\varrho_0}\right) \tag{3.7}$$

Hence for a diameter variation of 2%, about 4% power can be lost due such irregularities. The diameter fluctuations regarded for this geometric optic approach only considers slow changes in the waveguide diameter and does not account for the much higher spatial frequency diameter variation due to formation of facets. Since their pitch is smaller compared to the wavelength of the light propagating, such features cannot be analyzed by regular ray optic approach.

Chapter 4

Rare-earth Ions

The first functioning laser was demonstrated by Theodor Maiman, in 1960, was a flash pumped ruby (Cr^{3+} doped sapphire) crystal. Since then, this approach of using a doped solid-state medium has become one of the most well-established methods of realizing a laser. And despite the development of lasers based on gases, semiconductors, dyes, etc., even now, some of the most advanced and versatile laser systems are solid-state lasers. Such devices can function over a wide range of wavelengths, continuous wave power or pulse peak power, pulse duration and energy.

All solid-state lasers are composed of a solid medium, amorphous or crystalline, doped with a laser-active ion. The optical transitions in these ions, when subjected to suitable external stimulus form the basis of the lasing action in such lasers. There are two main classes solid-state lasers based on the laser-active ion. Transition metal ions like Ti^{3+}, Cr^{3+}, Fe^{2+}, Co^{2+}, Ni^{2+}, V^{2+}, etc., which have incomplete *3d* shells have a number of low lying levels where optical transitions can take place. These ions are characterized by broad transition bands and generally involve simultaneous absorption or emissions of both photons and phonons. The *3d* wavefunction in such ions extends beyond the ion core and interacts strongly with the crystal field of the host, making such systems strongly dependent on the host material. For the

same transition metal ion, changing the host changes the site symmetry of the ion and, as a consequence, affects the emission and absorption bands features [55] [56]. Transition metal ion lasers are broadly tunable and have been developed to cover the entire wavelength range from 270 nm to 4500 nm. The second major class of solid-state lasers are based on RE ions. Rare earths or lanthanides are a set of fourteen elements starting from cerium (Z = 58) to lutetium (Z = 71). In their neutral state, RE atoms have the electronic configuration of xenon ($[Kr]4d^{10}5s^25p^6$) along with a partially filled *4f* shell and another electron occasionally in the *5d* shell. The incomplete *4f* shell gives these elements some peculiar magnetic and optical properties. In condensed phases, the most stable state of ionization of RE ions is the trivalent state and is the most common configuration found in optical devices. RE doped laser materials are generally composed of a high bandgap (>5 eV) inert host that is doped via substitution or addition with RE ions. Such materials have been extensively researched ever since the development of the first neodymium doped solid state lasers in the early 1960s [57] [58] [59].

4.1 Optical properties of RE ions

Most of the optical transitions documented in lanthanides result from *4f-4f* transitions, with the exception of Ce^{3+} and Pr^{3+} ions where the *5d* level lies low enough to allow *5d-4f* transitions via strong and broad absorption in the ultraviolet region [60]. Unlike transition metal ions, the interaction between the lasing ion and host lattice in RE based laser systems is quite weak. The *4f* wavefunction is well shielded from the crystal field of the host by the optically passive outer *5s* and *5p* electrons, making the *4f-4f* transitions in lanthanides very weakly dependent on the host material. The shielding of the *4f* ions result in weak host-induced splitting and mixing of energy states. It also implies that there is little or no phonon assisted transitions. All these

factors contribute to the optical transitions in lanthanides to manifest as sharp and narrow lines with high transition efficiency [61] [62].

Since the *4f* electrons are very effectively shielded from the lattice, the effect of external potentials can be treated as perturbations. In such a case, the Hamiltonian of a *4f* electron can be assumed to have the following form

$$H = H_{free-ion} + V_{static} + V_{dynamic} \tag{4.1}$$

Among the perturbation terms, while V_{static} is responsible for producing the electronic structure of the energy levels, $V_{dynamic}$ induces transitions between the electronic states.

The energy level structure of the RE ion can be obtained by treating the static interaction term using time independent perturbation theory. Commonly, each discrete energy level of a considered rare earth ion is assigned the identification $^{2S+1}L_J$, where S, L and J are the quantum numbers of spin, angular momentum and total angular momentum, respectively. The energy spectrum of the *4f* shell in the free RE ion can be satisfactorily described within the LS coupling approximation. In the absence of the perturbations, the *4f* electrons are assumed to move in a spherically symmetric potential of the nucleus and the other electrons. The solutions to such a potential are hydrogen-like wavefunctions. In hydrogenic systems, the total orbital angular momentum (L) and total spin angular momentum (S) are conserved and L and S are good quantum numbers. The solutions resulting from the central field are highly degenerate and fails to explain any of the structures seen in the electronic levels of the *4f* electrons. These structures are due to the lifting of the degeneracy when the additional perturbing potentials are taken into consideration. Among these perturbations, the strongest is the effect of the electrostatic interactions between electrons. Electrons in closed shells contribute a constant energy term to the

Hamiltonian. This term can be included in the central field potential for the free-ion and can be ignored while considering the perturbation due to Coulomb interaction between electrons. The electrostatic perturbation, hence, arises from the interaction between the *4f* electrons. This interaction lifts the angular degeneracy and yields states that are defined by L and S. The splitting due to such interaction is of the order of 10^4 cm^{-1}. Following the Coulomb interaction, the next strongest interaction is due to the spin-orbit coupling. The spin-orbit coupling removes the degeneracy in the LS terms, formed due to electrostatic interactions, and further splits them into J levels. The typical splitting between levels is of the order of 10^3 cm^{-1}. The final contribution to the perturbation comes from the host. The weak external electrostatic field due to the host lifts the degeneracy in the J levels and causes further splitting of energy levels. Such a process is an example of a Stark splitting, which describes the splitting of spectral lines in the presence of electric fields. While the maximum number of possible Stark levels depends on total angular momentum of the level, the precise width and number of stark levels depend on the symmetry and intensity of the external field due to the host. Typically, splitting between Stark levels is of the order of 10^2 cm^{-1}. The splitting of the energy levels in RE ions under the effect of different perturbing potentials is shown in Fig. 4.1

The dynamic interaction term in the Hamiltonian can be used to explain the transition between the electronic states described by the static interactions. The most significant contribution to the dynamic term comes from the interaction of the electron with the electromagnetic field, which gives rise to the emission and absorption of photons by the ion. As both emission and absorption involve the transition of the system from one quantum state to another, their occurrence can be explained by selection rules. Selection rules are in essence conservation laws applied to angular momentum and parity for the photon and atom system. The basis of the spectroscopic selection rules between two states is given by the transition moment integral.

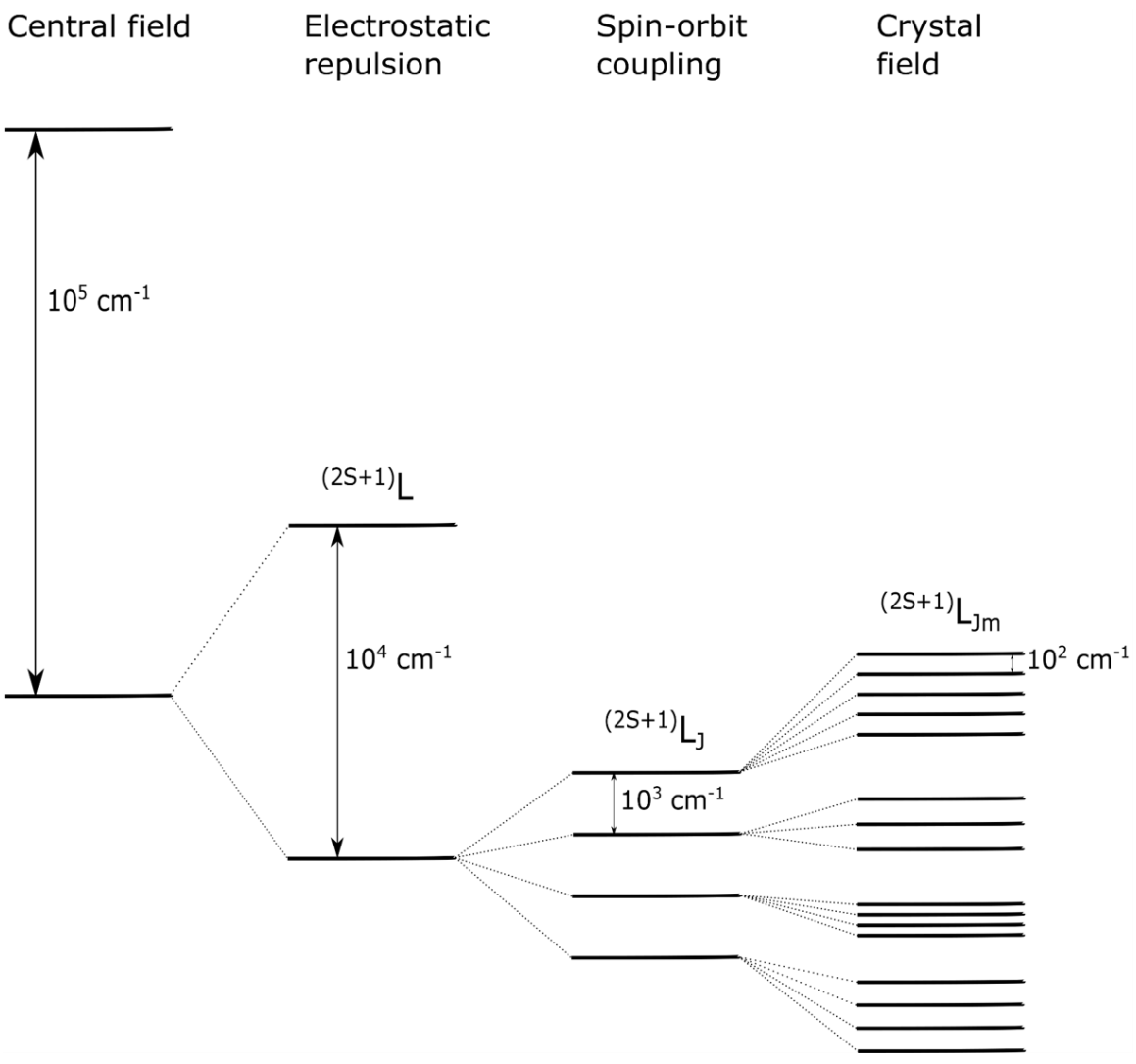

Figure 4.1: Splitting of energy levels in due to different interactions

Transitions for which the integral vanishes are called forbidden transition and have a low probability of occurring. In a medium, an electromagnetic wave can induce an electric or magnetic moment. The transition mechanics between two quantum states in a medium, in the presence of an electromagnetic wave, is dependent on these different electric or magnetic moments, from which the transition moment integral can be obtained. The difference between the electric and magnetic transitions arise from the angular momentum of the photon involved in the transition. The selection rules require that the change in angular momentum and parity between the initial and final states be compensated by the angular momentum and parity of the photon involved in the process.

For RE ions, the classical selection rules do not permit the transition between *4f* states via electric dipole processes as the initial and final states have the same parity. Although electric dipole transitions are forbidden, transition from one state to another are allowed to take place via weaker electric-quadrupole and magnetic dipole processes. However, the strengths of the *4f-4f* transitions were measured to be considerable higher than those allowed by electric-quadrupole and magnetic dipole transitions, even considering an intermediate coupling scheme. This anomaly in transition strengths is satisfactorily explained by the Judd-Ofelt theory that states that the *4f-4f* transition in RE ions happen by forced electric dipole mechanism [63] [64]. This theory, which is based on the concept of crystal fields assumes that in a solid host environment, non-centrosymmetric interactions such as ion lattice interactions allow the mixing of electronic states of opposite parity into the 4f wavefunctions, which somewhat relaxes the selection rules and the transition becomes partially allowed via induced electric dipole transition. The crystal field potential modifies the *4f* wavefunction to allow mixing of parities, resulting in a non-zero value of electric dipole transition. Such processes are usually weakly allowed transitions and are associated with small oscillator strength. Since these transitions are weakly allowed, they

are associated with high upper level lifetime, typically of the order microseconds to milliseconds, explaining the occurrence of metastable states in RE ions. The different energy levels of the $4f$ levels in trivalent RE ions is shown in Fig. 4.2

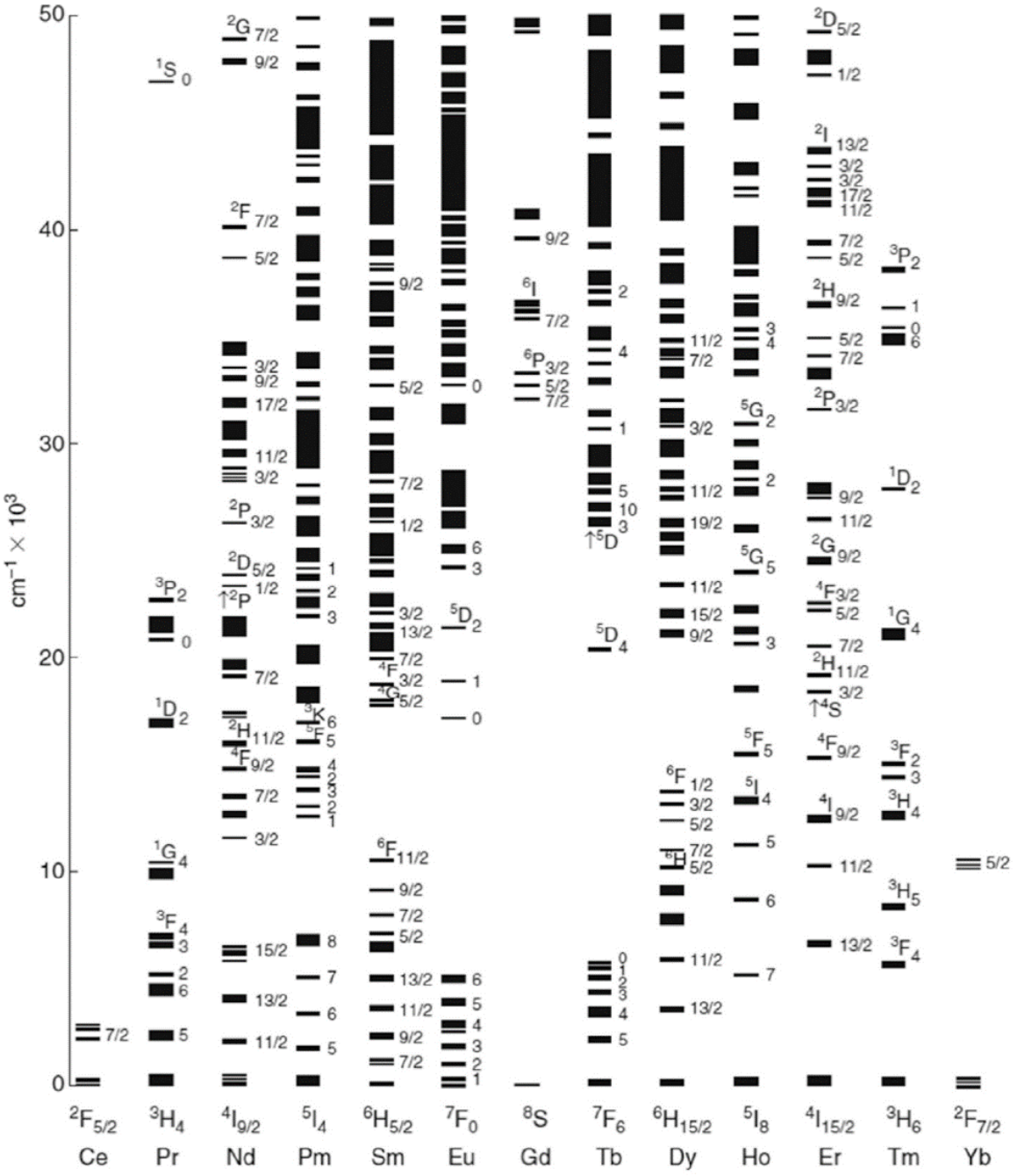

Figure 4.2: Energy levels of the $4f^n$ configurations of trivalent lanthanides (Ln^{3+}). Adapted from [65]. (Reprinted with permission)

4.2 Energy transfer mechanisms in RE doped materials

For RE ions in a solid host environment, energy transfer can occur between energy levels of the same ion or different ions. Depending on the pathway involved energy transfer mechanisms are of the following different categories:

- Radiative relaxation
- Non-radiative relaxation
- Co-operative mechanisms

If the difference between adjacent energy levels is large compared the phonon energy of the host, radiative transitions involving the emission of photons take place. Such transitions might occur via spontaneous emission in the absence of any external radiation or via stimulated emission in the presence of an external photon having similar energy compared to the separation between the two levels. The process of stimulated emission, which results in the production of photons exactly similar to the external photon, serves as the working principle for light amplifying devices like lasers and optical amplifiers.

If the energy levels are close enough, that is level separation is of the order of the phonon energy of the host, relaxation occurs via non-radiative relaxation. Such transitions which take place via simultaneous emission of phonons, are usually undesired while designing optical devices as they contribute to the loss energy as heat. Due to very high density of states of phonons, multiphonon processes are significant in solid state host but the probability of such processes decreases rapidly with increasing number of phonons involved. Non-radiative relaxations are most common in Stark components of a multiplet and transitions are very fast, in the order of 10^{-12} or 10^{-13} seconds.

Consider an energy level diagram shown in Fig. 4.3. After an ion is excited to

upper level 5 by absorption of suitable radiation, it relaxes through sequential non-radiative transitions to level 3. Since the energy difference between levels 2 and 3 is large compared to the phonon energy of the host, the ion undergoes a slow radiative relaxation to level 2 from which it decays to the ground state through another non-radiative relaxation.

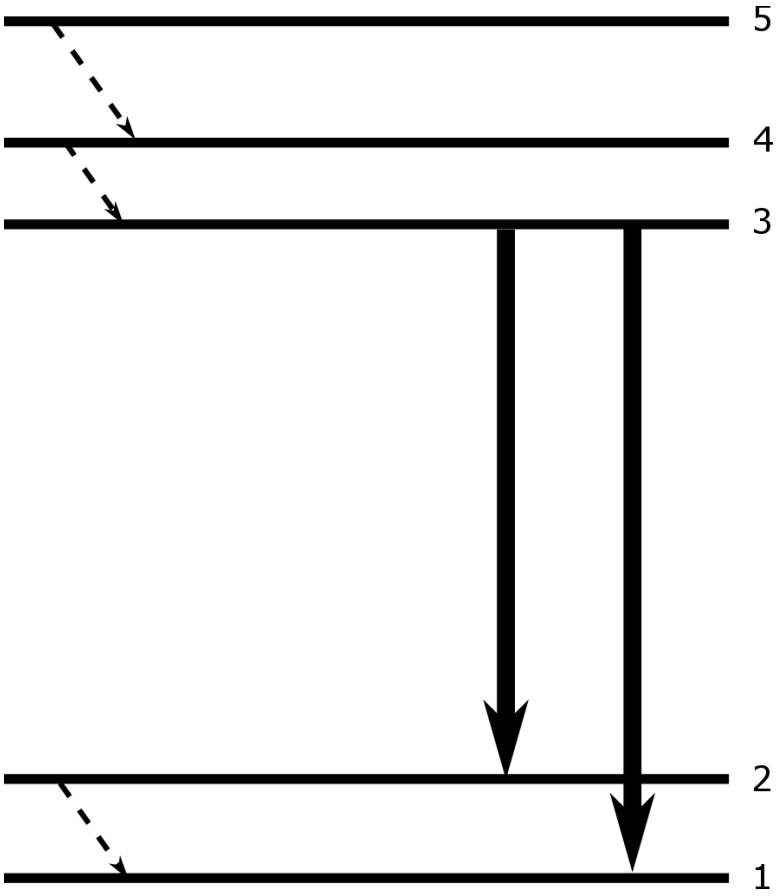

Figure 4.3: Simplified energy level diagram showing radiative (solid line) and non-radiative (dashed line) relaxation in a typical rare-earth ion

The two energy transfer mechanisms discussed above have assumed that the laser ions are isolated in a solid-state host. However, as the concentration of the dopant increases, the ions cannot be treated as isolated systems and multi-ion interactions need to be considered. Under suitable circumstances, RE ions may share or transfer energy between ions of same or different species. Ions closely located with other ions may transfer energy without the emission or absorption of a real photon. Such energy

transfer schemes are phonon-assisted and show significant dependence on temperature. When the transition takes place between ions of different species, these energy transfers usually necessitate the emission or absorption of phonons to compensate the difference in transition energies of the different ions. The transfer of energy from one ion species to another is most commonly used to sensitive laser materials to facilitate pumping in ions which do not have strong absorption bands at common pumping wavelengths. Using a large concentration of one species, the optical energy from the pump is absorbed and transferred to the emitting species. One common example of such a co-doped system is Yb^{3+} sensitized Er^{3+} solid state system, which allows the use of high power Nd based lasers at 1064 nm as pump sources [66].

While co-doping might seem like an appealing approach to expanding the pumping options for different solid-state lasers, in practice co-doped systems are not that common due to the difficulty in managing unwanted inter-ion energy transfer processes [67]. These processes are:

- Cross-relaxation
- Up-conversion

Cross-relaxation involves the partial transfer of energy from an ion in an excited state to another ion in the ground, resulting in both ions in being in lower excited states. In most cases, these lower excited states decay non-radiatively to the ground state, resulting in the generation of heat. This is the primary quenching mechanism for Nd^{3+} ions, where an ion in the excited metastable $^4F_{3/2}$ level interacts with a neighboring ion in the ground state and both ions end up on the intermediate $^4I_{15/2}$ level from where both ions decay non-radiatively to the ground state [68].

Up-conversion involves the complete transfer of energy from an ion in an excited state to another ion in the same excited state. This results in one ion returning to the ground state while the other ion is moved to a higher excited level. Eventually, the ion in the higher excited state relaxes non-radiatively and returns to its original

excited state. The net outcome of the process is half of the absorbed energy is lost as heat. This is a major factor causing low efficiency of Er^{3+} ion systems. In this case, one excited ion at the metastable $^4I_{13/2}$ transfer all its energy to another ion at the same level, resulting in one ion in the ground state and the other upconverted to the $^4I_{9/2}$ level from where it relaxes non-radiatively back to the metastable level [69].

Part III

Experimental Methods

Chapter 5

Laser Heated Pedestal Growth Technique

Since their invention, lasers have played an ever-increasing role in various material processing techniques. Characteristics like single frequency, coherence and collimation make lasers extraordinary processing tools, providing a clean and highly controllable energy source. Using suitable optical components, the generation of localized regions high energy density can be achieved. From the perspective of crystal growth, melts can be generated without the need of a melt container, leading to crucible-less crystal growth.

Of the different laser-based crystal growing techniques, the LHPG technique is the most widely used in the research community [70] [71] [72] [73]. It is essentially a modified float-zone technique where a suitable laser is used as the energy source to create a miniature molten zone on top of a source pedestal, from which a crystal fiber is pulled. There are several advantages this technique offers over other crystal growing techniques. As the laser radiation can be focused to a very small region, it produces a very steep thermal gradient at the growth interface, allowing for a fast pulling rate. The rate at which a crystal can be grown is about 60 times faster compared

to Czochralski method for bulk crystal growth. Since the molten zone is created by focusing a laser beam, extremely high temperatures can be achieved without the need for searching for suitable crucible materials. This enables the growth of materials with very high melting points. The absence of a crucible also means that the single crystals grown by this technique are extremely pure with very low concentration of impurities. Since the crystal growth front is free, and not in contact with an external surface as in the case Bridgman growth, the crystal has low inherent stress. Furthermore, as the laser beam can be focused to a very tight spot, SC fibers of very small diameters can be pulled using this technique.

While the LHPG technique is schematically similar to drawing of glass fibers, there are a few major differences. These differences arise from the material differences between crystals and glasses. While both crystal pulling by the LHPG technique and glass fiber drawing start with a source pedestal or preform, the reduction of diameter of the fiber to the source is vastly different. In the glass fiber drawing process, the glass preform is softened to a "neck-down" region from where the fiber is drawn out. The high viscosity of glassy materials under such circumstances provide an auto-dampening of perturbations and permit a considerably long molten region, ultimately allowing a very high reduction in diameter in a single cycle of fiber drawing. The high viscosity is also responsible for the very fast draw speed of glass fiber drawing. Draw speeds of several meters per minutes are typical of glass fibers in the industry. However, unlike glassy materials, the growth of crystal fibers involves a true liquid phase melt. In the absence of a crucible, the low viscosity molten zone in the LHPG technique is only held together by surface tension. This makes the growth highly susceptible to external perturbations and fluctuations in the melt. The low viscosity of the melt also restricts the diameter reduction and draw speeds in crystal fiber pulling. Although when compared to other crystal growing techniques, the growth rate in LHPG technique is much higher due to the high thermal gradient, it is much

slower than glass fiber drawing, about 3-4 orders of magnitude slower.

LHPG systems, in the early stages of developement of the technique, used multiple focused laser beams to create the melt. Symmetric arrangement of two to four laser beams have been utilized in the early stages of the LHPG technique development [20]. The current form of the LHPG apparatus, which uses a single laser beam and ring-forming optics called axicons, was developed at Stanford University in the early 1980s [22]. Their apparatus used a specially designed optical component called a reflaxicon which converted the circular spot of a laser beam into a ring. This ring of laser radiation was then focused on top of a source pedestal using a focusing mirror, creating a miniature melt at the tip of the pedestal. Over the years, there have been several modifications to the original design with the incorporation of different elements like after-heaters, electric dipoles, etc. However, despite these alterations, most currently functioning LHPG systems are, in essence, based on the basic design developed at Stanford.

Apart from the energy source, the other major part of the LHPG apparatus is the fiber pulling mechanism. The position of the melt is kept constant while the seed and the source feedstock are moved out and into it respectively. Two sets of independent pulling mechanisms are required for the translation of the source pedestal and the growing SC fiber respectively. It is worth noting here that, unlike Czochralski crystal growth, most LHPG systems do not involve a mechanism to rotate the seed crystal during crystal growth. Due to the small size of the molten region, such a mechanism would require a very high degree of sophistication so as to not introduce any disturbance in the melt. To maintain the uniformity of the crystal growth, rather than rotating the seed, the azimuthal heat distribution in the melt is made very uniform by fine-tuning the optical components present in the path of the laser beam.

As the fiber is pulled continuously from the melt, the source pedestal must be fed simultaneously and continuously in the region of the focus of the laser beam to

maintain a zero-net mass flux in the melt. Hence the conservation of mass relates the translational velocities of the source and fiber with their diameters.

$$d_s/d_f = \sqrt{v_f/v_s} \tag{5.1}$$

where d_s and d_f denote the diameters of the source and fiber respectively while v_s and v_f demote the velocity of the source and fiber respectively.

At steady state, the diameter of the source pedestal is uniform and it is theoretically possible to grow fibers of uniform diameter by maintaining a constant ratio of translational speeds of the source and the fiber. However, in practice this never occurs and some form of automatic diameter control is required to grow fibers of a certain preset diameter. Fluctuations that result in deviation from steady state behavior may arise from different factors like variation of the source diameter, fluctuation of the melt due to laser power and mechanical perturbation, etc. To mitigate the effect of these factors on the diameter of the SC fiber, a closed-loop growth system is necessary. Such a system is usually implemented by a proportional-integral-derivative (PID) control loop where the diameter is monitored in real time and the deviations from the set value are used to control the speed of the either the source or the seed or both. The effect of a closed-loop growth process is illustrated in Fig. 5.1, which shows the comparison of diameter variation between two growths, one with and the other without diameter control.

Monitoring of the fiber diameter can be achieved by several approaches, each of which has its own advantages and disadvantages. The diameter of a fiber can be determined by measuring the interference fringes when they are side-illuminated by a laser [74]. Assuming a circular cross-section fiber, a laser will produce quasi-sinusoidal fringes when it passes along the cross-section of a fiber. The width of the fringes and the distance of the laser source and detector can be used to calculate

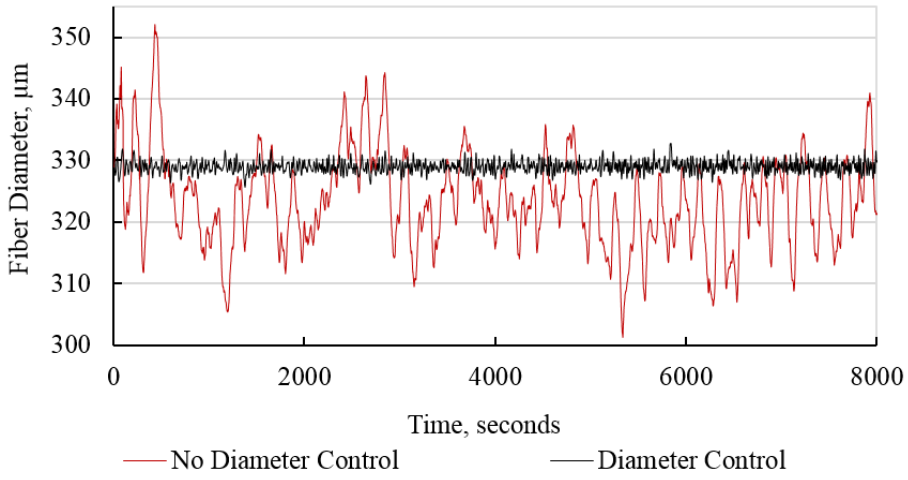

Figure 5.1: Fiber diameter measured during growth for two fibers, one with a diameter control feedback loop and a second fiber grown without diameter control.

the fiber diameter. While this method has a very good resolution and fast response, it is strongly dependent on the fiber geometry of the fiber cross-section, making it very error-prone if the fiber growth is not straight. Another method of the measuring the diameter is by the use of a non-contact laser micrometer. A laser micrometer usually comprises of two parts, an emitter and a receiver. The emitter uses a laser beam to scan across a given range at a known speed. Any object in the path of the scanning beam will cast a shadow and will interrupt the transmission to the receiver unit. The diameter of the object can be calculated by measuring the shadow period on the receiver. Although sub-micron resolution is possible, the response of this method is slower compared to the measurement of fringes as it is limited by the scan rate of the emitter unit. The final method of measuring the diameter involves the counting of pixels on the image of the fiber as captured on a CCD camera [75]. The glowing molten zone, due to the intense blackbody radiation, can be easily identified on a camera image and a software can be used to read off pixels at its upper edge where the growth interface is located. Both the resolution and response time of this technique are strongly dependent on the specifications of the CCD sensor and hence

can vary significantly based on the particular hardware used. This approach is very versatile and flexible; however, it requires a good knowledge of programming to design a suitable software that serves the needs for such applications.

5.1 General considerations regarding LHPG

The source rod or pedestal used in the LHPG process can be either single crystalline or ceramic material. Single crystalline source rods are obtained from previously grown crystal boules. Ceramic bars are fabricated by densifying and sintering ceramic powders. Source rods may also be obtained by cold extrusion process, where an organic binder is used to mold powder into small bars that can be used in the LHPG apparatus. While using single crystalline sources almost guarantees a high quality starting material with low impurity concentrations, it is usually more expensive than the other sources described. It also does not offer much flexibility with the stoichiometry of the material. Cold extrusion process allows for the preparation of source material with precise control over material composition but the presence of binders like PVA make them problematic during crystal growth using the LHPG technique.

Since the starting material for the crystal growth is a solid pedestal, the LHPG techniques allows for the possibility of growth of continuous SC fibers with compositional variation. Fibers with both varying doping levels and varying host matrix have been grown [76]. Using a pedestal with longitudinally fused sections of different materials, fibers with continuously varying composition have been demonstrated. A convenient approach to grow fiber monoliths of varying dopant concentration is by using a source pedestal coated with varying thickness of a particular (or different) dopants. Such a process will not only allow for the growth of fibers with varying dopant concentration, but provides the opportunity to introduce multiple dopants in the same fiber crystal. This has been demonstrated effectively in oxide crystal

fibers where layers of dopant oxide are deposited on the pedestal by vapor deposition techniques, sputtering [29], or sol-gel methods [77].

The seed crystals used in the LHPG technique are usually previously grown SC fibers. The seed determines the crystallographic orientation and the shape of the crystal fiber cross-section of the pulled crystal. For sapphire crystal fibers, circular cross-section fibers are obtained when {0001} oriented seeds are used, whereas fibers grown along the <1010>direction yield non-circular fibers with two parallel sides representing the {0001} basal facets [78]. Several studies have been focused on facet suppression in crystal fibers using oriented seeds. Ishibashi *et al.* used a seed oriented 15° from <100>to <110>to grow facet-free Ca,Cr:YAG SC fibers [29]. Apart from crystalline seeds, metallic wire seeds (Pt, Au, etc) have also been used [79]. Due to the high thermal conductivity of metallic wires, the melt temperature drops abruptly as soon as the seed is dipped into the melt and hence the laser power needs to be properly adjusted to initiate and continue crystal growth. Seeding with metallic wires usually leads to crystal nucleation in a direction perpendicular to wire surface.

The interaction of the solid and liquid phases during a crystal growth process is affected by the growth atmosphere. Several studies have explored this idea in the LHPG technique. SC fibers have been grown under air, He, Ar, N_2, H_2, Cl_2, etc. Growth has also been examined under various pressures. Studies have focused on the role of atmosphere and pressure on the rate crystal pulling and defect density in the single crystals. For sapphire fibers it was reported that the most ideal growth atmosphere is 5 Torr of He [73]. Similar results have been reported for a variety of other LHPG grown SC fibers.

For all techniques involving crystal growth from a melt, the shape of the solid-liquid interface is very important. Since LHPG is a float zone technique, the entire shape of the molten zone to be very critical for the crystal growth. In the LHPG technique, the molten zone is held together by surface tension. At steady state growth

condition, an equilibrium shape is attained and the surface energy of the molten zone is at a minimum. Minimization of the surface energy also means that the surface tension at the solid-liquid-gas tri-junction is balanced and an equilibrium wetting angle is reached. At a steady state the meniscus angle for a particular material growing in a particular atmosphere is constant. If a net-zero mass flux of the melt is maintained and growth continues in such a state, there is no variation in diameter. However, in a real crystal growth, such a condition is almost never achieved due to fluctuations in the melt and the equilibrium meniscus angle is not maintained, leading to diameter variations. Numerical modeling based on the shape and thermodynamics of the molten zone have shown that the fiber growth is possible for a range of aspect ratios of the molten zone, with the most stable growth achieved when the diameter of the grown fiber is a third of the source pedestal.

The thermal gradient at the solid-liquid interface produced in the LHPG technique is very high, of the order of $10^3 - 10^4$ °C/cm. The steep thermal gradient facilitates in the fast crystal drawing speeds associated with this technique. Another consequence of the high thermal gradient is the resistance to constitutional super-cooling. A smaller fiber diameter allows for a faster pulling rate before constitutional cooling takes place. However, the steep thermal gradient also introduces a high level of stress in the fibers. Not only do stresses increase possibility of various crystallographic defects, localized regions of stress affect the transmission characteristics of fibers.

For all floating zone based crystal growth technique, zone-refining is an inevitable consequence. For a two-component system, the solubility of one component in the other is usually different for the solid and liquid phases of the solvent. Depending on the solubility, an impurity (solute) can be preferentially incorporated into or rejected from the solid phase of the solvent. The quantity that determines this preferential behavior is known as the segregation coefficient (k_0). For a solute-solvent pair, if the k_0 for the solute is less than unity, the solute will be rejected from the solid phase

into the liquid phase, increasing the concentration of the solute in the liquid phase compared to the solid. The opposite phenomenon happens if k_0 is greater than unity. In zone-refining technique, a heating element progresses a molten region along the entire length of the crystal, melting only a small section of it at any given instant. As the melt moves forward, the molten region freezes back to a solid phase. This entire cycle of the crystal going from solid to liquid and then back to solid, changes the concentration of impurities in the crystal after the melt region passes through it. Consider a solute with k_0 less than unity. As the heater moves through a section of the system, the solute in the melt is rejected from the solid due to decreased solubility in the solid phase. This decreases the concentration of the impurity in the newly re-solidified region of the crystal. Considering this mechanism, LHPG technique can be regarded as a single pass zone-refining technique where instead of a moving molten zone, the crystal itself is moved through the region of the melt. The concentration of impurities, whose segregation coefficient is less than unity, regardless if it is introduced deliberately or not will be reduced when grown by LHPG technique. There will always be a decrease in concentration in the grown fibers compared to the source material, with a gradual increase in concentration down the length of the fiber. Such a phenomenon has been noticed in the growth of YAG doped with impurities like cerium and neodymium.

5.2 LHPG Set-up at Rutgers University

The original LHPG apparatus at the Rutgers University was donated by the Bellcore Corporation. It was one of the first LHPG systems ever assembled and was principally based on the design developed at Stanford University. Since then, numerous modifications have been made to the system to replace all the original components and update to the most recent standard. The main components of the system are

the laser, the focusing optical system, the crystal pulling mechanism and the growth monitoring imaging system. Most of these modules are inter-connected and controlled via a hardware interfacing software developed in the National Instruments Labview environment. The schematic of the set-up is given in Fig 5.2.

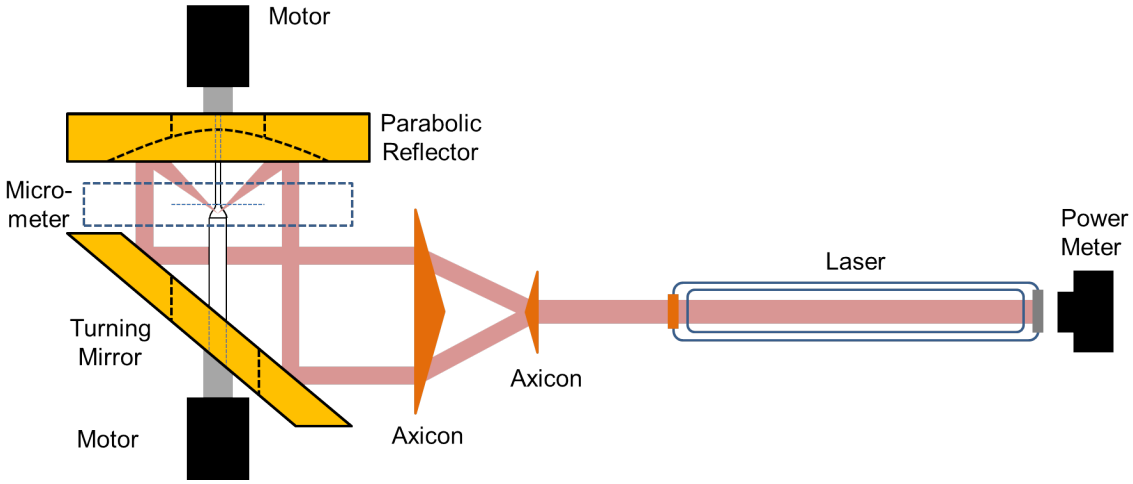

Figure 5.2: Schematic of the laser heated pedestal growth apparatus

Since most of the crystal grown using the LHPG system at Rutgers were oxides, a CO_2 laser was used as the melt-forming energy source. Most oxides strongly absorb in the long-wave infrared region, making the 10.6 μm radiation from CO_2 lasers very effective in processing them. The source laser used in the LHPG apparatus at Rutgers was a cw sealed gas CO_2 laser manufactured by Laser Engineering Inc., Milford MA. The beam size was measured to be 7 mm e^{-2} in diameter, with reasonably good output mode quality and stability (see Fig. 5.3). The maximum output of the laser was 36W. However, the growth process, the laser was operated in the range between 12W to 20W. Lower power was required to grow fibers of smaller diameters. For such growths, a wire-grid attenuator (Lasnix, Model 102) was used to lower the power available for the growth. The laser cavity had no polarization selecting optic and as a result, the output beam was unpolarized. The laser was water-cooled by temperature-controlled water circulated with the aid of a chiller (Neslab, RTE – 113). The laser had a warm-up period of 60 minutes after which it demonstrated an output fluctuation of less than

±0.5%. It was observed that for optimum stability of CO_2 laser output, the ideal room temperature needed to be maintained between 23°C and 24°C. Operation at such temperatures reduced the occurrences of a laser line hop. It had been previously reported by Fejer that the major factor contributing to growth fluctuations was lack of stability of the laser source. Hence, considerable effort was made to stabilize the laser power [80]. The laser power was stabilized electronically by via a PID control feedback loop. To avoid introducing additional optics in the beam path of the CO_2 laser, a beam-splitter was not used to monitor the laser power. Instead, the laser power was monitored by measuring a small fraction of the laser output through a 99.7% back-reflector in the CO_2 laser cavity. This value was fed back into the PID control loop which controlled the laser output by varying its operating voltage of the laser. Using such an approach, power stability with fluctuations of less than ±0.5% over 15 hours of continuous operation was demonstrated.

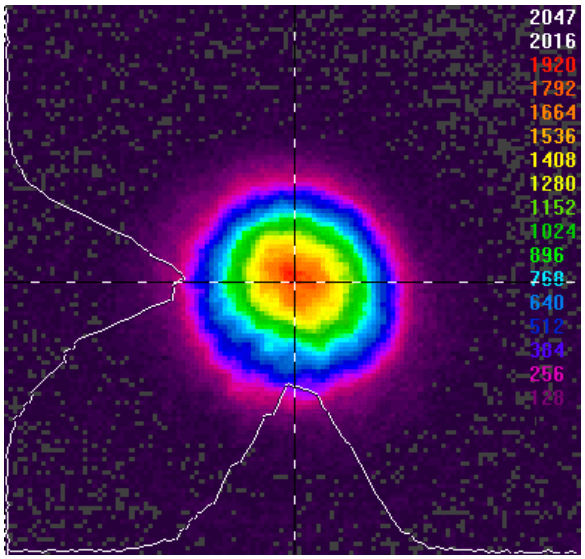

Figure 5.3: Mode profile of CO_2 laser

The Gaussian beam from the laser source was transformed into a collimated ring using an axicon. This ring was then focused on top of the source pedestal using a parabolic mirror. In the original Stanford LHPG apparatus, the axicon optic was a reflaxicon. The reflaxicon consisted of a pair coaxial pieces of diamond turned copper

conical pieces. The axes of the conical pieces were made to coincide with the axis of the laser beam. The first cone, with its apex towards the laser, produced a diverging ring. The second conical piece, which has the same apex angle as the first piece, reflected this diverging ring, producing a collimated ring. Such an arrangement of the optics can be referred to as a convex reflaxicon. The reflaxicon used by Nubling on the LHPG apparatus at Rutgers consisted of a pair of coaxial ZnSe optics [24]. Using ZnSe optics eliminated the need to support the first conical optic using a system of spokes and struts which lead to some part of the ring being obscured. In this modified reflaxicon system, the first optic had a Ag-coated diamond turned conical depression at the center. The diverging ring produced by this optic was collimated by a second coaxial Ag-coated conical ZnSe optic with the same apex angle. This arrangement of the optics can be called a concave reflaxicon. Although the Ag-coated ZnSe reflaxicon produced a very azimuthally symmetric annulus of heat, the quality of the silver coatings degraded over time and had to be re-coated to maintain uniform reflections from the surfaces. To overcome the need to recoat the optics, in the most recent iteration of the LHPG apparatus, the use of a transmissive axicon system was introduced [81]. This arrangement also simplified the optical system as each component interacted with the laser beam only once.

Transmissive axicons or simply axicons are conical prisms which produce diverging rings of constant thickness from a light source. The ring produced by such an optic has properties very similar to Bessel beams and are non-diffracting and have non-evolving transverse intensity distribution. The axicon system in the LHPG apparatus used in this work comprised of two ZnSe axicons with matching α of 10° (made by ULO Optics, Stevenage, UK). The optics were AR-coated for 10.6 μm. The laser beam was incident on the first optic, which was 28 mm in diameter, producing a diverging ring. The ring was then collimated by the second optic, which was 75 mm in diameter. In the system, the axicons were placed coaxially, 120 mm apart. The common axis was

made to coincide with the CO_2 laser beam. The size of the diverging ring produced by an axicon is given by the formula

$$d_r = 2Ltan[(n-1)\alpha] \tag{5.2}$$

where L is the distance between the two axicons, n is the refractive index of the material of the axicon and α is the alpha angle for the axicon pair. Using this formula, the size of the collimated ring was deduced to be about 60 mm. This was independently verified by recording a burn pattern of the ring on a carbon paper.

Following the axicon pair, the ring was reflected up with a coated copper flat turning mirror. The final optical component in the focusing system is a parabolic mirror. The parabolic mirror focused the collimated ring into a tight spot on the source pedestal to form the miniature floating melt zone. A parabolic mirror was selected to avoid the spherical aberration issues that arise with using spherical mirrors for such extended aperture sizes. A gold-coated parabolic mirror, (made by Thorlabs, NJ) with a 25.4 mm focus was used as the focusing optic in the described set-up.

To initiate growth, both the seed and the source pedestal needed to be aligned properly where the laser was being focused. To provide this freedom, they were mounted on individual x-y translation stages. A belt-translation based system was used for feeding the source and pulling the fiber. The belts were driven by brushless servo motors (National Instruments AKM). To improve resolution and smoothness of motion, worm gears were used in conjunction with the motors. The requirement for the smoothness of motion of the belts during growth cannot be overstated. Discontinuous and jerky movement of the belt leads to the growth of fibers of poor quality with significant fluctuations in diameter. These fibers, such as the one shown in Fig. 5.4, are characterized by very high losses. The fiber was moved along a grooved metallic block (or v-groove block) by the friction of the belt. Metallic blocks of different

groove depths were used for guiding fibers of different diameter ranges. For fibers with diameter less 500 μm, an additional guide-tube was used to prevent the fiber from "wandering" off axis, in the plane perpendicular to the fiber growth direction. This guide-tube would be placed between the molten zone and the v-groove block. The guide-tube was chosen such that it was no more than 20 μm larger than the fiber to prevent significant lateral movement.

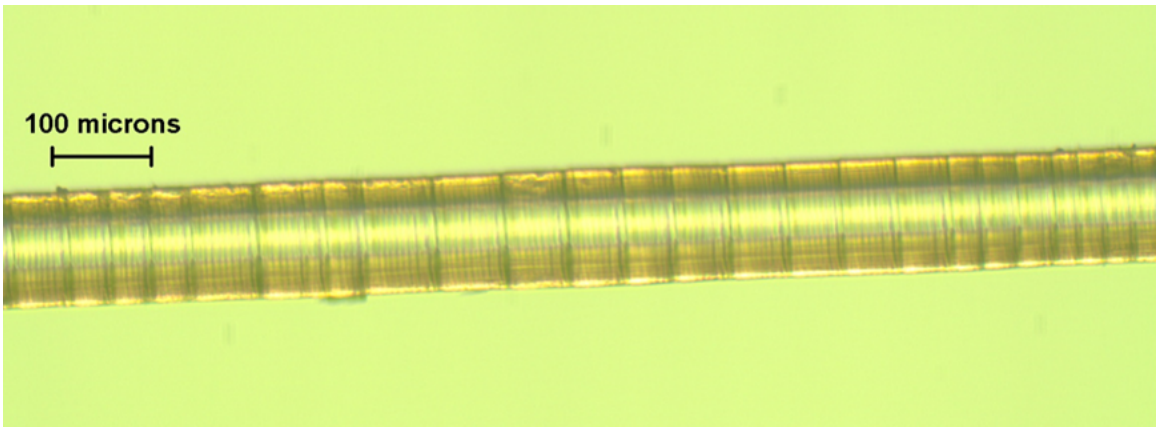

Figure 5.4: High-loss YAG SC fiber grown with discontinuous motor movement. Such a fiber had a loss of 1 dB/cm.

The pulling rate of the fiber and the feeding rate of the source were controlled via closed loop PID control. The diameter of the fiber was continuously monitored using a laser micrometer (Model 162-100, Laser Gauge). The PID control was executed via the same Labview program used to control the laser power. Without the active closed loop growth, the grown fibers show a slow sinusoidal variation in diameter, with variation of ± 15 μm for 340 μm diameter. However, when the feedback loop was engaged, the diameter fluctuations for a similar growth were reduced to less than ± 1 μm. Since the functioning of the PID loop for the automatic diameter control was based on the value of the diameter read by the laser micrometer, care was taken on the exact position the micrometer was monitoring. For proper operation of the feedback loop, the micrometer needed to be set at the upper solid-liquid junction, *i.e.* at the fiber growing interface. If the micrometer was set higher than the interface, the

laser micrometer would be sending delayed data to the loop and hence the diameter control would also act in a delayed manner. On the other hand, if the micrometer was set lower than the interface, the reading would not be the true diameter of the fiber, rather it would be higher due to the shape of the molten zone. Under such circumstances, the calculated speed of translation of the source and/or the fiber needed to be readjusted to reflect the true diameter reading of the fiber.

The imaging system, which was very critical in the alignment process, comprised of two digital cameras along mutually perpendicular directions. The cameras provided simultaneous highly magnified view of the molten zone along two axes. During the alignment process, a third camera was temporarily used to provide a view from the top, looking down along the direction of fiber growth.

5.3 Alignment of optical system

The quality of the SC fibers grown using the LHPG method depends largely on the symmetrical shape and homogeneity of the melt zone. Asymmetric heating in the melt leads to highly strained fibers of poor quality fibers which are characterized by high transmission losses. Moreover, a non-uniform distribution of heat in the melt leads to curved fibers which, very often, jam inside the fiber pulling mechanism and stop growing altogether. Hence, proper alignment of optical components is central to the growth process. However, conventional aligning techniques for visible and near-IR lasers are not applicable in this situation, as the 10.6 μm CO_2 laser is in the mid-IR wavelength region. This means that typical IR visualization and alignment cards do not work. Moreover, effects of different misalignment are difficult to distinguish using carbon paper or imaging plates. Hence the effect of misalignments of each of the optical components, which cause asymmetric heating of the melt, were simulated using Zemax, a commercially available optical ray-tracing software. By isolating the

misalignments causing the non-uniformity in the melt zone, it was possible to fine-tune the optical alignment of the components [82].

As shown in Fig 5.5, two axicons, a turning mirror, and an on-axis parabola define the optical system in its simplest form. The exact specification and spacing of each optical component is described previously. The order in which objects interact with rays depends on the object geometry, angle, and position of the input ray, rather than the order of the objects in the system specification. This analysis technique allows for future analysis of stray light and other effects on the system, as well as greater flexibility in adding objects and detectors for better visualization and study.

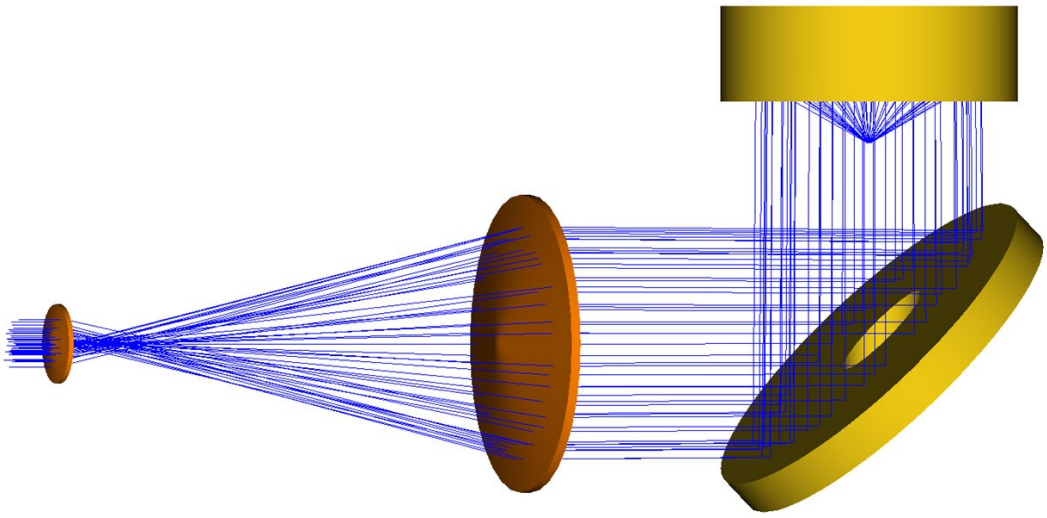

Figure 5.5: The primary optical components in the LHPG apparatus. These four components transform the Gaussian beam from the CO_2 laser to form a ring and then focus it on top of a source bar.

The simulations look primarily at the alignment of the two axicons, as well as some aspects of the parabola. The results of the simulations are shown in Figs. 5.6 through 5.11. An input Gaussian beam is used for all of the simulations. For Figs. 5.6, 5.7, 5.9, 5.10, and 5.11, the first column shows the intensity pattern on a plane placed 35 mm after the second axicon. The second column shows the intensity pattern when

the observation plane slightly above the focus. The first axicon in the two-axicon ring shaping system primarily affects the intensity distribution of the light in the ring. This can be seen in the first column of Fig. 5.6. The intensity patterns in the first column, which is 35 mm after the second axicon, will always look close in shape to a ring. However, the farther that the observation plane is set, the more the error in the axicon alignment can be seen. The second column contains the observation plane roughly 1 mm before the focus. The shape and intensity of the ring output looks appreciably altered by shifts in the first axicon. This is expected, as the axicon being shifted indicates that the Gaussian beam is off-center from the axicon tip. The axicon's circular symmetric conical shape is what causes the diverging ring shape, and therefore the case of a non-concentric beam and axicon leads to a non-uniform ring distribution at the output.

The effect of shifting the second axicon is shown in Fig. 5.7. In the figure, it seems as though the profile of the beam following the axicon system is unchanged. This is true if the observation is located near the second axicon. However, as the observation plane moves farther away, the beam shows more of the distortion caused by lateral misalignment. Although Fig. 5.6 and Fig. 5.7 look similar, the sequences of images are different in two important ways. Firstly, the left column in Fig. 5.6, which is a cross-section of the beam 35 mm after the second axicon, changes significantly with a shift in the first axicon. This differs from the left column of profiles shown in Fig. 5.7. In this case, the profile following the first axicon is fixed to be that of a properly aligned first axicon. Secondly, the right columns of Fig. 5.6 and Fig. 5.7, being very similar to one another, illustrate an important concept in the alignment process: it does not suffice to look at only one plane when aligning the system. The focal plane cannot distinguish between a shift in the first axicon, and other observation planes are necessary to determine the cause of the distortion. Once aligned, the first axicon evenly distributes the laser radiation in the characteristic ring shape, and can

therefore remain fixed to simplify alignment. This is very important in saving time when aligning, and considering the error in alignment of the practical system.

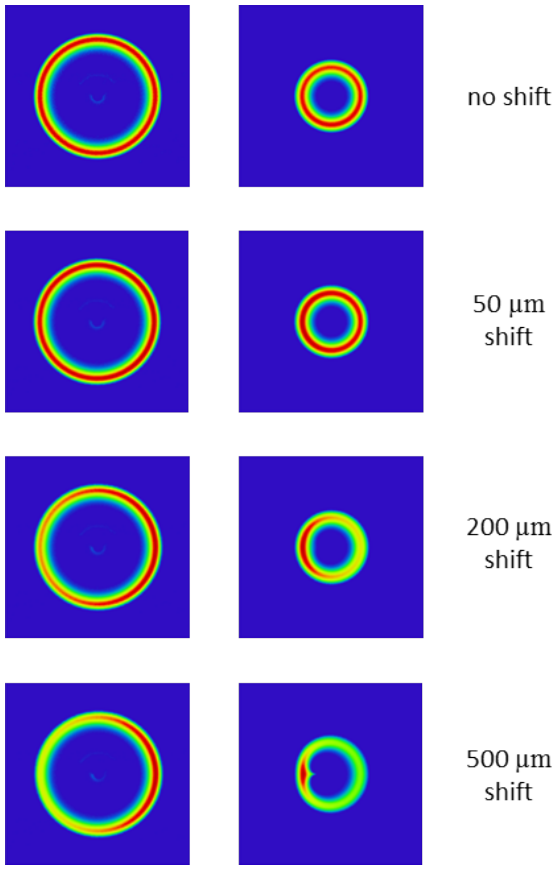

Figure 5.6: Effect of lateral displacement of first axicon.

We see that it is relatively simple to get a cardioid at the focus, by simply shifting the second axicon half a millimeter in the simulated setup. When the second axicon has a considerable misalignment, the cardioid can be seen very easily. Such an exaggerated situation is shown in Fig. 5.8, where the second axicon is laterally misaligned by 2.09 mm.

In addition to lateral displacements and misalignments, the axicons can also be tilted with respect to one another. The effect of tilting the first axicon has a similar effect as tilting the second axicon. However, something to note is that tilts of the first axicons have a significantly smaller effect on the output characteristic of the focus, as compared to tilts of the second axicon. The ring near the output of the two-

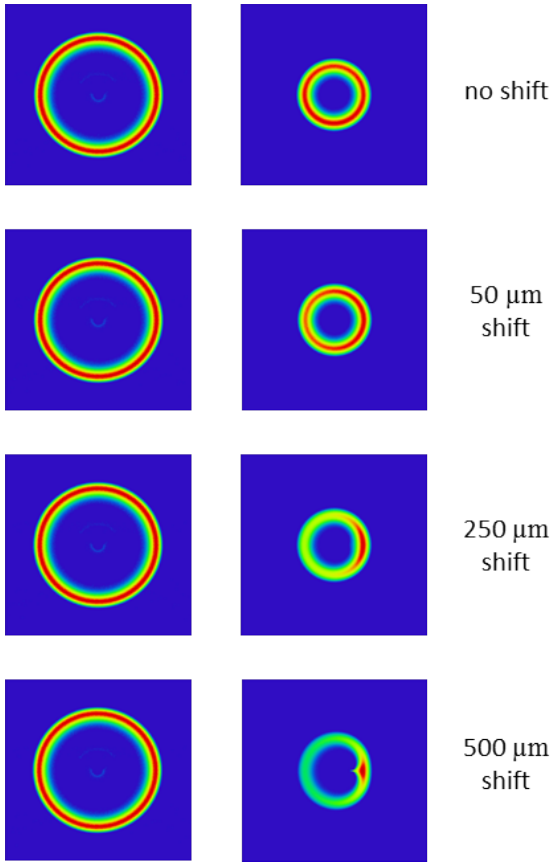

Figure 5.7: Effect of lateral displacement of second axicon.

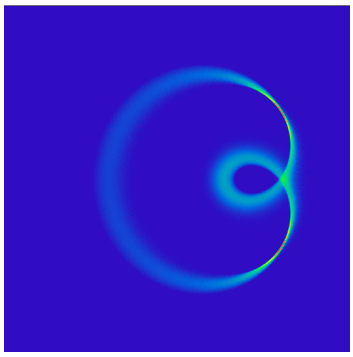

Figure 5.8: Effect of excessive lateral misalignment of the second axicon.

axicon ring shaping system is almost identical in these cases. But again, a noticeable difference is observed if the imaging plane is farther away. As evident in Figs. 5.9 and 5.10, the effect of tilting the second axicon, has a stronger effect on the focal shape and intensity than the first axicon.

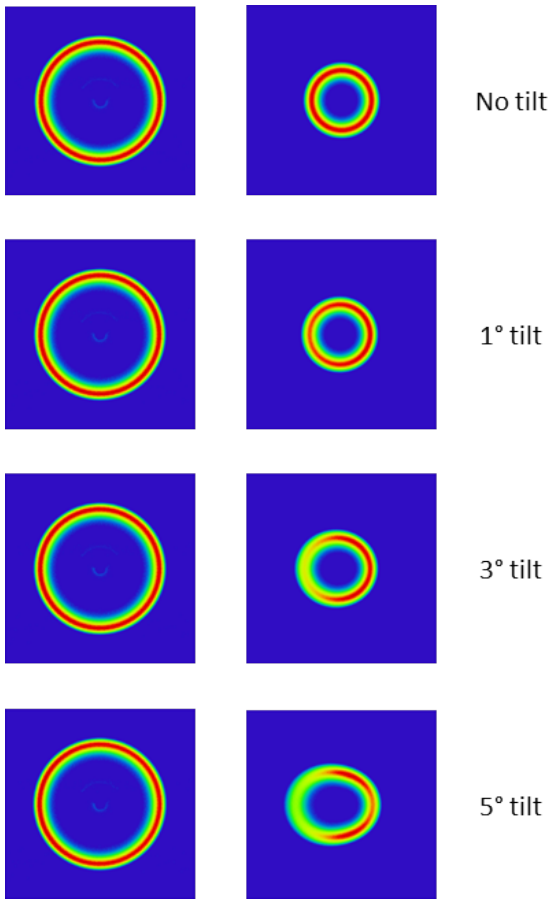

Figure 5.9: Effect of tilt of first axicon.

One interesting effect is the consequence of shifting or tilting the parabolic mirror. Although the ring focus should not be significantly affected by a shift along the parabola, there in fact is some change in the distribution, as shown in Fig. 5.11. The translational misalignment of the parabolic mirror causes an asymmetry in the heat distribution about the ring without affecting its shape. However, tilting the parabola changes the shape of the ring significantly. Similar to the effect of a shift in the axicons, a small amount of tilt causes the ring to distort into a cardioid. The cusp

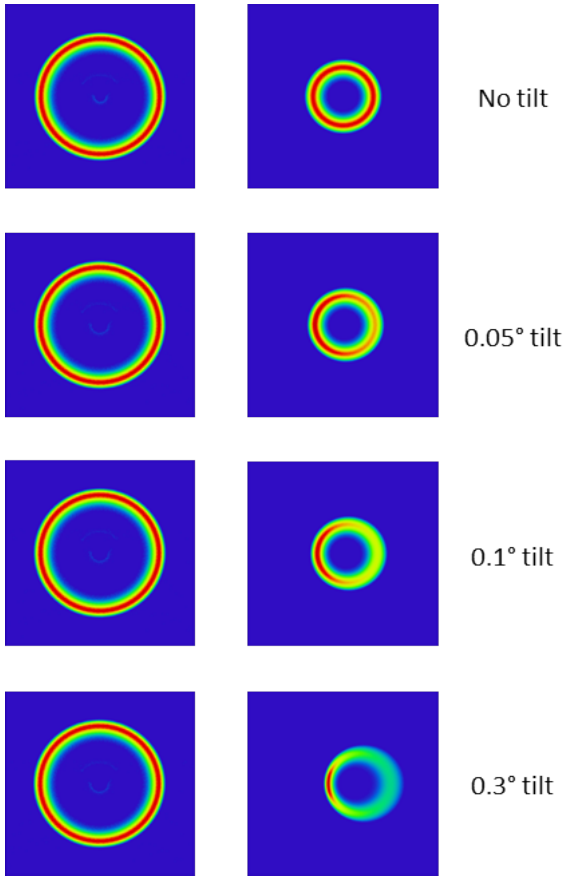

Figure 5.10: Effect of tilt of second axicon.

of the cardioid is in the direction which is lower than the horizontal plane. Proper alignment of the parabolic mirror is very important as not only does the tilt change the shape and intensity distribution of the focal ring, a small tilt moves the focus significantly.

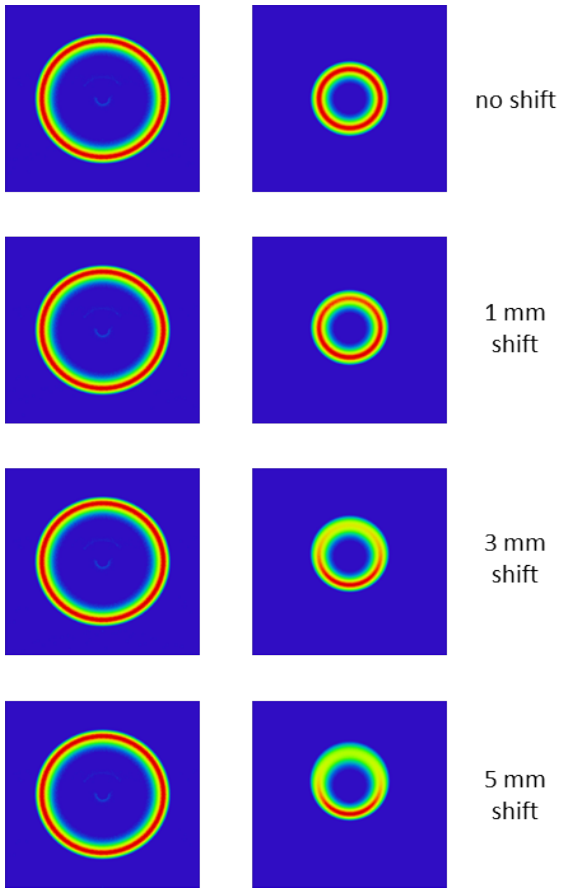

Figure 5.11: Effect of lateral shift of the parabolic mirror.

The results obtained from the simulations could be clearly seen in practice while aligning the optical components. In the images of Fig. 5.12, the first and the third column show the molten zone on top of the source from two mutually perpendicular sides. The second column shows the molten zone when viewed from the top. In Fig. 5.12b, the cardioid shape of the focus can be clearly seen. It was determined that this was caused by the angular misalignment of the parabolic mirror. In Fig. 5.12e, it can be clearly seen that the ring is thicker on one side than the other. This is due

to the translational misalignment and tilts of both the first and the second axicon. The tilts in this particular case dominate the shifts, as evident from the image. It should be noted that even though the side views in the upper row (Figs. 5.12a and 5.12c) seem symmetrical, the cardioid shape of the focus doesn't reveal itself unless viewed from the top.

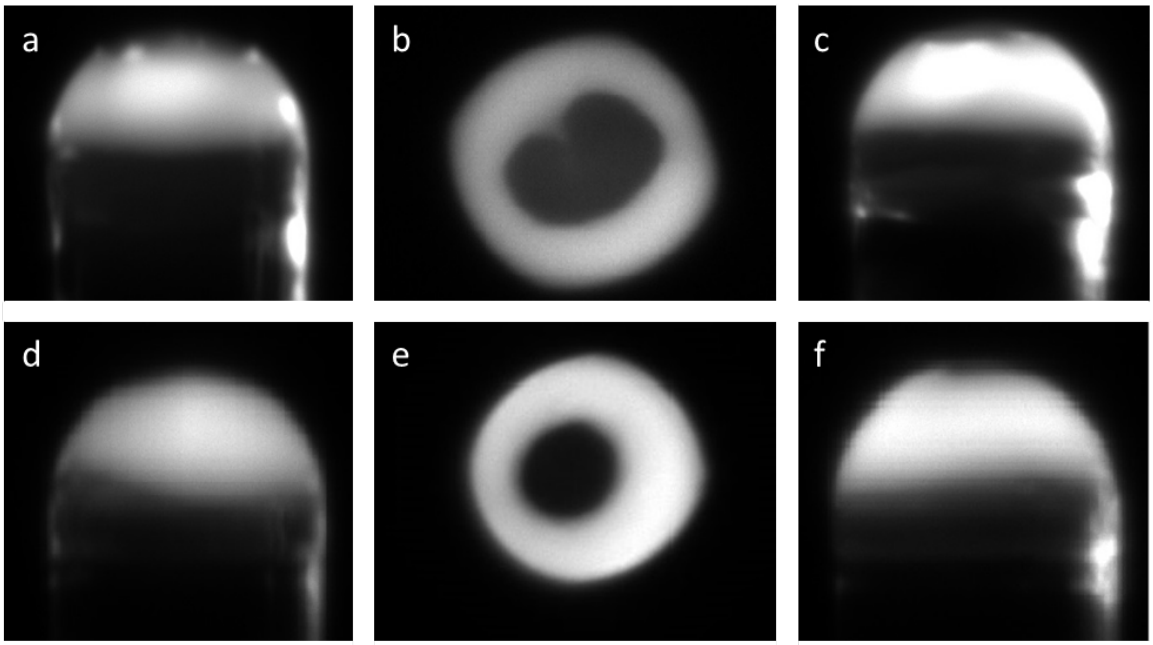

Figure 5.12: Photographs of focus on a 340 μm source. The two rows show two different cases. The first and third columns show the source from the side. The two sets are recorded on cameras orthogonal to each other. The second column shows the view of the source from the top

The approach for aligning the optical system is sequential. A He-Ne laser beam, coaxial with respect to the CO_2 laser beam, is used to aid the alignment process. When all the optical components are properly aligned, the molten zone on top of the source bar should look like a symmetric ring as shown in Fig. 5.13 when viewed from the top.

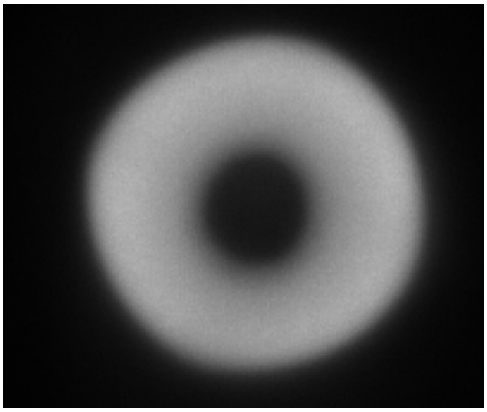

Figure 5.13: Photograph of symmetric focus achieved on a 340 μm source by fine-tuning alignment of components.

Part IV

Results and Discussions

Chapter 6

Loss Measurements

Attenuation represents one of the most significant characteristics of an optical fiber. Attenuation is the reduction in intensity of a signal as it travels through an optical fiber. The lower the attenuation losses are in an optical fiber, the lower will be the energy lost during transmission through the fiber. The optical power propagating in a fiber decreases exponentially with length. The attenuation losses can be mathematically expressed in terms of Beer's law which relates attenuation to the properties of material through which the light is propagating. The expression for transmission losses is given as

$$\alpha = -\frac{10}{l} log(\frac{P_{out}}{P_{in}}) \tag{6.1}$$

where P_{in} and P_{out} represent the power at the input and output of the fiber. The losses are expressed in the form of decibels per length where length is in the unit of l. The origin of transmission losses has been discussed in a previous chapter. In general, the total attenuation losses are a sum of scattering, absorption and bending losses. Several factors determine the total losses in a fiber. These include wavelength of light, refractive indices of core and cladding, shape and size of core and cladding, etc.

Attenuation can be measured by two different methods, cutback method and

insertion loss method. The cutback method is a destructive technique of determining the optical losses in a fiber. For the determination of attenuation coefficient of a fiber by cut-back method, the power output through a long piece of fiber is measured. Then the fiber is cut at a position near the launch end and the power output of the short section is measured. The power outputs of the long and the short sections are compared to yield the losses due to the residual section.

$$\alpha = -\frac{10}{L_1 - L_2} log\left(\frac{P_2}{P_1}\right) \tag{6.2}$$

where P_1 and P_2 represent the output power through the initial and cutback sections respectively, and L_1 and L_2 represent the length of the initial and cutback sections respectively. The principle advantage of the cut-back method is that it allows for the measurement of losses without introducing errors due to changes in launch condition. Coupling efficiency of a laser into a fiber is affected by different factors like the launch angle, polish of the fiber end face, focal length of coupling lens, etc. Effect of such variations on the measurement can be avoided by using the cutback method as it preserves the launch conditions between the initial and cutback sections. However, in spite of this advantage, the cutback method posed two major difficulties in measuring losses in SC fibers. The cutback method is a destructive method, so lengths of fibers are lost during the measurement process. The SC fibers grown for the study had very limited lengths, usually about 70 cm or less. Hence, a destructive method of measurement was not preferred. The cutback method is suitable for glass fibers as these fibers cleave to form clean flat faces with negligible surface roughness. However, cutting SC fibers mostly does not yield cleanly cleaved faces and require further polishing. This, along with the limited length of the fiber, would require the removal for the fiber from the attenuation measurement apparatus. Removing the fiber out of the set-up would void the advantage of uniform launch condition between the initial

and cutback sections. Due to these drawbacks, measurement of insertion losses is preferred for SC fibers.

In the insertion loss technique, for a section of fiber, the corrected power at input and output are considered to measure the attenuation coefficient. The correction is due to Fresnel reflection at the fiber faces. For normal incidence in air, the fraction of power reflected at the interface is given by

$$R = \left(\frac{n-1}{n+1}\right)^2 \tag{6.3}$$

where n is the refractive index of the material. Hence if P_{lens} is the power measured after the coupling lens, then the power coupled into the fiber cannot exceed $(1 - R)P_{lens}$. Similarly, if the power measured at the output of the fiber is given by P_{out}, the power at the end of the fiber would be given by $P_{out}/(1 - R)$. For insertion loss measurement, the coupling efficiency also needed to be considered. The correction due to the Fresnel reflection at different wavelengths are calculated in Table 6.1. These values were calculated based on the refractive index of YAG at different wavelengths as given in Fig Y. Using the corrected values for the power, the attenuation coefficient can be calculated using the following equation

$$\alpha_t = -\frac{10}{l} log\left(\frac{P_{out}/(1-R)}{k(1-R)P_{lens}}\right) \tag{6.4}$$

where k is the coupling efficiency of the laser into the fiber. Depending on the beam quality of the laser source and the diameter of the fiber, the value of k varies. However, for fiber with diameter greater than 200 microns, its value can be assumed to be unity.

Attenuation measurements of the crystal fibers were made at different wavelengths. The principal wavelengths used were 532 nm, 660 nm, 808 nm, and 1064 nm. Several measurements were also carried out at 1908 nm and 2940 nm. The characteristics of these laser sources are described in Table 6.2 .

Wavelength	YAG refractive index	R	1-R
532 nm	1.838	0.087 mrad	0.913
661 nm	1.827	0.086 mrad	0.914
808 nm	1.821	0.085 mrad	0.915
1064 nm	1.814	0.084	0.916

Table 6.1: Correction due to reflectance at different laser wavelengths

Wavelength	Maximum Output Power	Divergence	Beam Diameter	Source
532 nm	50 mW	<1.5 mrad	1.2 mm	Opto Engine
661 nm	150 mW	<1.0 mrad	1.1 mm	Vortran
808 nm	100 mW	<1.0 mrad	3.5 mm	Opto Engine
1064 nm	210 mW	<1.5 mrad	1.5 mm	Opto Engine

Table 6.2: Lasers used for loss measurements

The laser source was coupled into the fiber using a 9 cm focal length borosilicate lens. Due to the high refractive index of YAG and the absence of a cladding layer for the SC fibers, the theoretical numerical aperture of the YAG fibers is very high. This allows for the acceptance of light at all angles into the fiber, allowing propagation for all angles more than 33°.

For a straight section of fiber, the total attenuation is a result of absorption and scattering. The scattering contribution, which represent a major fraction of the losses, originate from factors like bulk scattering, surface roughness and fluctuation in fiber diameter. A two-inch integrating sphere (Thorlabs IS200) with a silicon photoconductive detector was used to measure the scattering contribution to the total losses at different wavelengths. Using the same method described in the total attenuation measurements, the laser beam was coupled into the YAG SC fiber and the scattering sphere was moved along the length of the fiber, recording the scattering values every 5 mm. Unlike similar studies for glass fibers, no index-matching fluids were used at the output end of the fiber. Because of the high refractive index of YAG, obtaining refractive index matching fluids was difficult and hence the output end was left exposed to air. This introduces higher scattering at the output end due

to light reflected from the output end face of the fiber. The loss due to scattering was calculated using,

$$dI_s = -I(x)\alpha_s dx = -I_0 exp(-\alpha_t x)\alpha_s dx \tag{6.5}$$

where dI_s is the intensity of light captured in the integrating sphere with diameter dx = 5.08 cm; I(x) is the intensity of the light at position x along the fiber; α_t is the total attenuation losses in the fiber. I(x) was calculated by considering the power coupled into the YAG SC fiber and the total attenuation of the fiber.

6.1 Results for 330 μm SC fibers

As stated earlier, one of the biggest obstacles in fabricating a single-crystal based fiber laser has been the high attenuation losses associated with SC fibers. Fibers grown during the initial period of the project were characterized by very high losses, usually no less than 10 dB/m. These fibers displayed poor crystal quality and significant variation in diameter and fiber geometry. Some samples even exhibited internal cracking due to large amount of strain. The poor quality which resulted in high losses was due to a combination of different factors like poor optical alignment, inconsistencies in the fiber pulling mechanism, and instability of the CO_2 laser power. A important observation that was noted for these fibers was the almost monotonic increase of scattering losses down the length of the fiber. Such an observation was highly suggestive of large scattering losses by coupling of power into higher order modes. From a simple geometrical point of view, imperfections in the crystal bulk and on the fiber surface modify the conditions for total internal reflection of the guided rays until the conditions are not satisfied anymore. At this point, the light is not guided anymore and is lost through the surface of the fiber as scattered light. This effect is cumulative and causes the steady increase of the scattered power along the length of

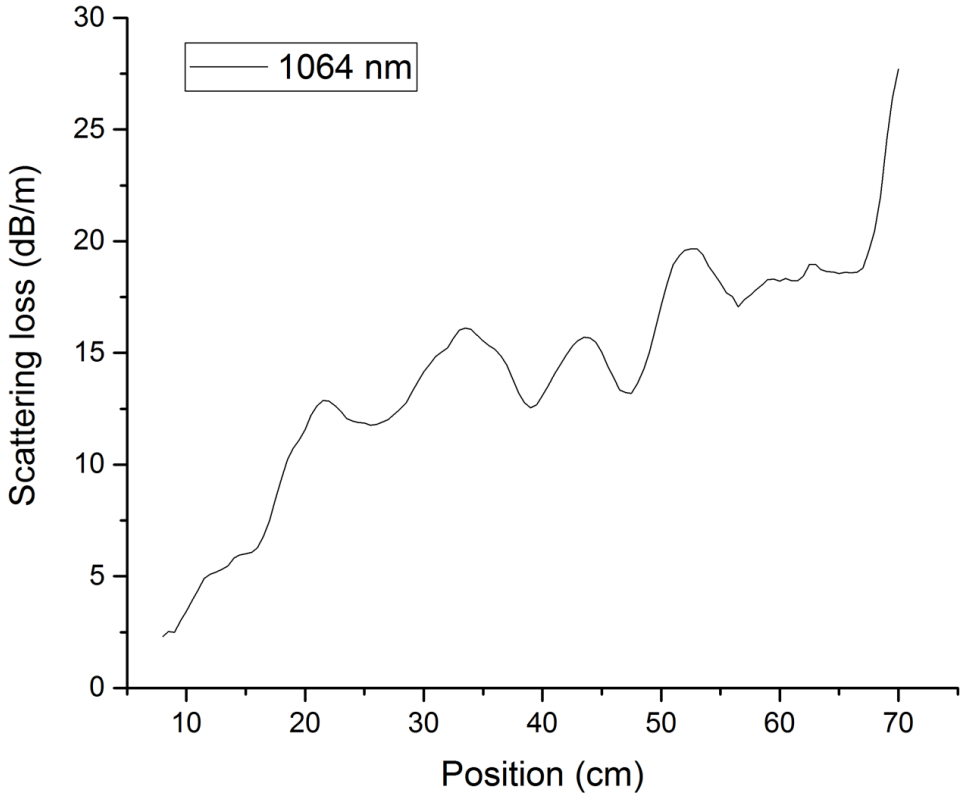

Figure 6.1: Scattering losses along the length a 79-cm long 330 μm diameter YAG SC fiber at 1064 nm

the fiber.

The scattering loss in one such high-loss YAG SC fiber is shown in Fig 6.1. Although the measurement was done at 1064 nm, it was representative of the scattering behavior at other wavelengths as well. This particular sample was a 79 cm long undoped YAG SC fiber with a 300 μm diameter. The attenuation losses of this fiber were measured to be 28.68 dB/m, 22.13 dB/m and 15.97 dB/m at 532 nm, 635 nm and 1064 nm, respectively. The scattering losses in this fiber exhibit an increasing trend along the fiber length, indicating the loss of power by coupling to higher order modes.

For the fiber described in the previous section, a 15.97 dB/m means that neglecting loss due to coupling, only 2.5% of the optical power launched into the fiber can measured at the output. At such high losses, these fibers cannot be used in any practical applications. Hence quality of the fibers had to be improved drastically to continue to explore the idea of using these fibers as active media for high power lasers. Since then, major modifications were applied to the LHPG system to improve the fiber quality. The most significant of the changes was the application of a double axicon optical system in place of a reflaxicon system. Observable changes in fiber quality were observed when the axicon system was commissioned. Improving the power stability of the CO_2 laser also contributed to the improvement of the fiber quality. These changes, along with optimizing the alignment of the optical components, allowed for the consistent growth of YAG SC fibers with losses less than 1 dB/m.

One of the fibers that stood out in terms of quality was a 1m long 335 μm diameter undoped YAG fiber. The attenuation losses for the fiber at different wavelengths is shown in Fig 6.2. At 1064 nm, the fiber had a loss of 0.3 dB/m, which means only 7% of the light launched into the fiber was lost. This is a stark improvement compared to the high-loss fiber described earlier. The remarkable consistency of the fiber quality over the entirety of its length was borne out in the scattering measurement as it did not show a strong increase in loss along its length (see Fig. 6.3). The scattering losses remained fairly constant at less than 0.2 dB/m for the majority of the length of the fiber.

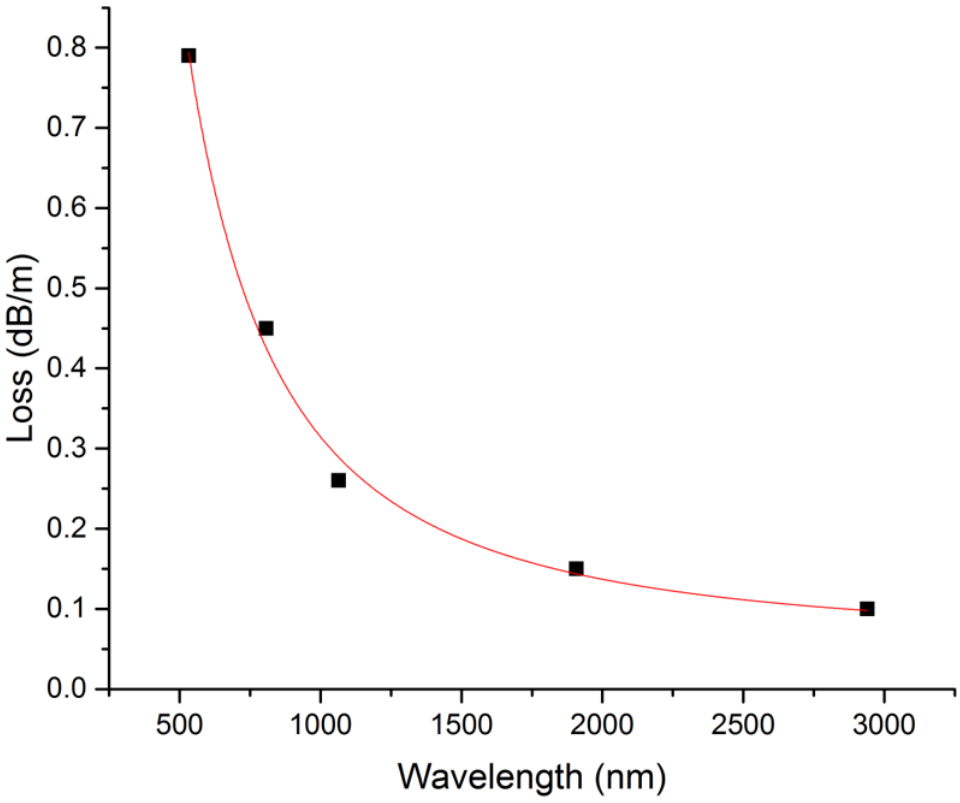

Figure 6.2: Total attenuation losses for a 1 meter long 330 μm diameter YAG SC fiber at different wavelengths

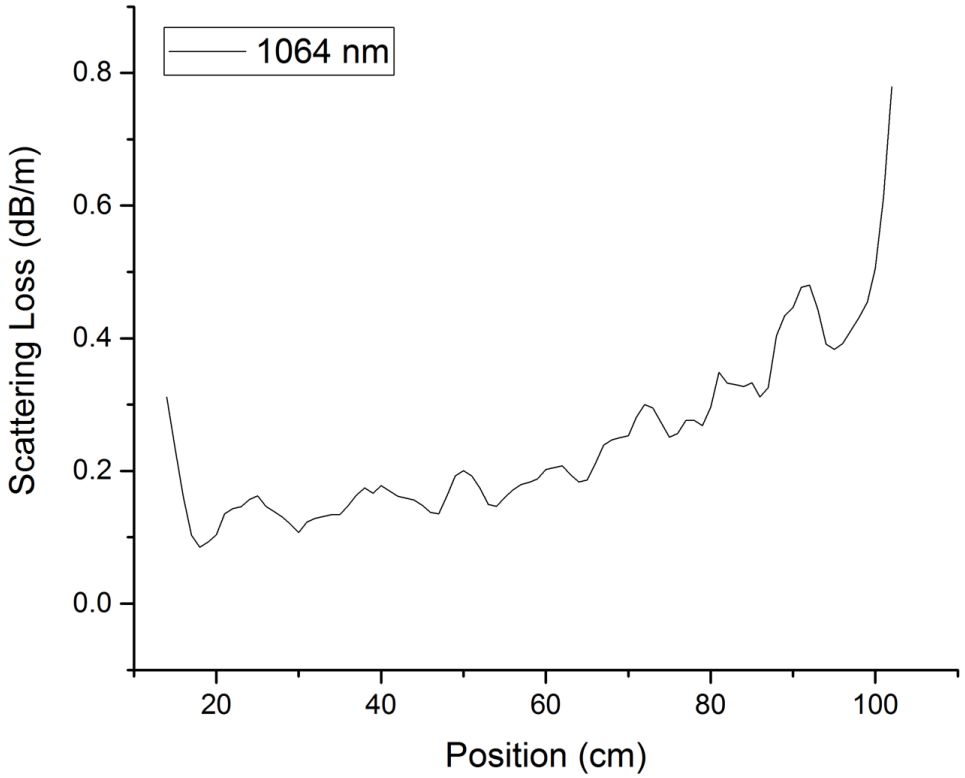

Figure 6.3: Scattering losses in a 1 meter long 330 μm diameter YAG SC fiber along its length at 1064 nm

Using the improved optical alignment, low-loss doped YAG SC fibers were grown as well. Since a lot of the lasing experiments were focused on lasing transitions in Ho^{3+} ions, 0.5% Ho:YAG fibers were grown. It is worth mentioning here that since the Ho^{3+} ion absorbs at 532 nm and in the red, attenuation measurements were limited to 808 nm and 1064 nm. The lowest loss measured for a 0.5% Ho:YAG fiber was 0.6 dB/m, which is comparable to the losses in the undoped fibers. The lasing characteristics of low-loss 0.5% Ho:YAG SC fibers are described in a later chapter.

6.2 Results for 120 μm SC fibers

The losses in 120 μm fibers were lowered considerably over the course of the entire work with ultimate losses well below 1 dB/m. Previous works have indicated that the total loss scaled with the diameter of the fiber [80]. The total attenuation losses

increased with decreasing fiber diameter. A possible explanation for this is likely due to increased scattering losses. The number of bounces of light while being wave guided through a smaller diameter fiber is more than that of a larger diameter. Since the SC fibers are not clad, increased number of bounces increases the scattering losses in the fibers. Growing SC fibers with diameters of the order of 120 μm was also more involved compared to fibers of 340 μm, as this requires more precise alignment of the optical components to obtain a more uniform focus of the CO_2 laser beam. The improvements in alignment were assisted by the results obtained from the simulations using the optical ray-tracing software described in a previous section. Using improved alignment of optical components, attenuation losses have been reduced from about 10 dB/m to less than 1 dB/m. To date, the lowest measured loss for a 120 mm diameter YAG SC fiber at 1064 nm is 0.3 dB/m. The attenuation losses measured at different wavelengths for a different 30 cm long, 120 μm diameter YAG SC fiber is shown in Fig. 6.4 The error bars indicate changes in measurement due to varying power and coupling into the fiber. The figure shows an increasing total attenuation loss in the fiber with decreasing wavelength. The increase in total attenuation losses in the fiber with decreasing wavelength is mostly due to increased scattering losses. The losses appear to have a $\lambda^{-2.4}$ dependence on wavelength.

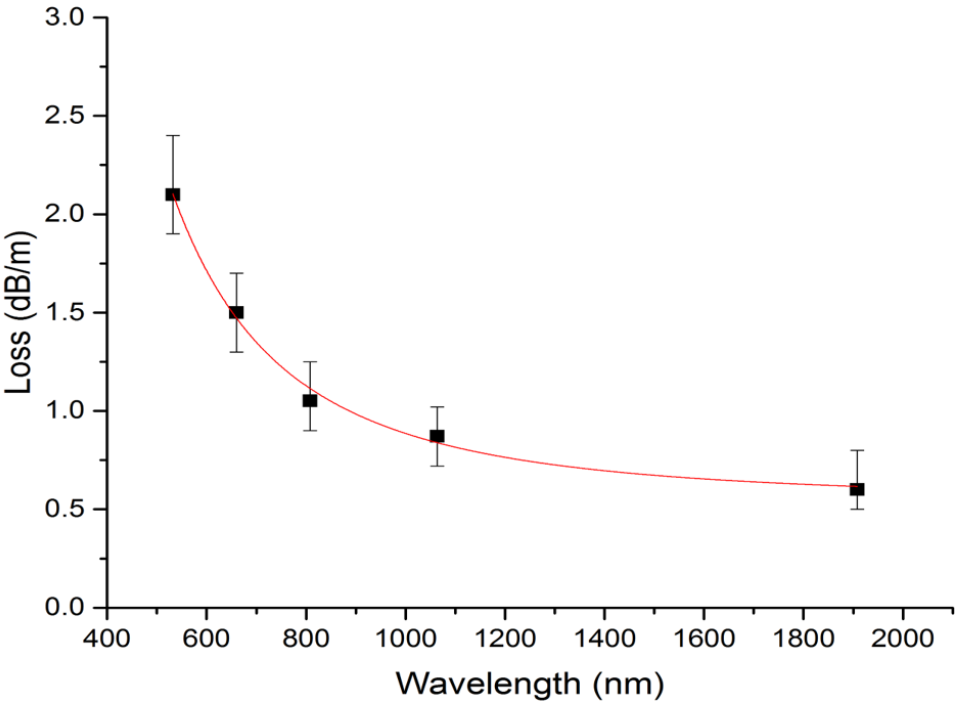

Figure 6.4: Total attenuation losses for a 30-cm long 120 μm diameter YAG SC fiber at different wavelengths

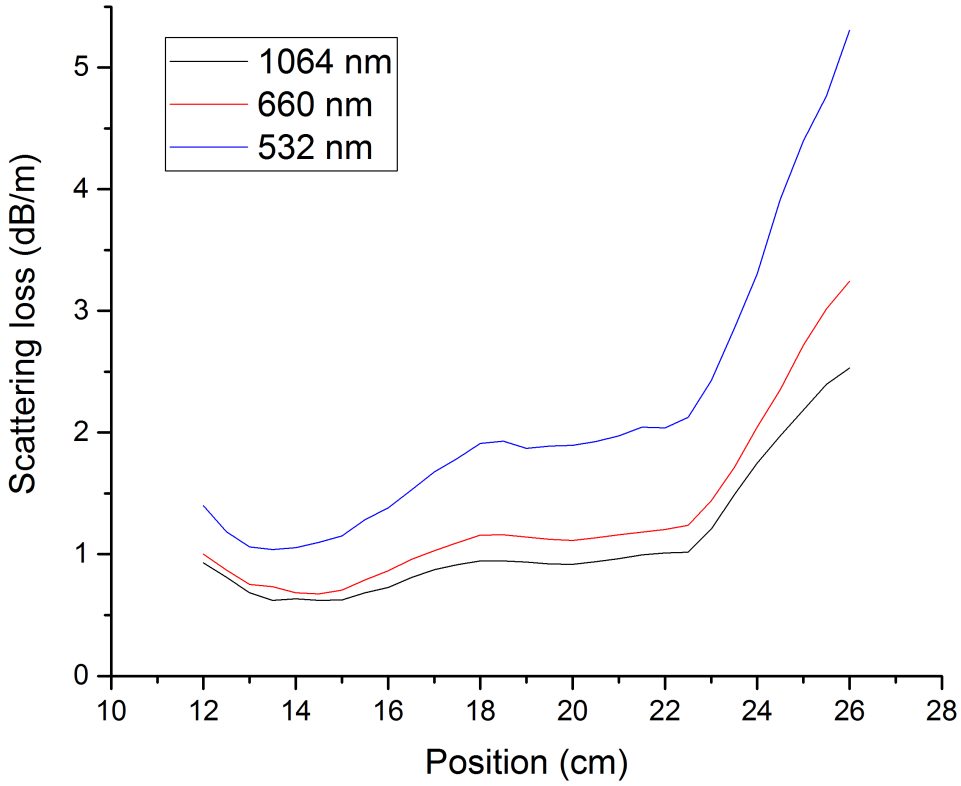

Figure 6.5: Scattering losses in a 30-cm long 120 μm diameter YAG SC fiber along its length at three wavelengths, 532 nm (top), 660 nm (middle) and 1064 nm (bottom).

Figure 6.5 shows the scattering losses along the length of a particular fiber measured at three different wavelengths. In the figure, the curves from top to bottom show scattering at 532 nm, 660 nm and 1064 nm respectively. For this particular fiber, the total attenuation losses are 2.1 dB/m, 1.4 dB/m and 0.9 dB/m at 532 nm, 660 nm and 1064 nm respectively. The scattering data at both wavelengths shows increased losses at about 12 cm and 19 cm along the fiber. The increased scattering losses in these sections of the fiber was due to "hotspots" or pronounced defects in the fiber. Scattering also increased along the length of the fiber. In general, the 120 μm fibers displayed a consistent increase of losses with increasing length. While fiber sections with length less than 20 cm consistently showed losses of less than 0.5 dB/m (at 1064 nm), longer fibers displayed higher losses. This is likely to be due to increase in radiation losses along the length of the fiber. Fluctuations in the fiber diameter can cause initially bound rays to become leaky as they are propagating down the fiber and lose power by radiation. The 120 μm fibers showed a diameter variation of about 1.5% which is considerably higher than the 330 μm fibers which showed a variation of about 0.5%. This is the likely reason behind the higher length dependence of the small diameter fibers.

As evident from Fig. 6.5, scattering losses increased with decreasing wavelength. The intensity of scattered light varies as λ^{-n}, where n depends on the particular mechanism of scattering. Depending on the size of the scattering species, n can be 4 for Rayleigh scattering, 2 for Rayleigh-Gans scattering, and 0 for Mie or Tyndall scattering. In our case, it is seen that the best fit is a $\lambda^{-2.4}$ dependence suggesting that the scattering occurs due to Rayleigh-Gans scattering. However at this point, we do not have any more details about the scatterers.

As a part of the lasing characteristics experiment, 0.5% Ho:YAG SC fibers were also grown at 120 μm diameter. Calculations regarding the optimum length to 0.5% Ho:YAG SC fiber required for maximum lasing output show that length required was

no more than 20 centimeters. Hence the lengths of 120 μm 0.5% Ho:YAG SC fibers were limited to 25 cm. For these lengths, the losses measured in the doped YAG fibers at 1064 nm were in good agreement with undoped fibers of similar diameter. For example, a 17.5 cm long 0.5% Ho:YAG SC fiber showed a loss of 0.5 dB/m.

Optical fibers demonstrate additional losses when bent. The losses due to bending increase sharply if the bending radius is smaller than a critical value. The critical radius of bend is typically smaller for higher order modes. The SC fibers grown for this project are highly multimode in nature and as expected their losses increase on increasing the curvature of a bend. The change in attenuation losses (at 1064 nm) for a 30-cm long 120 μm diameter YAG SC fiber with increasing curvature is shown in Fig. 6.6.

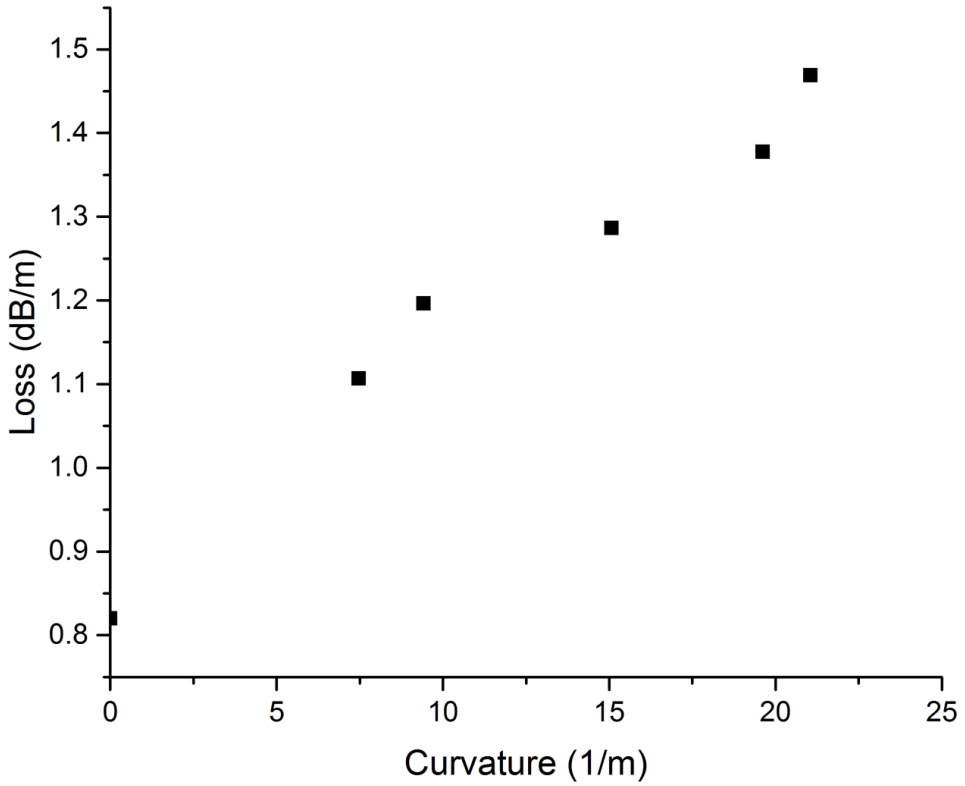

Figure 6.6: Increase in losses in a 30-cm long 120 μm diameter YAG SC fiber with increasing curvature of bending.

Chapter 7

Cladding a Single Crystal Fiber

A step-index optical fiber is the most extensively used form of an optical waveguide. It consists of a central core region, clad by a layer of dielectric material of a lower refractive index. Such an arrangement causes the light to be confined in the core region by total internal reflection at the core-cladding interface. In most practical applications, the fiber must be supported. Direct contact of the fiber core surface with the supporting structure may modify the condition for total internal reflection and thereby affect waveguiding in the fiber. The presence of the cladding layer prevents such a situation, as the interface at which the total internal reflection takes place is shielded from external contact. Additionally, the presence of the cladding layer also prevents light from leaking between individual fibers in fiber bundle. In most optical fibers the cladding layer is chosen such that its refractive index is slightly lower than that of the core. In other words, if n_1 and n_2 are the core and cladding refractive respectively, then the index step, Δ, is very small. Δ is defined as

$$\Delta = \frac{n_1 - n_2}{n_1} \tag{7.1}$$

Under such condition, the optical modes propagating in the fiber can be assumed to be weakly guided. This assumption simplifies the mathematical analysis of the

modes in the fiber, allowing simple approximate solutions for the cut-off conditions. Furthermore, in multimode step-index fibers, dispersion increases as Δ increases. So even though a smaller value of Δ decreases the acceptance angle for the fiber, it is preferred for multimode fibers as it preserves pulse shape.

While the single clad structure is well-suited for telecom and low power active fibers, it is not sufficient for high power active fibers. For a lot of applications, a single mode diffraction limited output is desirable from fiber lasers. For single clad active fibers, such a condition limits the option of pump sources to diffraction limited sources, which are normally low-power sources. While increasing the size of the core would allow pumping by high power sources, output mode quality would be sacrificed. A double clad fiber geometry solves this problem by allowing cladding-pumped configuration where the pump laser is coupled into the inner cladding. As the pump wavelength propagates through the fiber, it excites the laser active ions in the core, leading the emission at laser wavelength. The laser beam, unlike the pump beam, is confined to the smaller core region, thereby maintaining a good mode quality at the output. The inner cladding is usually much larger compared to the core region, resulting in a very high numerical aperture for these fibers. The large numerical aperture allows for the pumping by cheap broad area pumps like diodes. The pump light is not required to be coupled into the end faces but can also be side-pumped into the fiber where the pump sources are perpendicular to the laser beam direction.

In conventional glass fibers, the core and the cladding region of the fiber are drawn simultaneously. A monolithic fiber preform, composed of higher refractive index core rod and lower refractive index outer tube, is used as the starting material for an optical fiber. The preform is softened by a furnace and drawn to a small diameter fiber. In the softened state, the high viscosity of the glass phase prevents the mixing of the core-rod and outer-tube regions, thereby transferring any cross-sectional geometry

from the preform to the fiber. As glasses have relatively open structure, it is relatively easy to modify properties like refractive index and thermal conductivity in glasses by introducing suitable dopants. However, the growth of a core-clad structured fiber is not straight-forward in the case of SC fibers. During the growth of such fibers, the melt from which the fiber is pulled is in a true liquid state. The low viscosity in the liquid melt, tends to homogenize the composition of the melt and hence of the pulled crystal. Diffusion in the melt leads to a uniform melt which restricts the transfer of any refractive index profile from the preform to the drawn fiber. This difficulty in growing a true core-clad structured single crystal has been one of the principal challenges in developing a SC fiber laser system. In the following sections, a few different approaches to cladding SC fibers have been discussed.

7.1 Glass Clad SC fiber

For a functional step-index fiber, the cladding layer needs to have a refractive index slightly lower than that of the core region. Since refractive index of glasses can be easily modified by introducing ions like boron, aluminum, etc., the idea of designing a glass composition with a refractive index slightly lower than that of YAG and cladding SC fibers with that glass has generated a considerable amount of research interest. One idea to achieve this goal would be to form a preform with a SC rod and a glass tube. The composition of the glass is chosen such that not only is its refractive index slight lower than the crystalline core material, but the coefficient of thermal expansion of the glass also matches that of the crystal. When such a preform is introduced into a fiber pulling apparatus, the limited solubility of the core material in the glass layer prevents the homogenization of the composition and transfers a core-clad structure to the drawn fiber. During the drawing process, the high viscosity glass cladding layer acts as a crucible where the core is melted. As the fiber is grown the molten core

and the glass "crucible" form the core and cladding of the fiber respectively. This technique also allows the core rod in the preform to be replaced by a densely packed column of powder which can form the molten core. While there is some dissolution of the core into the cladding, this method does yield long lengths of fibers with a stable core-clad geometry.

While alumina molten-core crystal fibers have been well documented, drawing YAG molten-core crystal fibers is fairly difficult to achieve. This is perhaps due to the crystallographic complexity of YAG and the dissolution of high amount of silica into the core. However, Huang *et al* have demonstrated the Cr:YAG molten core fibers for broad band amplifiers using their co-drawing LHPG (CDLHPG) technique [83] (see Fig. 7.1). While most of the other efforts using a similar configuration have yielded all-glass fibers [84], their group was able to verify crystallinity of the core region with transmission electron microscopy [85]. For smaller core sizes, these fibers displayed a core diameter variation of around 20%, which perhaps explains the high transmission losses in these fibers (>30 dB/m at 1550 nm) [83].

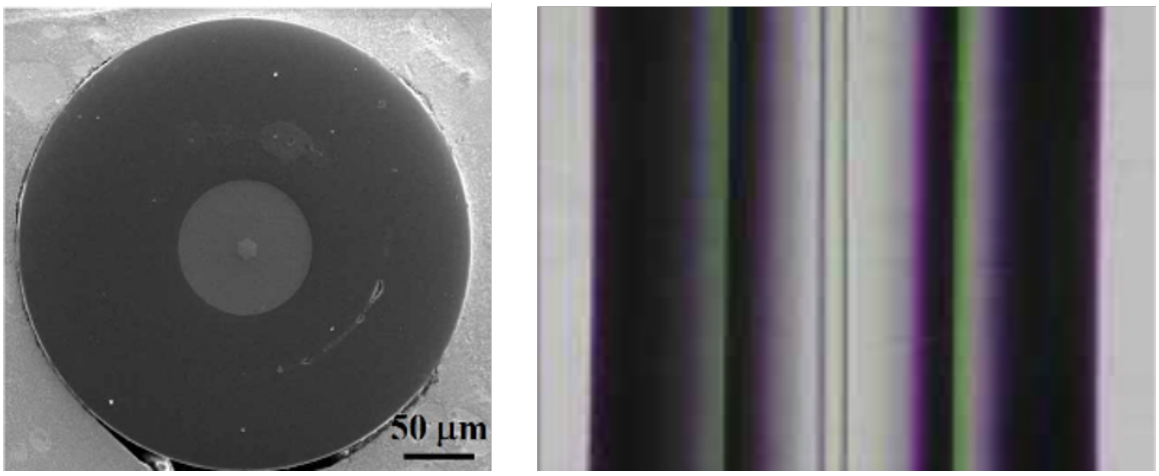

Figure 7.1: Cr^{4+}:YAG double-clad crystal fiber fabricated by the sapphire tube assisted CDLHPG technique. [83] (Reprinted with permission)

A second approach to glass cladding a crystal fiber would be to apply a cladding layer on an already grown SC fiber. A glass-cladding can be obtained either by extru-

sion or by a deposition process (like OVD or ion sputtering) followed by vitrification. Using the extrusion method, Digonnet *et al.* were able to clad 125 μm Nd:YAG SC fibers with high index glass with an index step of 0.048 [86]. Recently, Shaw *et al.* have demonstrated glass cladding of Yb:YAG SC fibers using a post growth cladding technique [87]. They were able to demonstrate a 230 μm double-clad fiber with a 35 μm core. The properties of the inner cladding glass was tailored to be make the index step less than 0.002. Fiber quality grown by this technique was not very good and the fibers showed fairly high losses (about 15 dB/m).

7.2 Crystal clad SC fiber

While the properties of glasses can be tweaked heavily by modifying their composition, they cannot be made to completely mimic crystalline materials. Crystals and glasses are different classes of solids which are defined by vastly different physical properties. The lack of a long-range ordering in glasses affects their thermal and mechanical properties significantly. Such a disparity in properties renders the glass claddings incompatible for crystal fibers for high temperature applications. Hence for high power fiber laser applications, glass clad SC fibers have found limited success. This has turned the focus on the development of a crystalline cladding for SC fibers. However there are serious challenges is growing an all-crystalline core-clad fiber. While crystals have high thermal conductivity that is essential for high power applications, unlike glasses, properties of crystals cannot be easily modified by introducing dopants. Introduction of dopants in crystals usually occurs via substitution of ions in the lattice and is not kinetically very favorable and generally requires highly sophisticated techniques to succeed. Hence the choices of cladding material is very limited. Nevertheless, there have been various attempts to fabricate an all crystal core-clad structure. Mu *et al.* were the first to demonstrate such a structure [88].

There were able to fabricate a rectangular crystal waveguide by bonding undoped YAG bars to a 40 μm doped YAG core crystal using adhesive-free bonding technique. Using the same technique, they were able to fabricate a double-clad structure with an outer cladding of spinel. The index step Δ at the inner and outer interfaces were 0.002 and 0.113 respectively. Using such a structure, they were able to obtain a laser output with slope efficiency of 78%. While such a structure was demonstrated to function as a laser, it was not a true crystal fiber waveguide. The structure was very rigid and not amenable to coiling like regular glass fibers.

Approaches to growing all-crystal core-clad fibers can be broadly classified into two categories:

i. Post-cladding techniques

ii. In-situ cladding

Post-cladding techniques, as the name suggests, involve the growth of the cladding layer on an already grown SC fiber. In-situ cladding, on the other hand refers to the approach of obtaining a transverse refractive index by manipulation of ions while the crystal fiber is being grown.

7.3 Post-cladding techniques

One of the principal challenges in growing a crystalline cladding layer on crystal fibers is due to the curved growth surface. Such a cylindrical geometry makes is difficult to use traditional physical deposition processes like sputtering, pulsed laser deposition, molecular beam epitaxy, etc. Efforts have been made to use such techniques by rotating the fiber along its axis during the deposition process. While theoretically such an approach seems very favorable, in practice it is very difficult to execute, often leading to considerable fluctuation in cladding thickness along the fiber length. On the other hand, chemical vapor deposition (CVD) techniques yield conformal coating

and would be ideally suited for growing a crystalline cladding on the fibers. However, CVD processes for mixed oxides usually require complex starting chemicals and precise control over flow rates of the chemicals, making such processes very involved and expensive. While it is possible to devise experiments to investigate the feasibility of CVD processes in fabricating crystalline cladding for SC fibers, such studies require considerable planning and capital. And unsurprisingly, no such study has been reported to date. All these limitations have led to the exploration of solution based techniques to grown a crystalline cladding.

7.3.1 Sol-gel Cladding

Among the post-cladding techniques, sol-gel derived claddings have been extensively studied under this project. Sol-gel processing can be described as the wet-chemical processing of ceramic material by preparation of a colloidal sol, gelation of the sol and subsequent removal of the solvent. In this process, nanoparticles suspended in a solution condense to form networks upon the slow removal of the solvent phase. The network of particle grows with time and temperature, forming a gel, a continuous solid with fluid phase of colloidal dimensions. Structures of different shapes can be achieved by allowing the gelation of a sol in molds or different substrates. As the gel ages more, more liquid from the pores is expelled and the solid phase shrinks and dries. The dried gel is amorphous and crystallizes when heated. For the production of pore-free ceramic, treatment at higher temperature and longer period is required to affect sintering of the ceramic material. A flow diagram of the sol-gel coating process is shown in Fig. 7.2.

The principal advantage of the sol-gel processing technique lies in its simplistic nature. A huge variety of ceramic materials can be produced at low temperature, starting from rather simple chemicals. Since this process does not involve the use of sophisticated apparatus, it is a low-cost technique that can be performed in a

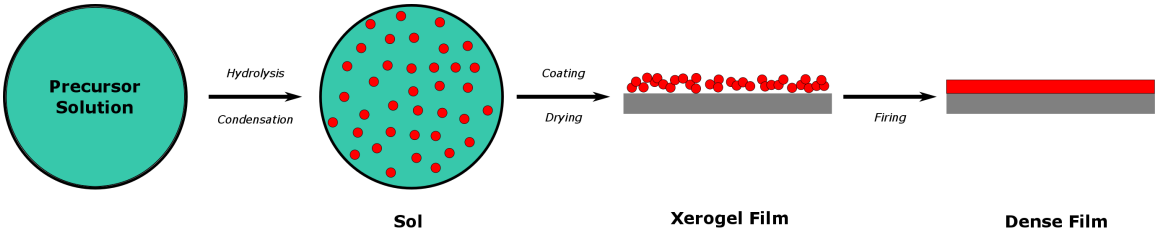

Figure 7.2: Flow diagram of a sol-gel film coating

simple chemical laboratory. Additionally, the sol-gel technique allows for conformal casting of the gel on substrates of random shape by the process of dip-coating. In its simplest form, sol-gel dip-coating involves the introduction and controlled withdrawal of a substrate in a sol. Subsequent gravitational draining, evaporation of solvent and condensation of the gel network result in the deposition of a solid film on the substrate. By varying the speed of withdrawal or changing the physical properties of the sol (like viscosity, surface tension and density), the thickness of the deposited layer can be controlled [89]. The schematic of a dip-coating set-up is shown in Fig. 7.3. Compared to other thin film deposition techniques like sputtering or CVD, the sol-gel dip-coating process does not require complicated instrumentation and hence is much simpler and cheaper.

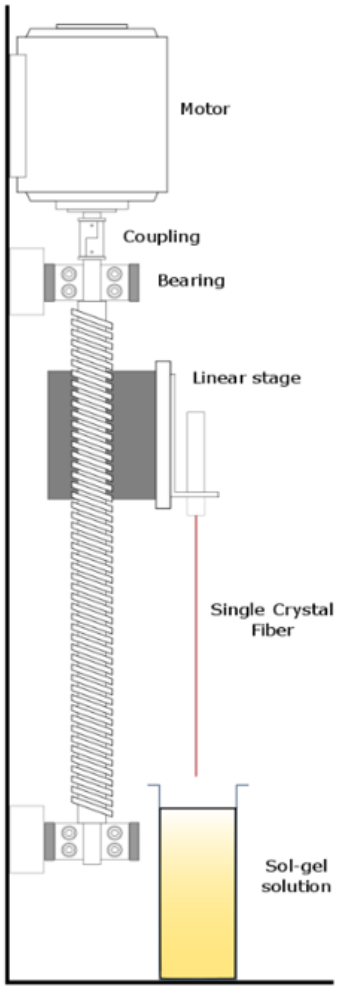

Figure 7.3: Schematic of a sol-gel dip-coating set-up

Alumina Sol-gel

Alumina, whose synthesis via sol-gel method has been well-established in literature was explored as a cladding material for YAG SC fibers. Since the refractive index of alumina is less than that of YAG (1.75 at 1064 nm), alumina could be considered for the cladding process.

Crystalline alumina was obtained through the sol-gel route by starting with aluminum *sec*-butoxide (ASB) as the precursor [90] (see Fig. 7.4 for flowchart). ASB was added to water at 75°C in the molar ratio of 1:100 (ASB to water). The hydrolysis of ASB raised the temperature to about 90°C and the mixture was held at this temperature for 15 minutes. Nitric acid was then added to the mixture to affect peptization. The molar ratio of HNO_3 to ASB was 0.3:1. The solution was maintained at the same temperature until it concentrated to half its original volume. The obtained alumina sol could be utilized for dip-coating or it could be dispersed in an ethanol solution to modify its surface tension. Ethanol was added in the molar ratio of 2:1 to ASB and the solution was vigorous shaken for thirty seconds and then ultrasonicated for 5 minutes. Cleaned fibers were dip-coated with the sol and allowed to age and dry for 24 hours after which they were dried in an oven for 30 minutes to expel any remaining moisture. Finally the coated fibers were sintered at 800°C for 10 hours. Figure 7.5 shows an alumina-clad 120 μm YAG SC fiber.

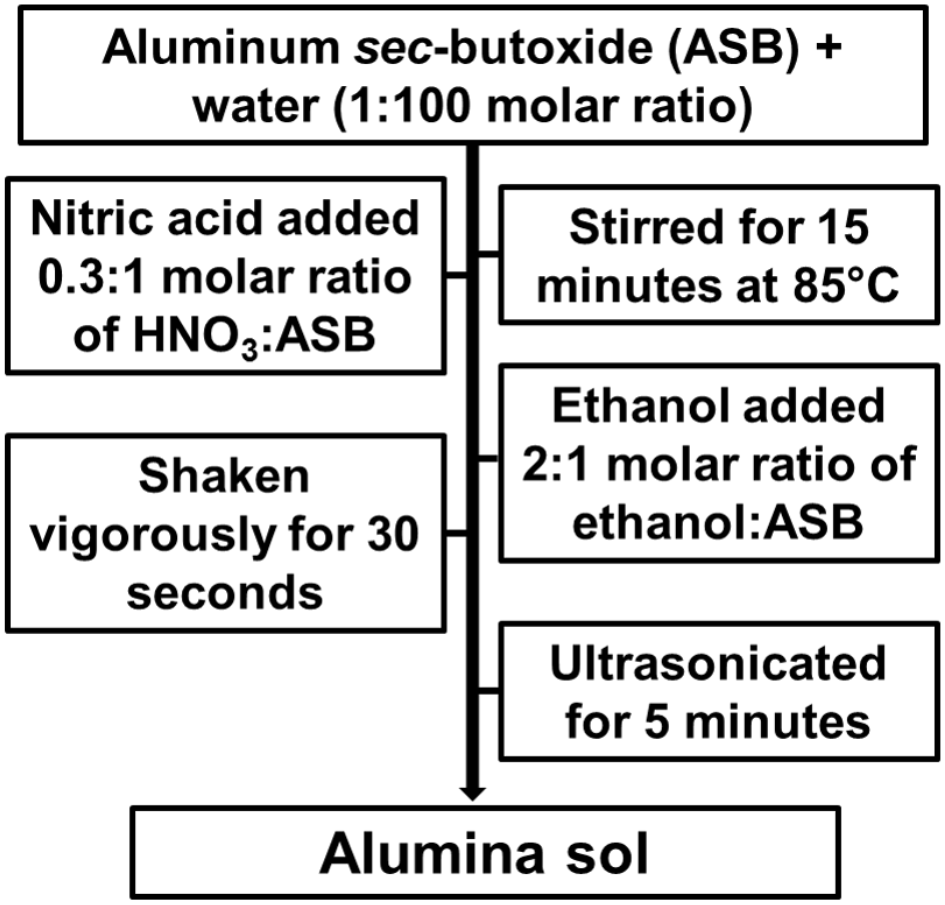

Figure 7.4: Flowchart describing preparation of alumina sol-gel

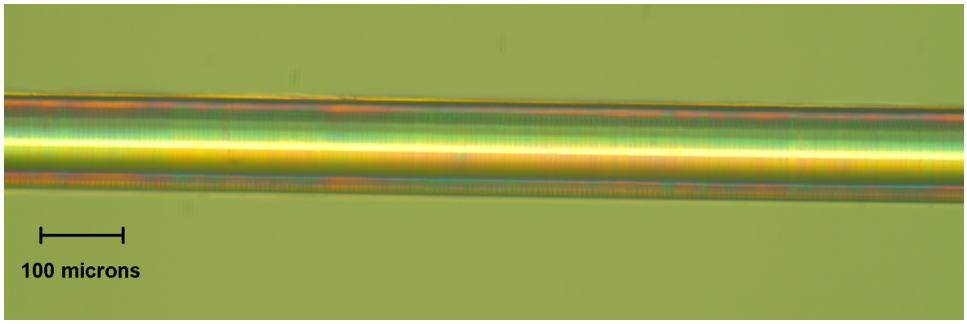

Figure 7.5: Alumina sol-gel deposited layer on a 120 μm YAG SC fiber

YAG Sol-gel

Unlike the case of an alumina sol-gel derived cladding, most physical properties of the sol-gel derived YAG cladding were very similar to that of the YAG crystal fibers. The extent of match of the properties of the core and the cladding layer depended on the densification of the sol-gel derived layer. Properties like thermal conduction and refractive index of the cladding layer were usually lower than that of the crystalline layer due to its porosity. In decrease the porosity in the cladding layer, it had to be treated at higher temperatures for longer duration.

YAG sol was synthesized using the glycolate sol-gel route, starting from metal acetates [91] (see Fig. 7.6. for flowchart). The sol-gel method offered excellent homogeneity through thorough mixing of starting materials. Moreover, the formation of extended networks in the gel phase due to the condensation of partially hydrolyzed species facilitated structural evolution and lowered the crystallization temperature. YAG was derived by the hydrolysis and condensation of yttrium oxide and aluminum nitrate by an acetate-glycolate path. Yttrium oxide was refluxed in 0.02 M acetic acid at 60-70°C for 6-8 hours to yield yttrium acetate. Aluminum nitrate was added to the solution and the solution was constantly stirred at 70°C for 2-3 hours. Finally, ethyl glycolate was added and the final solution was kept at the same temperature, slowly evaporating the dissolved water to raise the viscosity of the precursor sol. Although the viscosity was allowed to increase considerably, gelation was not reached.

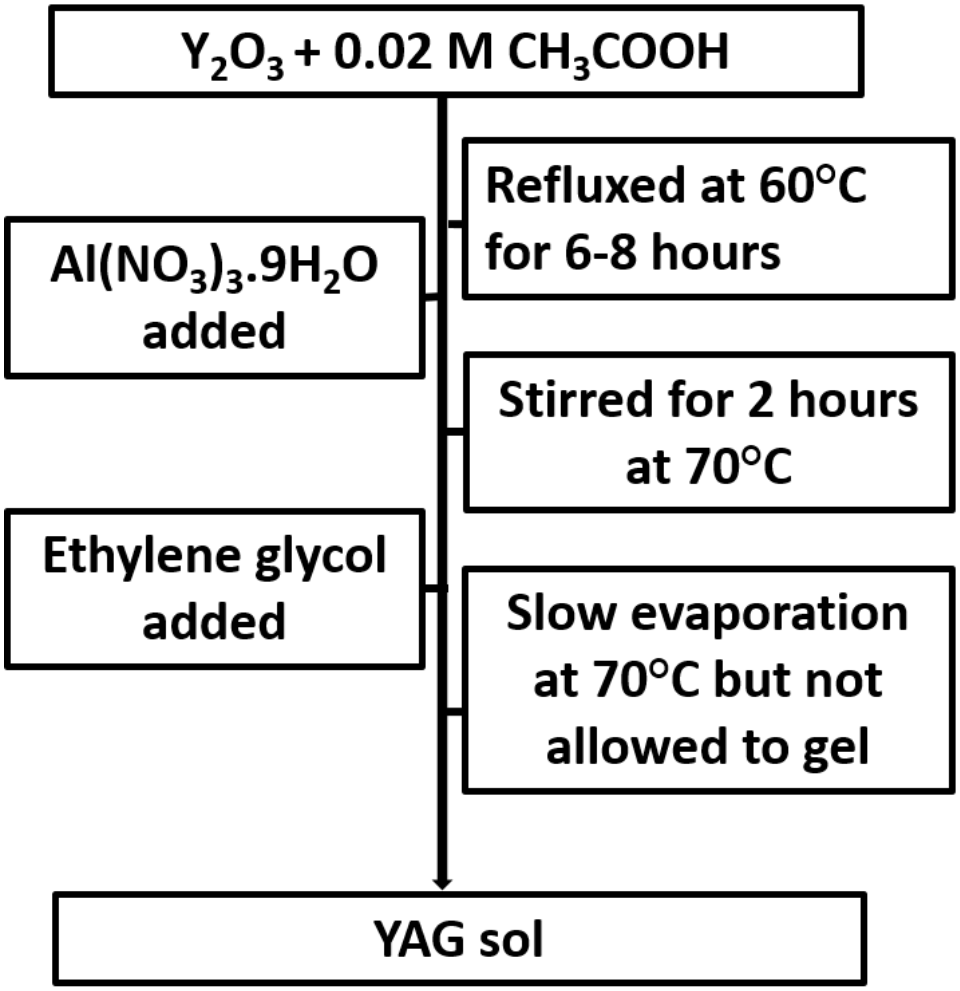

Figure 7.6: Flowchart describing preparation of YAG sol-gel

The YAG sol was applied to a SC YAG fiber, using a dip-coater illustrated in Fig. 7.3. Before dip-coating, the fiber was first cleaned with de-ionized water and then with isopropyl alcohol. The dip-coating was done at a withdrawal rate of 7.5 cm/min. The fiber was then left to dry in air for 10 hours. After this, it was put in an oven held at 130°C for 60 minutes to dry. After drying, the fiber was sintered in air at 1000°C for 14 hours to remove any remaining organic material from the sol-gel precursor. This entire process was repeated for each layer. Multiple dip-coating cycles were performed to increase the thickness of the sol-gel derived layer. To maintain a consistency between the layers, the same batch of sol-gel was used for all the dip-coating cycles and the withdrawal rate for the dip-coating process was kept the same. Figure 7.7 shows a micron-thick sol-derived YAG layer deposited on to a 330 μm YAG SC fiber. A side view of the same sol-gel YAG clad fiber is shown in Fig. 7.8. The image shows a consistent crack-free layer of YAG on the YAG SC fiber.

Despite the success in using the sol-gel method to obtain crack-free cladding layers, there were two major problems with this technique. Firstly, unlike reported in some studies [92], there were no significant improvements in the attenuation losses of the sol-gel clad fibers. Secondly, thickness of the sol-gel layers never exceeded more than a couple of microns. The thickness of the layer could be increased up to a certain limit by successive dip-coating cycles. But beyond this point, additional increase in layer thickness caused cracking of the cladding layer. The cracking could be attributed to the internal stress when the accumulating layers were too numerous. With increasing number of layers, possibility of imperfections due to thickness variation, inhomogeneous organic material removal, contamination, etc. also increased, thus raising the possibility of development of fissures. This severe limitation in cladding thickness has completely throttled the idea of the development of a double-clad fiber structure that is so essential for high power laser applications. This has led to the exploration of alternate technique to obtain a cladding layer for the SC fibers.

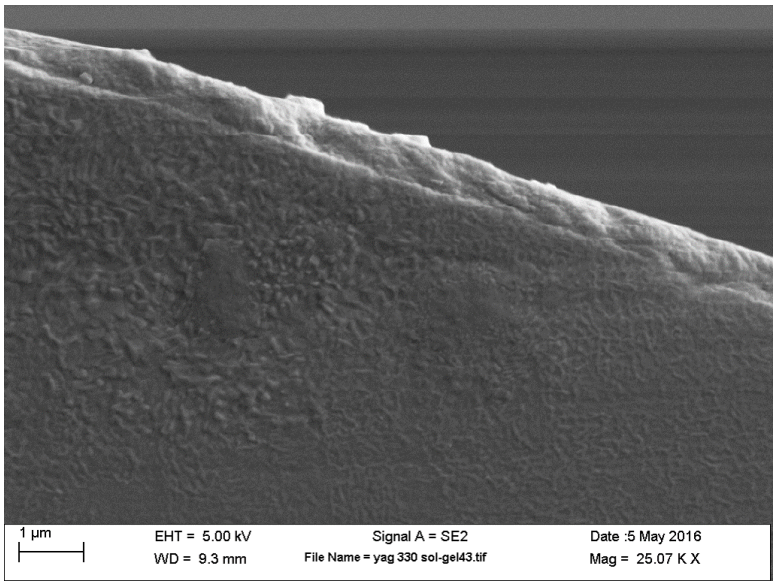

Figure 7.7: SEM image showing YAG sol-gel deposited layer on a 330 μm YAG SC fiber. The layer was obtained by 10 successive application of the dip-coating procedure.

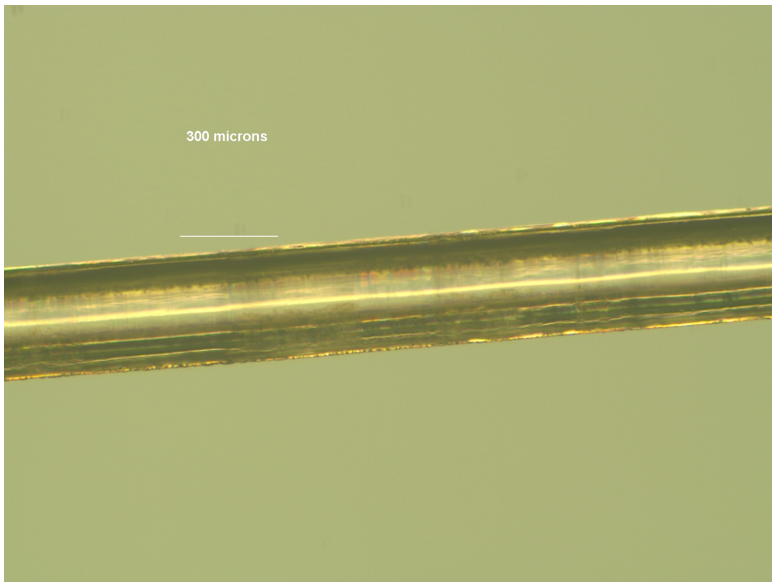

Figure 7.8: YAG sol-gel deposited layer on a 330 μm YAG SC fiber

7.3.2 Liquid Phase Deposition

Liquid phase deposition (LPD) is another low temperature approach in which a crystal can be deposited onto a substrate without the requirement of any special apparatus. It is a single step process where conformal layers with thickness of a few tens of microns can be deposited on substrates. Thickness of the deposited layer can be controlled by varying the reaction parameters like pH, temperature, etc. [93]. Germanium dioxide (GeO_2) or germania was selected as the material for cladding due its suitable optical and thermal properties. GeO_2 has a broad optical transmission window, transmitting from the NIR wavelengths to far out in the MIR wavelengths. It has a coefficient of thermal expansion close to that of YAG [94] and in its crystalline form, it has a high thermal conductivity.

Electronic grade GeO_2 was dissolved in a 1.4% ammonium hydroxide solution at 85°C with constant stirring. Substrate samples were introduced into this basic final solution where ammonium hydroxide was about 5% w/w. The pH value of the solution was slowly adjusted to 2 by adding dilute sulfuric acid to affect the precipitation of GeO_2. The samples were left undisturbed for 3-4 days and then taken out and dried in air and finally heated to 150°C to drive off the moisture. This entire procedure left a thick and uniform layer of crystalline GeO_2 on the substrates (see Fig. 7.9, Fig. 7.10, and Fig. 7.11).

While the liquid phase deposition allowed for the deposition of more than 10 microns, the quality of the deposited layer was very poor. The cladding was not strongly adherent to the surface of the crystal fiber and had a strong tendency to flake off. Bending of the fiber or contact with external surfaces aggravated the tendency to peel off. Moreover, the crystalline layer of germania had a significant surface roughness, thereby increasing the surface scattering of the fibers. Under such severe shortcomings, the idea to use liquid phase deposited germania as cladding for YAG SC fibers was abandoned.

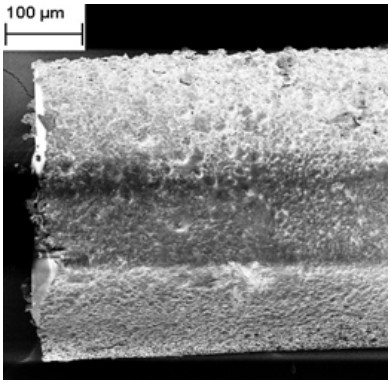

Figure 7.9: SEM image showing the growth of GeO_2 crystals on YAG SCF

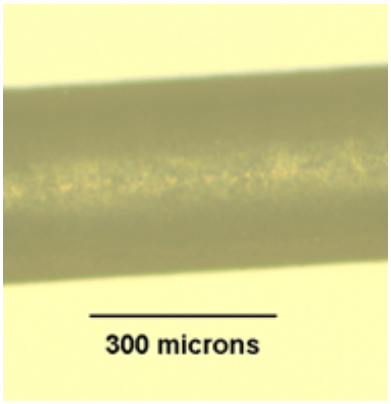

Figure 7.10: Optical microscope image showing the growth of GeO_2 crystals on YAG SCF

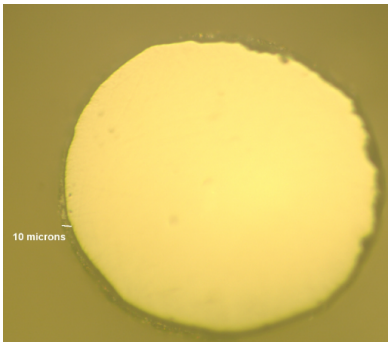

Figure 7.11: SEM image showing the growth of GeO_2 crystals on YAG SCF

7.3.3 Hydrothermal Growth

Some of the most promising methods for growing a crystal cladding on the SCFs are methods based on high temperature solvents. Methods such as liquid phase epitaxy (LPE) [95] and hydrothermal growth [96] can be used to grow high grade single crystals of different garnets. As a part of this project, hydrothermal growth was explored as a potential method to obtain a crystalline cladding for SC fibers.

Hydrothermal growth refers to the growth of crystals of different scale (nanocrystals to bulk single crystals) in the presence of aqueous solvents or mineralizers under high pressure and temperature. High temperature and pressure is required to dissolve and recrystallize materials which under normal conditions are mostly insoluble. The crystal growth is performed in specially designed steel pressure vessels called autoclaves. To affect the dissolution of the starting material at one end of the autoclave and crystal formation on the other, a temperature gradient is maintained in the autoclave. The dissolution takes place at the hotter region while the crystallization takes place in the colder part. The driving force for transport and growth is the thermal gradient in the autoclave. This creates a solubility differential between the hot lower zone and cooler upper zone. Supersaturation leads to deposition on the fiber seed. Compared to the sol-gel and LPD techniques discussed earlier, the hydrothermal process requires considerably elaborate and expensive growth apparatus and crystal growing expertise. Since no such facility was available at Rutgers University, for the present project, the hydrothermal growth of YAG crystalline cladding was performed at Clemson University by Professor Joseph Kolis.

A typical autoclave is shown in Fig. 7.12, where the crystal growth takes place in the upper section of the autoclave. This region is maintained at temperature lower than the bottom section.

The crystal growth was performed in a silver-lined autoclave, where the seed for the crystal growth was a YAG SC fiber grown by the LHPG technique. The seed was

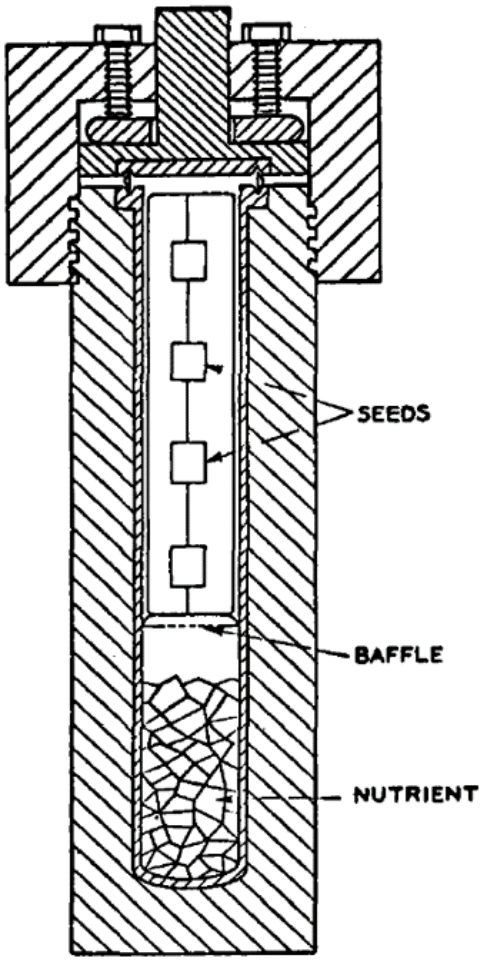

Figure 7.12: A typical autoclave used for hydrothermal growth of single crystals. Adapted from [97]. (Reprinted with permission)

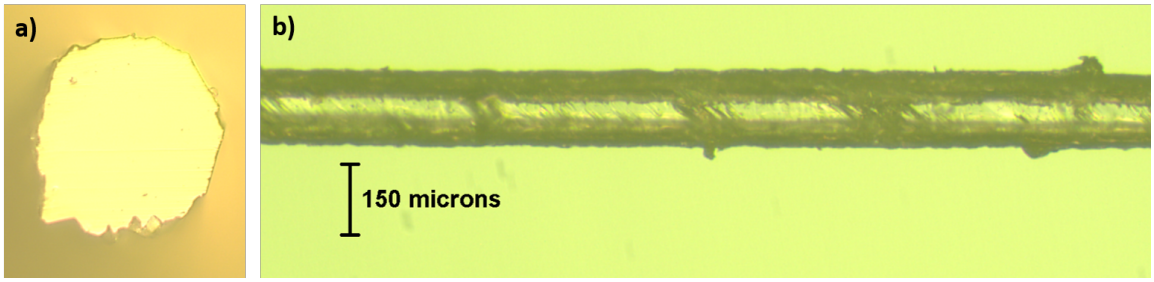

Figure 7.13: Hydrothermal layer of YAG grown on an undoped YAG SC fiber. a) Cross-section view b) Length view

suspended in the cooler upper region of the autoclave while the feed stock was kept at the warmer lower region of the autoclave. The feed stock comprised of a stoichiometric mixture of yttria and alumina. While this particular project did not involve the growth of doped crystals, dopants can be introduced by using desired ratio of oxide starting materials in the feedstock. 2 M K_2CO_3 solution was used as the mineralizer to affect the material transfer from the feedstock to the seed. The autoclave was maintained at about 550-600°C, with a gradient of only 3-5°C. Operating at such a temperature resulted in a pressure of 15-20 kpsi within the autoclaves. Under such conditions of growth, the crystal growth was allowed to continue for 15 days.

Using the hydrothermal growth technique, crystalline cladding layers of consistent thickness of up to a few hundred microns can be grown on the SC fibers. The growth of single crystalline cladding on the SC fiber was designed to take place in two steps. The first step involved the dissolving back of the curved SC fiber to reveal low-Miller index planes to provide sites for the nucleation of the cladding crystal layer. The second step involved the reversal of the thermal differential in the autoclave to initiate and continue growth of the cladding layer of undoped YAG.

Using the hydrothermal technique, crystalline YAG layers were grown on various samples using different growth conditions and periods. Figure 7.13 shows a 25 μm thick cladding layer was grown on a 120 μm diameter YAG SC fiber. The fiber was dissolved down to 100 μm diameter, before the growth of cladding layer was initiated. The cladding layer does demonstrate some spontaneous nucleation sites along its length. Such a spontaneous growth site can also be seen on the lower left section of the fiber cross-section.

While among the post-cladding techniques discussed previously the hydrothermal growth is superior than the others, this approach does have a couple of drawbacks. The length of the section of fiber that can be subject to such a growth is limited by the inner dimension of the autoclave. The facilities at Clemson, at present, are limited to

accommodating fibers of less than 5 centimeters. While the length can be increased by employing larger autoclaves, it would be really difficult to adapt the technique for handling fibers whose length are in the order of meters. A more serious drawback arises from the crystal quality of the cladding layer. The cladding layer grown by the hydrothermal method is usually highly strained. Such a strained crystal is likely due to the high curvature of the substrate surface. This strain made the fibers very fragile and drastically reduced their flexibility.

7.4 In-situ Cladding

The in-situ approach to cladding involves the growth of SC fibers where a refractive index profile is realized by the distribution of the ions across the fiber cross-section during the fiber growth. Under the effect of factors like diffusion, thermo-capillary currents, etc., dopant ions in a crystal distribute themselves radially in a manner that mimics graded index fibers. Such a technique, if achievable, would be highly desirable as it would lead to a monolithic core-clad structured crystal fiber. Post-cladding techniques, by virtue of their sequential growth approach often leads to fibers with a sharp discontinuity at the core-clad interface. This in turn, leads to increased scattering at the core-clad interface. However, using an in-situ approach, the possibility of such losses due to scattering at the core-clad interface can be effectively eliminated.

Two different approaches, one based on diffusion of dopants and the other based on auto-segregation of particular ions were explored.

7.4.1 Rod-in-tube Approach

The rod-in-tube (RiT) approach to cladding is very similar to the idea of growing a core-clad structured glass fiber from a RiT preform. While the viscosity of the melt in case of a glass fiber growth is very different from a crystal fiber growth, the premise of this approach is to transfer a cross-sectional profile from the preform to the fiber. The preform for the RiT crystal fiber growth would be a composite structure with the central rod of high dopant concentration and the outer tube of undoped material. Even though the low viscosity in the melt would tend to homogenize the composition of the fiber through diffusion, the expectation is that the fiber pull rate can be adjusted to overcome the diffusion equilibrium. Hence if the fiber is drawn fast enough, the high dopant concentration in the core region would not have sufficient

time to diffuse uniformly across the fiber cross-section and hence yield a fiber with graded profile of dopant. As the local refractive index of the crystal is affected by the dopant concentration, the graded profile of dopant concentration across a fiber cross-section would lead to a graded index fiber.

A typical RiT preform, as shown in Fig 7.14, consisted of an 450 μm diameter 50% erbium doped YAG SC rod placed inside 1100 μm diameter, pure SC YAG tubes with inner diameters of about 550 μm. The tube sections were bored from the undoped YAG crystal bars. The boring was performed by Mindrum Precision Inc. This process was limited to 1 cm lengths with source diameters about 1,000 μm, and requires the preform be drilled 5 mm on both sides, resulting in a variable mismatch between each hole and each tube sample. The preform was mounted in a V-groove aligned with the growth axis and fed into the molten zone of the LHPG apparatus by a mechanical belt drive from where it was grown into SC fibers.

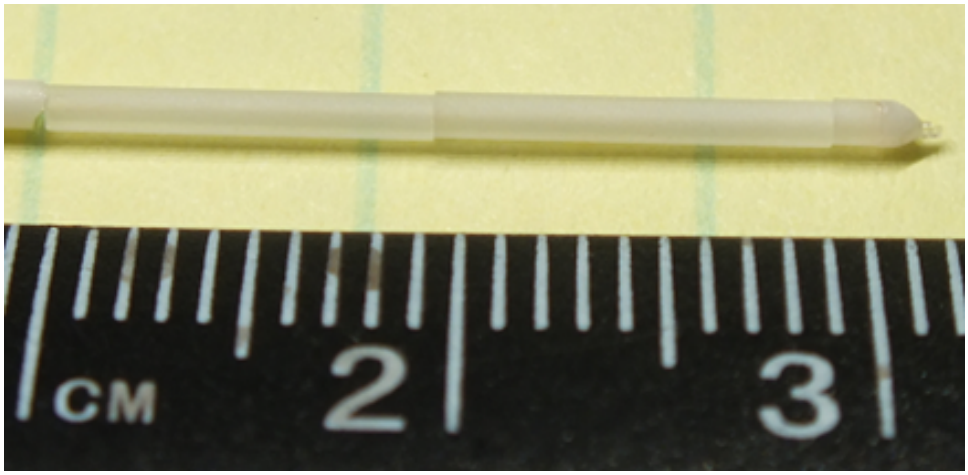

Figure 7.14: RiT preform consisting of YAG tubes assembled on a doped YAG SCF

During the fiber growth, the Er^{3+} ions had a very strong natural tendency to diffuse out to the outer undoped region. When temperature is held invariant, the extent of diffusion was determined by the time spent by the dopant ions in the molten zone. Fibers were grown at different speeds ranging from 1 mm/min to upto 6 mm/min. Samples grown at speeds below 3 mm/minute showed no strain-induced birefringence or cracking, whereas faster growths resulted in both. Optical quality of samples grown at speeds below 3 mm/minute was also high. When examined with polarized light in a Nikon Eclipse microscope, no evidence of any strain-induced birefringence or cracking was found for slow growth, whereas strain and defects were detected for samples grown at higher speeds.

Since the emission in RE ions is proportional to its concentration, laser-induced fluorescence of the Er^{3+} ions was measured to calculate the Er^{3+} ion distribution across the fiber cross section. An apparatus to characterize the Er^{3+} ion distribution was devised by Prof Stephen C. Rand at University of Michigan. A 532 nm laser source was used to excite fluorescence in the Er^{3+} ions. For the concentration mapping of the Er^{3+}:YAG SC fiber, a high resolution profile apparatus was set up to image laser induced fluorescence. Fluorescence from the fiber sample was relayed to a spatial filter using a 2f-2f lens system to reject incident laser light and magnified 10X before being passed through a sharp edge filter to discriminate further against scattered light at the laser wavelength. Finally, the image was captured with a CCD detector. Due to selective excitation of erbium ions by the incident laser, and the strict proportionality of re-emission intensity to excited state density, the brightness in fluorescence images provided a spatial map of the distribution of erbium ions that was linear in dopant concentration.

For the samples that were grown at speeds of 4 mm/min or higher, the crystal quality of the resultant fiber was poor, often exhibiting cracking at the center. The presence of such physical defects in the crystals introduced large anomalies in the flu-

orescence intensity and had to be omitted from further analysis. For the fiber samples grown at speeds of 1 mm/min, 2 mm/min, and 3 mm/min, the fluorescence intensity showed a similar pattern with the peak brightness of fluorescence intensity near the center of the fiber (see Fig. 7.15). The actual location of the peak was subject to random variation in the symmetry of the RiT preform. The shape of the fluorescence intensity distribution in the three samples showed significant differences. Unsurprisingly, the slower a fiber sample was grown, the flatter was its fluorescence intensity profile. This observation matched well with the modelling of the time-dependent thermal diffusion of the ions from the higher concentration at the center towards the periphery. Results for Er^{3+} ion distribution versus radius obtained with fluorescence imaging were well-described by a numerical model based on Fick's equation with a single value of diffusion constant. The inter-diffusion coefficient for Er^{3+} and Y^{3+} ions in YAG at a temperature of 2000°C was determined to be $(9.1 \pm 0.8) \times 10^{-11}$ m^2/s. These results demonstrate the fact that by changing conditions like fiber growth speeds and preform dopant concentration, it is possible to achieve fibers with dopant distribution that can be controlled to a certain degree.

Despite the demonstration of SC fibers with graded dopant concentration using the RiT method, there are significant challenges in growing actual graded index fibers using this technique. The degree of control that can be exercised over such a process is somewhat limited and the technique needs to be considerable refined to have a consistently reproducible ion distribution in the fibers. Moreover the actual refractive index profile due to the ion distribution has not been established yet and reliable technique to determine that needs to be developed.

7.4.2 Auto-segregation of dopants

It has been noticed previously that in certain doped systems, the fibers grown by LHPG technique exhibit non-uniform radial distribution of the dopant species. De-

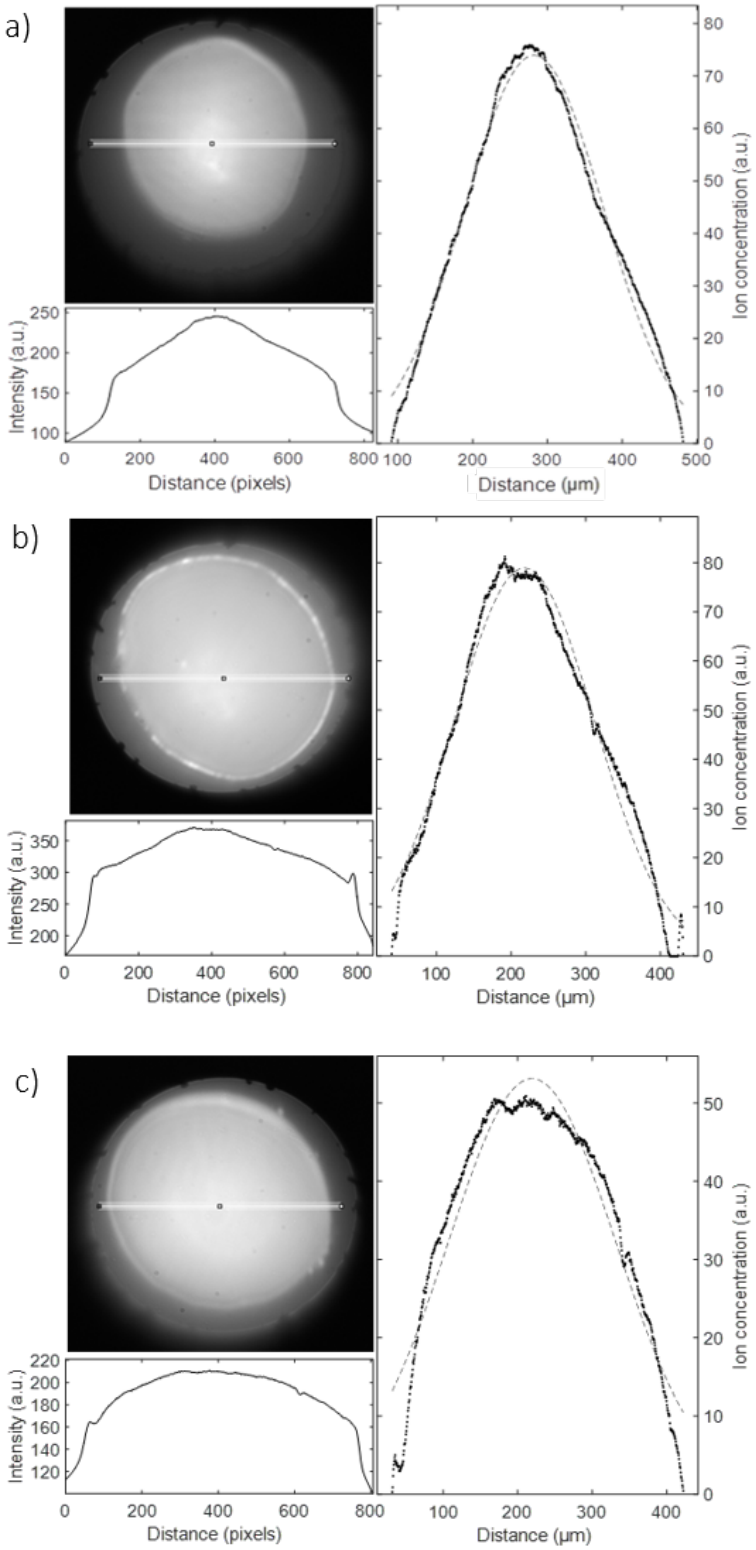

Figure 7.15: Er^{3+} distribution in 50% Er:YAG core with pure YAG cladding grown at (a) 3, (b) 2, and (c) 1 mm/min. The profiles are one-dimensional lineouts through fluorescent images giving dopant concentration versus position across each fiber sample.

pending on the dopant ions, there was a tendency of the dopant to either move to the center of the fiber or towards the periphery, creating a distribution profile. In Mg doped sapphire, for example, the center axis of the fiber showed a much higher concentration of Mg^{2+} ions compared to the fiber edges [98]. Such an effect has also been observed in doped YAG SC fibers as well. While Nd ions were observed to concentrate at the center axis [25] [92], Cr ions were observed to have higher concentration near the fiber periphery [99].

The movement of the ions in the YAG matrix seems to depend on their size and segregation coefficient [100]. Ions like Nd^{3+} and Ce^{3+}, which are larger in size compared to the Y^{3+} ions (see Table 7.2), have segregation coefficients less than one and tend to move towards the center of the fiber. On the other hand, ions like Cr^{3+}, which are smaller compared to Y^{3+} ions, have segregation coefficient greater than one and tend to move towards the outer rim of the fiber. Since the refractive index of YAG changes linearly with the addition of dopant ions (see Table 7.1), the auto-segregation of dopant ions in YAG can be explored as a means to create an effective refractive index gradient in the fiber, thereby creating a monolithic core-clad structured crystalline fiber.

RE Dopant	**Δn (x10^{-4}) per 1% of dopant**
Nd^{3+}	4.74
Ho^{3+}	2.44
Er^{3+}	2.10
Tm^{3+}	2.08
Yb^{3+}	1.60
Lu^{3+}	0.96

Table 7.1: Refractive Index change in YAG due to addition of different common RE dopants. [88]

Ion	Radius (Å)
Y^{3+}	1.02
La^{3+}	1.18
Ce^{3+}	1.14
Pr^{3+}	1.14
Nd^{3+}	1.12
Sm^{3+}	1.09
Eu^{3+}	1.07
Gd^{3+}	1.06
Tb^{3+}	1.04
Dy^{3+}	1.03
Ho^{3+}	1.02
Er^{3+}	1.00
Tm^{3+}	0.99
Yb^{3+}	0.98
Lu^{3+}	0.97

Table 7.2: Ionic radii of different trivalent rare-earth ions

The exact mechanism of the movement of the ions during fiber growth process has still not been decisively explained yet. In a previous study Liu *et al.* [98] have discussed a possible mechanism of the radial segregation of Mg dopant in sapphire SC fibers. They surmised that the cause of the ion movements was due thermo-capillary currents in the LHPG melt zone. The strength of these currents is determined by the magnitude of the Marangoni number. For most crystal growths using the LHPG technique, the magnitude of the Marangoni number of the melt is such that strong thermo-capillary currents are present. It is worth noting here that if the magnitude of the Marangoni is too high, oscillations in the melt are observed [101]. The thermo-capillary currents operate between fluid layers due a gradient in surface-tension. The differential absorption of the laser at different depths of the melt zone creates a gradient in temperature and hence in surface tension. Strong absorption of the laser radiation at the surface compared to the center of the melt creates a convection cell due the Marangoni currents, moving the larger ions to the center of the fiber. A possible explanation for the more pronounced effect of the current on the larger ions is likely due to the fact that the larger an ion is, the more cross-section it offers

for the current to act upon. Detailed discussion of the mechanism of the Marangoni currents is quite involved and was not studied under this particular project. However, a detailed study has been previously conducted by Chang *et al.* [99].

The movement of Nd^{3+} ions in YAG SC fiber were observed as a part of this project. Using the same apparatus described in the previous section, fluorescence measurements were carried out to identify the dopant distribution of Nd^{3+} ions across the cross-section of different Nd doped YAG SC fibers. The selective emission by the Nd^{3+} ions provided a map of the distribution of the dopants across a fiber cross-section.

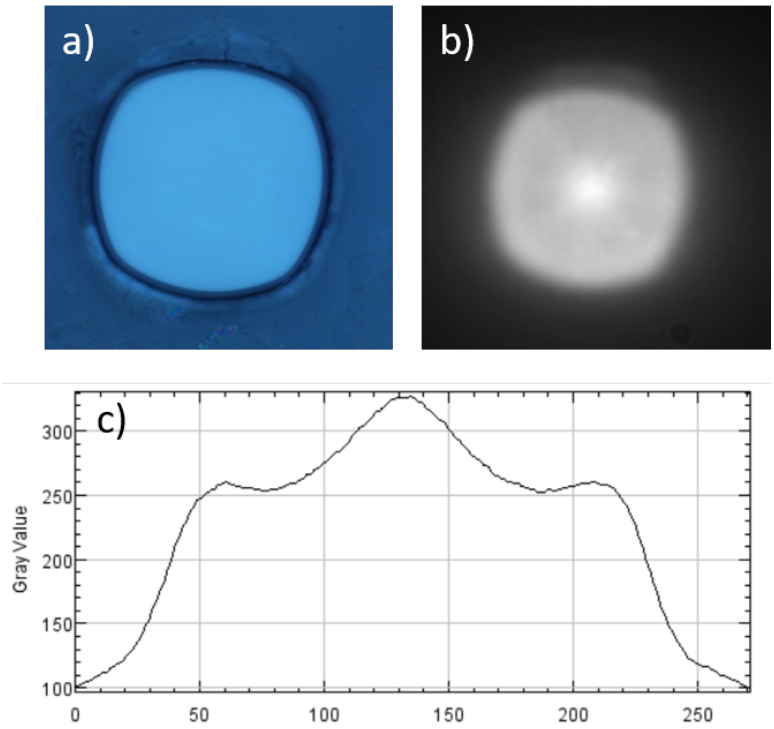

Figure 7.16: a) Polished cross-section of 120 μm 1.5% Nd:YAG SC fiber. b)Fluorescence image of same fiber. c) The profiles are one-dimensional lineouts of fluorescent image giving dopant concentration versus position across fiber sample.

Figure 7.16 shows the fluorescence measurement of radial distribution of Nd^{3+} ions in a 120 μm YAG SC fiber grown by the LHPG technique. The sample was obtained by two successive growths from a 1.5% Nd:YAG source bar. The measurement shows that the intensity of fluorescence of the Nd^{3+} ions is about 30% higher in

the central axis region of the fiber compared to the fiber periphery, indicating a decreasing concentration of the dopant with increasing distance from the radial center. Since refractive index of YAG increases monotonically with increasing concentration of Nd^{3+} ions, the radial distribution of the dopant would give rise to a graded-index along the fiber cross-section. Fluorescence measurements reveal that Nd:YAG fibers grown under different growth conditions show a similar distribution of dopants across the fiber cross-sections, suggesting that Nd^{3+} ions show consistent auto-segregation towards the fiber center in YAG SC fibers grown by the LHPG technique.

Chapter 8

Growth of sources with Varied Dopant Concentration

RE ions can substitute Y^{3+} ions in YAG to varying amounts. The degree of substitution depends on the size mismatch of the substituting ion with the Y^{3+} ion. Trivalent RE ions like ytterbium, holmium, erbium, and thulium, which are very similar in size to Y^{3+} ions, form stable aluminum garnet phases of their own [102]. These ions can form a crystalline solid solution with Y^{3+} ions in the garnet phase at any given ratio between the two pair of ions. In contrast, RE ions which have a considerable size difference with the Y^{3+} ions have limited solubility in YAG and have no known RE aluminum garnet phase. For example, trivalent neodymium, which is about 12% larger than Y^{3+} ion, has a maximum solubility of 18% in the YAG phase [103]. The output characteristics of a RE doped laser depends heavily on the concentration of the dopant in the lasing medium. For a doped fiber of a given length, there is an optimal concentration of dopant that produces maximum laser output. If the concentration is lower than this optimal value, the pump power will not be effectively absorbed by the lasing ions. If it is greater than the optimal value, the emitted laser wavelength will be reabsorbed.

Varying amounts of dopants can be introduced into a glass system with relative ease using solution doping. This is due to the open amorphous nature of glasses which allow such processes to be handled at relatively lower temperatures. At these temperatures, however, YAG does not allow significant diffusion and substitution. Hence, the concentration of dopants required in a crystal fiber cannot be easily modified, and is limited to the starting material. Since SC fibers are usually grown from crystalline starting materials, trying to vary the dopant concentration would require obtaining the source material from crystalline sources which had originally been grown with the required dopant concentration. Such a process is not only time consuming but rather expensive as well. A possible solution is to use a ceramic source material, made in-house [92]. However, it has been observed that the purity of the starting material has a direct influence on the optical properties of the fiber [104]. Hence, a hybrid process is desirable which allows for the variation of the dopant concentration without affecting the quality of the fiber.

A new method to grow high purity SC YAG fibers with varied RE dopant concentrations using a low cost, low temperature sol-gel based method was developed. A sol-gel derived layer of holmium aluminum garnet ($Ho_3Al_5O_{12}$, HoAG) was deposited on a 330 μm diameter pure YAG SC fiber by dip-coating. This fiber was then regrown to SC fibers with diameters of about 120 μm, using the LHPG technique to introduce the Ho^{3+} ions into the YAG matrix. The dopant concentration of the Ho^{3+} ions in these fibers was changed by varying the thickness of the sol-gel derived layer. Although the present technique was developed to introduce Ho^{3+} ions into YAG, this method can be adapted for other ions like Er^{3+}, Tm^{3+}, Yb^{3+}, etc. This method offered the advantage of low cost, and flexibility of changing dopant concentration without sacrificing optical quality. By having the freedom to introduce dopants during growth, not only can the dopant concentration be modified according to need, but other sensitizing ions can be introduced to change lasing characteristics of the gain

medium. This method also makes it possible for the different sections of the same SC fiber to be doped with different dopant ions that can act as a saturable absorber or magneto-optic component, hence paving the way for a monolithic all-crystalline fiber laser system.

8.1 Sol-gel dip coating

Sol-gel based synthesis of RE aluminum garnets has been previously studied by using an acetate-glycolate pathway by Dubnikova *et al.* [102] In this study, we use a similar method to obtain polycrystalline HoAG (see Fig. 8.1 for flowchart). HoAG was derived by the hydrolysis and condensation of holmium oxide and aluminum nitrate. The materials used for the synthesis were Ho_2O_3 (Alfa Aeser, 99.995%), $Al(NO_3)_3.9H_2O$ (Acros Organics, 99+%), glacial CH_3COOH (Fisher Scientific) and ethane-1,2-diol ($(-CH_2OH)_2$) (Acros Organics). Holmium oxide is refluxed in 0.02 M acetic acid at 60-70°C for 6-8 hours to obtain holmium acetate. Aluminum nitrate was added to the solution and the solution was constantly stirred at 70°C for 2-3 hours. Finally, ethyl glycolate is added and the final solution is kept at the same temperature, slowly evaporating the dissolved water to raise the viscosity of the precursor sol. The viscosity is allowed to increase considerably, while not reaching gelation. The subsequent sol was used for dip coating.

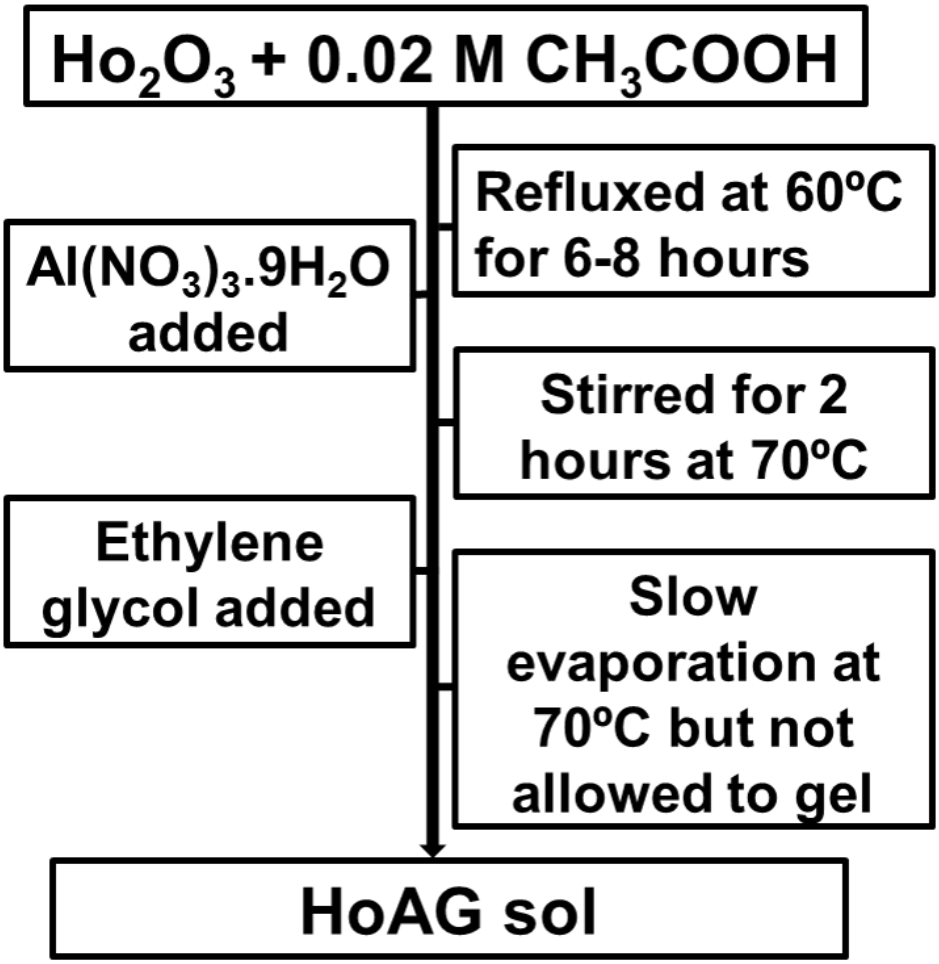

Figure 8.1: Flowchart describing preparation of HoAG sol-gel

The HoAG sol was applied to a SC YAG fiber with a diameter of 335 μm, using a dip-coater illustrated in Fig. 7.3. Before dip-coating, the fiber was first cleaned with de-ionized water and then with isopropyl alcohol. The dip-coating was done at a withdrawal rate of 7.5 cm/min. The fiber was then left to dry in air for 10 hours. After this, it was put in an oven held at 130°C for 60 minutes to dry. After drying, the fiber was sintered in air at 1000°C for 14 hours to remove any remaining organic material from the sol-gel precursor. This entire process was repeated for each layer. Multiple dip-coating cycles were performed to increase the thickness of the sol-gel derived layer. To maintain a consistency between the layers, the same batch of sol-gel was used for all the dip-coating cycles and the withdrawal rate for the dip-coating process was kept the same. One, two, three and four cycles of dip-coating were applied on four different but contiguous sections of the YAG fiber, with each section covering roughly 1 cm. The increase in thickness of the sol-gel layer due to each cycle of dip-coating was approximately 0.25 μm.

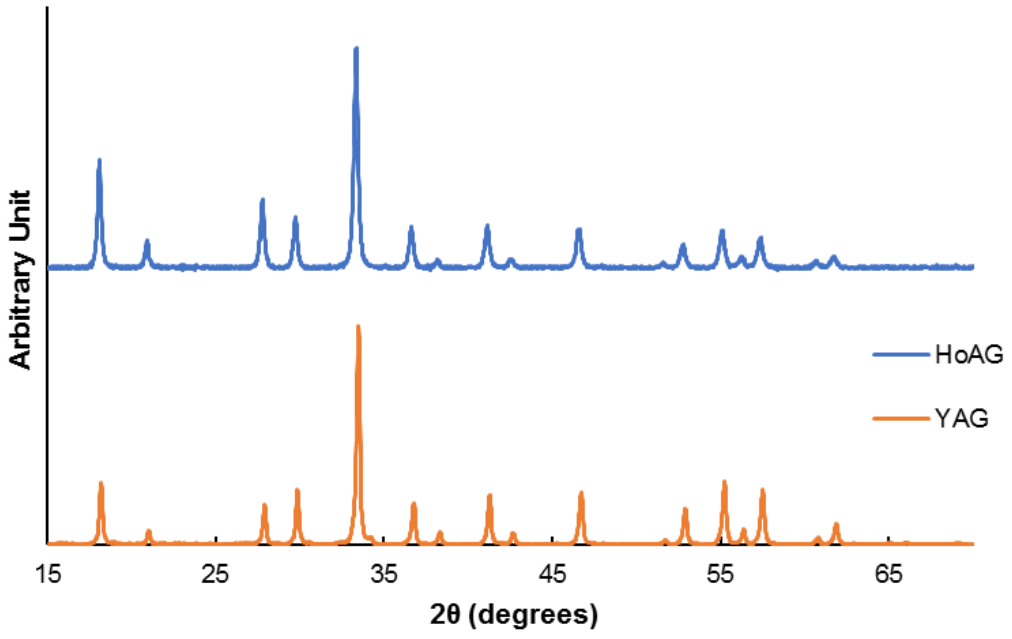

Figure 8.2: XRD pattern of sol-gel derived HoAG (top) compared to YAG (bottom)

For the homogeneous distribution of Ho^{3+} ions into the YAG matrix, it is required that the HoAG form a true solid solution with the YAG. One of the important requirements of two materials forming a solid solution is that they have the same crystal structure. X-ray diffraction results confirm that the HoAG obtained from the sol-gel method was indeed in the garnet phase. The sol-gel precursor solution yielded a yellowish-white porous solid. This solid was then ground up and then held at 500°C for one hour to burn off the organic material. Finally, it was sintered at 1000°C for 10 hours to obtain a pinkish white powder. Figure 8.2 compares the XRD pattern obtained from the sol-gel derived HoAG with YAG. It can be seen that all the characteristic peaks associated with the garnet structure are present in the sol-gel derived HoAG, confirming its garnet structure. Hence we can expect HoAG to form a single phase solid solution with YAG.

8.2 Fiber Growth

After having the desired thickness of the sol-gel derived layer of HoAG on a pure YAG fibers, it was regrown to smaller diameter SC fibers using the LHPG technique. The HoAG coated 330 μm diameter YAG fiber was regrown into Ho:YAG SC fibers of 120 μm in diameter. The entire YAG fiber preform with sections of 1, 2, 3, and 4 layers of HoAG coating was grown, at a speed of 1.5 mm/min, in a single fiber growing run to maintain a consistency among the different sections. Each section yielded about 14 cm of 120 μm diameter fiber. Pieces measuring about 10-12 cm corresponding to each preform section were identified and removed.

Once the fibers were grown using the LHPG technique, the crystallinity of the SC fibers were measured using X-ray rocking curve analysis. The analysis showed that the fibers are of a very high quality single crystalline phase with no indication of twining or amorphous phases.

8.3 Holmium Concentration

The amount of holmium in each fiber section, was characterized by both optical and quantitative x-ray techniques. The concentration of Ho^{3+} ions was determined by optical measurements as shown in Fig 8.3. Ho:YAG absorbs at 532 nm. The power absorbed increases with the increase of concentration of Ho^{3+} ions in YAG. Attenuation losses for SC Ho:YAG fibers were measured for known Ho dopant concentrations (0.5, 1, 4%) and a general trend was established. By performing optical absorption measurements on the fiber sections grown from the preform with different numbers of HoAG layers and comparing it with the pre-established trend, an estimate of the unknown atomic percent of Ho in the different fiber sections can be obtained. Experimental measurements demonstrate that for every layer of HoAG on the 330 μm diameter source preform increases the Ho concentration of the regrown 120 μm diameter fiber by 0.21%. Hence for example, the section grown from the preform having 2 layers of HoAG is expected to have 0.42% Ho:YAG. It is to be noted here that the SC fiber grown from the section of the preform having 1 layer of sol-gel derived HoAG has been removed. This segment had a significant "hotspot" in the fiber which rendered its optical quality significantly poorer than the other fiber sections.

The Ho concentration determined by optical absorption methods assumed uniform waveguide quality for all sections of the fiber. Although, this is a reasonable assumption, the estimation of Ho concentration obtained by the optical method could be affected by fiber quality. Hence, for further verification, the concentration of Ho was also determined by EPMA. The Ho concentration in the different fiber sections grown from the preform having different number of layers of HoAG is shown in Fig. 8.4. As can be seen from the figure, each layer of sol-gel derived HoAG increases the Ho dopant concentration in the final fiber by approximately 0.2%. This is in very good agreement with the optical data discussed in the previous section.

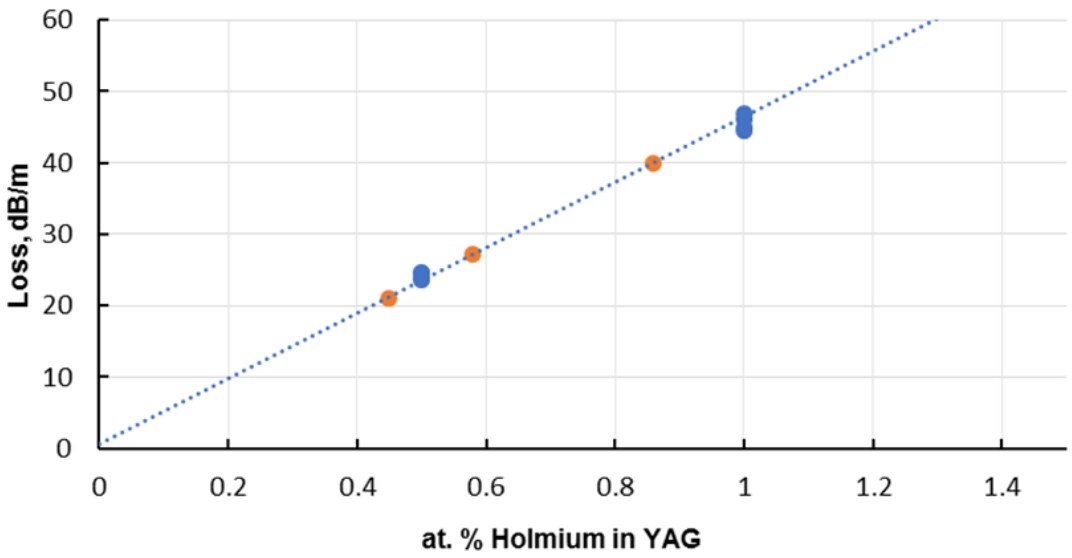

Figure 8.3: Estimating concentration of Ho dopant in YAG SC fiber in sol-gel coated regrown fibers, by fitting it to previously obtained absorption loss for a known concentration of holmium, shown as blue dots. The data points in orange are losses measured for SC fibers grown from preforms with 2, 3, and 4 layers of sol-gel HoAG.

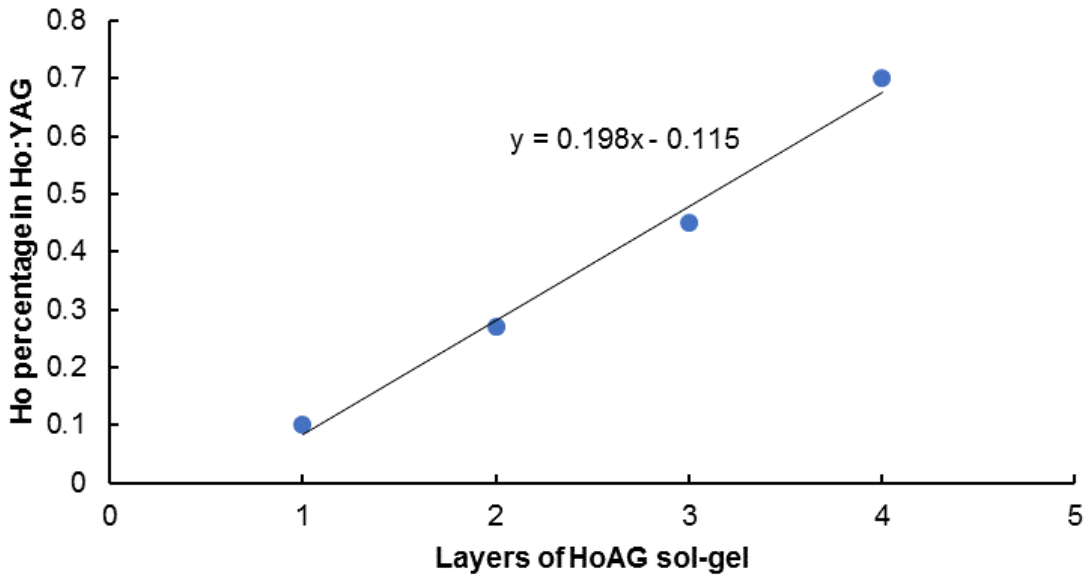

Figure 8.4: Change in holmium concentration with number of layers, as measured by EPMA

Chapter 9

Ho:YAG Single Crystal Fiber Laser

The laser emissions of Ho^{3+} ion at 2 μm and 2.9 μm arising from the transitions between the Stark levels of the $^5I_7$ and $^5I_6$ states, respectively to the $^5I_8$ ground state have been well studied (see Fig. 9.1) [105] [106]. In particular the 2 μm transition has received a lot of research attention due its potential as an eye-safe source for applications like target illuminators, Doppler lidars, medical devices, etc. The 2 μm micron transition is especially appealing for various applications due to the long lifetime of the upper $^5I_7$ level. Such a long upper level lifetime allows the storage of a large amount of energy in the upper level, favoring operation in a Q-switched mode.

Lasing characteristics Ho^{3+} ions in crystalline materials have been well documented, with the earliest report of lasing behavior reported in 1965 by Johnson *et al.* [107]. Despite such early beginnings, very little research effort has been invested in towards the investigation of lasing characteristics in materials other than bulk crystals. It is only in the last few years that alternate configurations like Ho^{3+} doped SC fibers or thin disks have been properly investigated. The SC fiber architecture offers the potential for the development of a high power eye-safe laser system that is capable producing high power output in both cw and pulsed mode of operation.

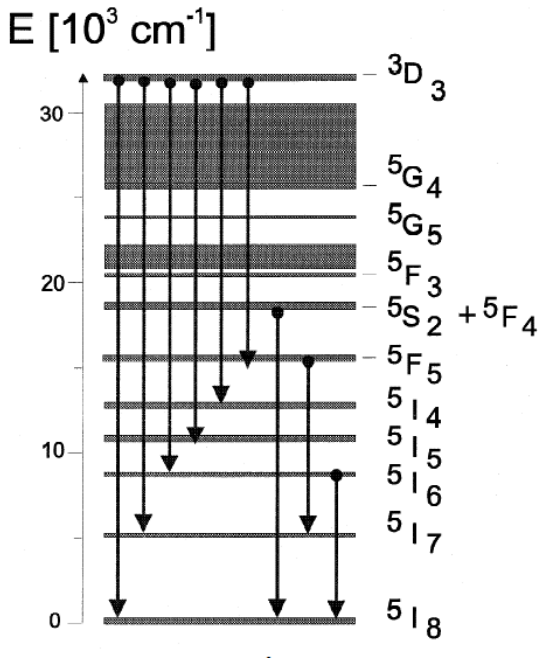

Figure 9.1: Energy level scheme of Ho^{3+} ion, observed emission transitions found are indicated by arrows. (Reprinted with permission) [105]

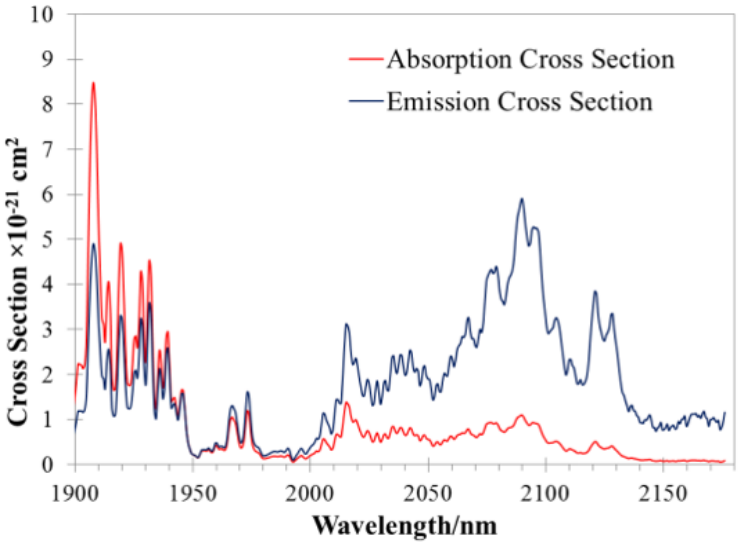

Figure 9.2: The spectra of Ho^{3+} in YAG obtained using a Yokogawa AQ6375 Optical Spectrum Analyzer (OSA). Results obtained at Clemson University.

While Ho^{3+} ions have a rich lasing spectra in the near infrared region (see Fig 9.2), experiments were limited to the 2 μm lasing between the $^5I_7$ and $^5I_6$ states. The spectrum shows a peak absorption at 1908 nm. Pumping at this wavelength resulted in lasing around 2 μm, Accordingly, the lasing experiments in this project were conducted using pumping at 1908 nm.

The lasing experiments were performed at Clemson University by Professor Eric Johnson's group. The schematic of the lasing set-up is shown in Fig. 9.3. The Ho doped SC YAG fiber was pumped using a TEM_{00} 1908 nm Tm:fiber laser (IPG TLR-50) in either continuous-wave (CW) or pulsed mode. For the lasing experiments, a modulated pump laser (10 Hz, 50% duty cycle) was used to reduce thermal load. The pump was coupled into the SC fiber using a 200 mm focal length lens (F1). The output and input ends of the fiber used for the experiment were polished but not coated. The optical cavity was set-up using a high reflector (HR) at the input end and just the bare polished fiber end at the output end. The HR allowed high transmission at the pump wavelength and high reflectivity between 2050 and 2400 nm, where the Ho^{3+} ions were expected to lase. The HR was butt-coupled to the SC fiber. At the output end, the 8% Fresnel reflection from the uncoated fiber face was sufficient to provide a reasonable balance between multiple passes of the pump wavelength and extraction of the laser wavelength. The laser output from the fiber was collimated using a 5.95 mm focal length lens (F2). A dichroic mirror (M1), at 45° angle of incidence, was used to separate the residual pump and laser wavelengths. Similar to the HR, M1 had high transmission at pump wavelength and high reflectivity at 2090 nm. During the experiemnts, the fiber was passively cooled.

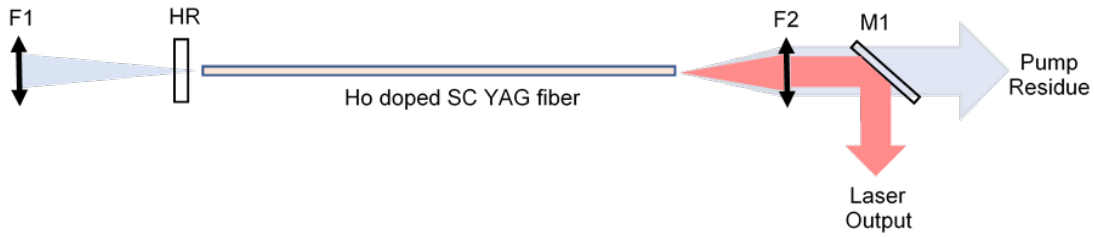

Figure 9.3: Schematic of Ho:YAG lasing set-up

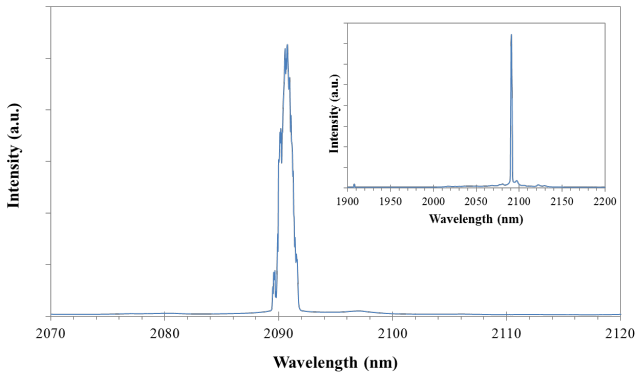

Figure 9.4: The optical spectrum of the laser at 20 W of output power centered at 2090.6 nm. The inset, the whole spectrum from 1900 to 2200 nm

9.1 Results for 330 μm SC fibers

Using the lasing set-up described above, different 0.5% Ho:YAG SC fibers of 330 microns were studied. There was a strong correlation between fiber quality and slope efficiency of the laser output. Fibers which had higher attenuation losses demonstrated low slope efficiency. One such high loss (9 dB/m) fiber (330 μm diameter, 10.1 cm length) had a slope efficiency of just 10.2%. However, the slope efficiency increased significantly when the lasing experiments were conducted on low-loss fibers. The highest optical-to-optical slope efficiency of 72.3% was achieved in an 11 cm fiber with an attenuation loss of 0.6 dB/m at 1064 nm. Another sample, an 11.5 cm long fiber with a 0.9 dB/m loss showed a 67.5% when pumped under the same condition. For this fiber, the spectrum of the output laser beam at the output power of 22 W is shown in Fig. 9.4 on a linear scale. The laser wavelength is centered at 2090.6 nm

with a full width at half maximum (FWHM) of 1.3 nm. The inset in Fig. 9.4 shows the relative strength of the signal laser beam relative to the pump beam after passing through the second dichroic filter.

Despite the high slope efficiency of the low-loss fibers, the mode of the laser output was highly multimode. Factors like large fiber diameter, absence of a fiber cladding and the presence of diameter variations along the fiber length result in output beam being speckled and highly multimode (see Fig. 9.6 and Fig. 9.7). It was noticed that the beam quality varied significantly as the output power increased, with the output beam becoming more diverging and more multimode as the power output increased.

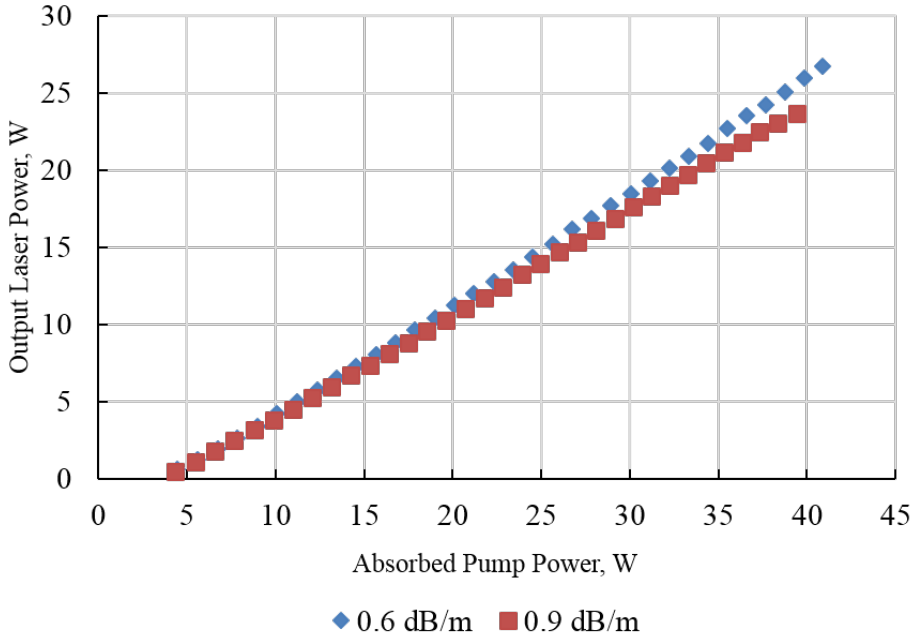

Figure 9.5: Slope efficiency of two 0.5% low-loss Ho:YAG SC fibers. The fiber with 0.9 dB/m loss shows a slope efficiency of 67.5% while the fiber with 0.6 dB/m loss shows a slope efficiency of 72.3%

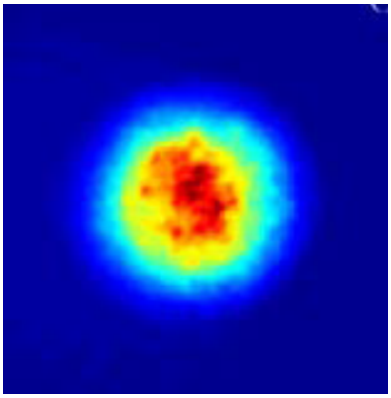

Figure 9.6: Mode profile of output 0.9 dB/m loss Ho:YAG fiber in the near field

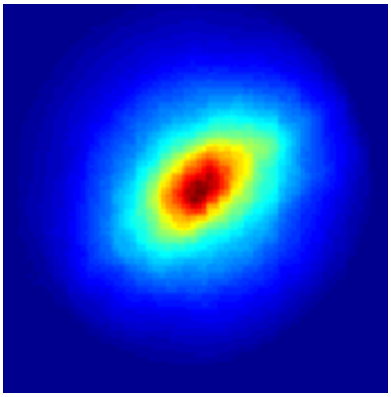

Figure 9.7: Mode profile of output 0.9 dB/m loss Ho:YAG fiber in the near field

9.2 Results for 120 μm SC fibers

The lasing characteristics of holmium doped YAG SC fibers grown from HoAG sol-gel coated YAG fibers were also studied using the lasing set-up described previously. Similar to previous experiments, when pumped with a 1908 nm Tm:fiber laser, Ho doped YAG SC fibers demonstrated lasing at 2.09 μm. The lengths of the fibers grown from the preforms with 2, 3 and 4 layers of HoAG were 11 cm, 12 cm and 11 cm, respectively. The performance of the three different fibers are shown in Fig. 9.8. It could be seen that the slope efficiency increased with the increase in holmium concentration of the fiber. For the fibers grown from performs having 2 and 3 layers of HoAG, the residual pump was too high suggesting that, at these fiber lengths, the Ho^{3+} ion concentration was too low for effective absorption at the pump wavelength. The slope efficiency did not show any thermally induced roll-off up to 27 W of pulsed input power. This result demonstrates the good passive cooling due to increased surface-to-volume ratio for the small diameter fibers.

For the fiber grown from the preform with 4 layers of HoAG, the lasing characteristics were measured for three different fiber lengths. It can be seen from Fig. 9.9, that the slope efficiency is optimized for the 10.7 cm length.

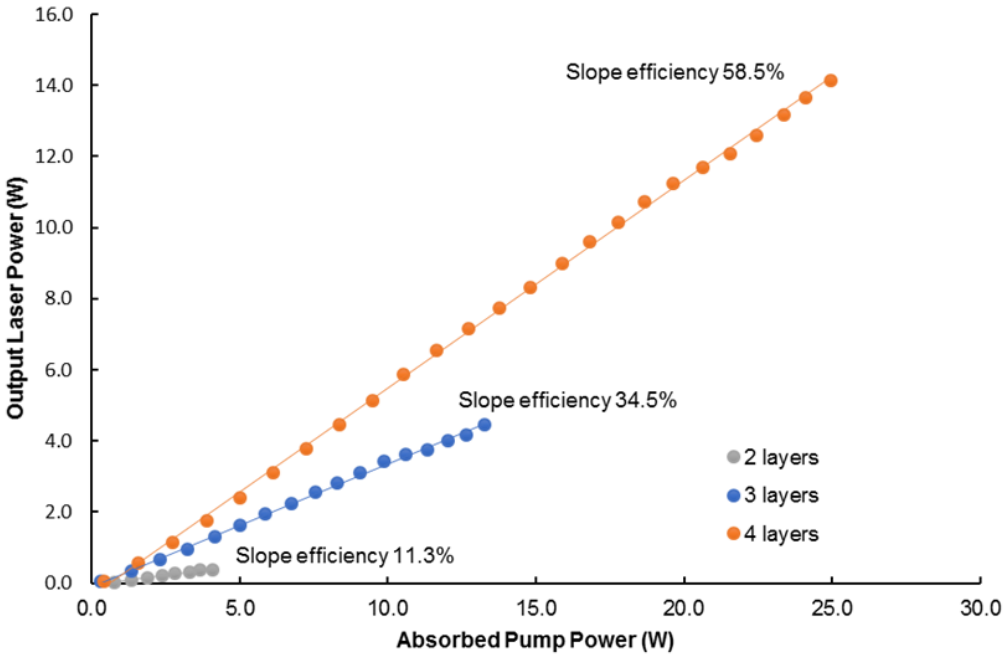

Figure 9.8: Slope efficiency of Ho:YAG fibers grown from a preform with different number of HoAG layers

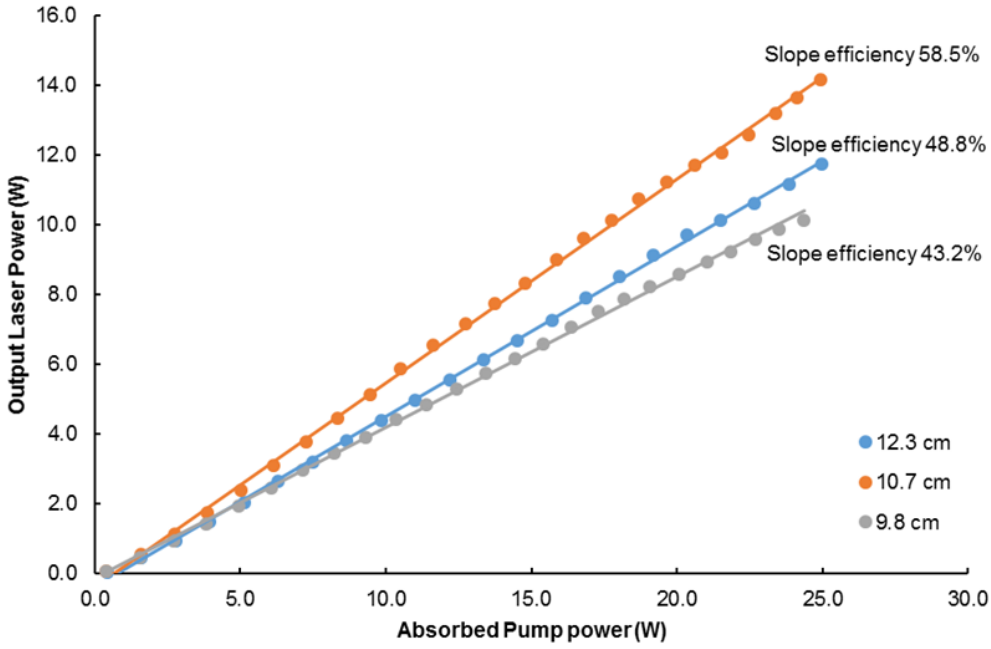

Figure 9.9: Slope efficiency of Ho:YAG fiber at different lengths of fiber grown from 4 layer HoAG coated preform

The maximum slope efficiency observed for these SC Ho:YAG fibers was 58.5%, which was lower than the 72.3% slope efficiency reported for 330 μm diameter 0.5% Ho:YAG fibers. A possible explanation for the lower slope efficiency could be due to increased scattering losses. The number of bounces of light while being wave guided through a smaller diameter fiber is more than that of a larger diameter. Since the SC fibers were not clad, an increased number of bounces increase the scattering losses in the fibers.

It was also noticed that compared to the 330 μm diameter 0.5% Ho:YAG fibers, the threshold for lasing for the 120 μm diameter Ho:YAG SCF fibers was lower. While the threshold for lasing for the 330 μm diameter fibers was about 3 W, the 120 μm diameter fibers showed a lasing threshold of a few hundred milliwatts. The decrease of the lasing threshold in the smaller diameter fibers was likely due to the tighter optical confinement possible in these fibers.

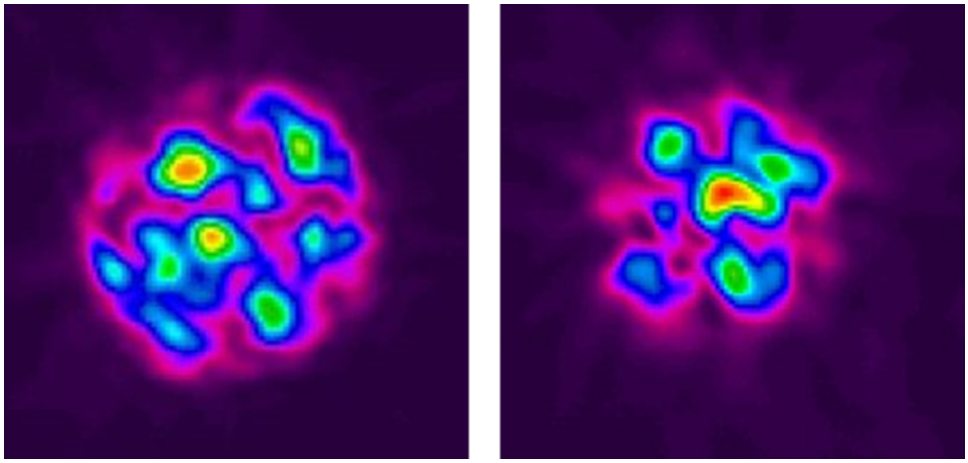

Figure 9.10: Mode profile of output in the near field (left) and far field (right). Beam profile captured using Ophir SP503U silicon CCD camera.

The near and far-field beam profiles of the laser emissions show that the output was highly multi-mode (see Fig. 9.10). This resulted from the size and quality of the SC fiber used as the gain medium. The Ho doped SC fiber has a 2% variation in fiber diameter, which is small yet a significant variation. Since the fiber had no

cladding, the scattering from the fiber surface caused a large degree of mode-mixing. The cross-section of the SC fibers was about 120 μm across, which is much bigger than the dimension required for single mode operation at the lasing wavelength. Moreover, there are no spatial mode control for the cavity to clean up the propagating modes. All these resulted in a highly multimode lasing output.

Chapter 10

Crystal Quality and Crystallographic Data

10.1 Crystal Orientation

Crystal growth has a natural inclination to form facets as the anisotropic surface free energy has a tendency to define an equilibrium shape corresponding to the minimum value of surface energy. Facets are the macroscopic manifestation of the crystalline structure of a material. Faceting will occur when the surface energy can be reduced by exposing surfaces of low index, thereby giving a clear macroscopic indication of the underlying crystallographic structure of the solid. Although facets are not defects, in a majority of applications, highly faceted crystals are undesirable. This is due to the fact that faceting introduces chemical inhomogeneities and lattice strain [108]. While RE doped garnets grown from melts have a natural tendency to form facets, the formation can be suppressed to a certain degree by optimizing growth conditions. Factors like seed orientation and direction of growth, curvature of the solid-liquid interface, temperature gradient in solid and undercooling temperature at growth interface determine the lateral extension of the facet [109]. Faceting was a common

feature amongst the YAG SC fibers grown as a part of this project (see Fig. 10.1). It is worth mentioning here that for crystal pulling techniques, faceting is not similar to periodic diameter variations which arise due to fluctuation in melt shape and volume, fiber pulling rates, etc. The scale of variation in the two cases are starkly different with faceting giving rise to surface roughness in the order of nanometers whereas diameter variations are of the order of micrometers.

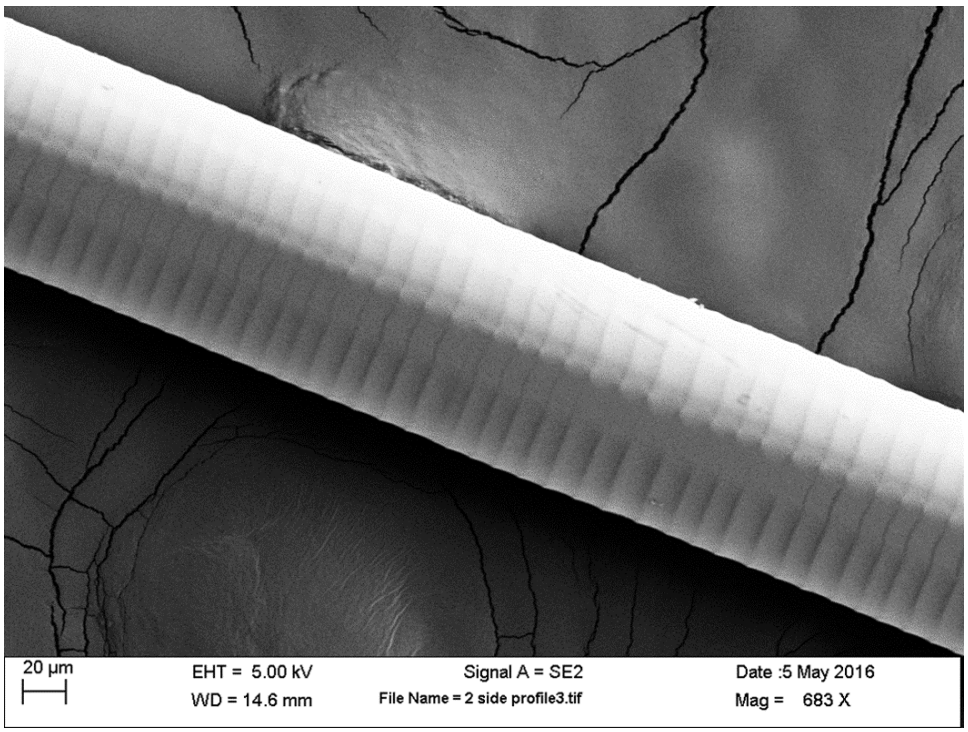

Figure 10.1: SEM image of 120 μm YAG SC fiber showing faceting.

In this project a series of experiments were conducted to study the effect of oriented seeds on faceting and transmission losses in the fiber. In an earlier work, Ishibashi *et al.* [29] had determined that facet-free crystal growth was possible for YAG if the seed with an orientation of 15° from [100] to [110] direction was used. However, in the present project it was determined that using such a seed was neither necessary nor sufficient for growing facet-free SC fibers. Even with this oriented seed, occasional faceting was observed in some fibers while, facet-free fibers were growing using randomly oriented seed with visible faceting (see Fig. 10.2). Experiments

also determined that faceting did not influence the transmission losses in a fiber. A likely explanation of this could be due to the fact that surface roughness arising from faceting was much smaller compared to the wavelength of light propagating through the fiber.

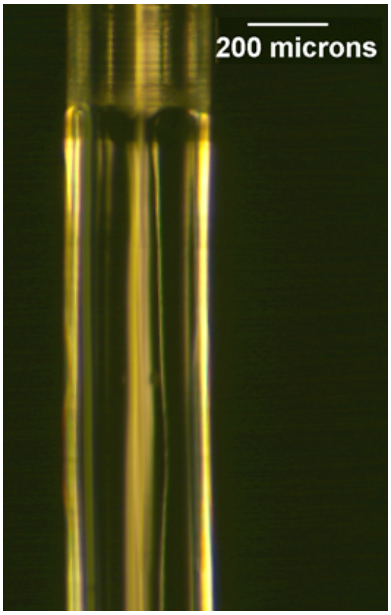

Figure 10.2: Fiber with no faceting grown from seed which displays faceting

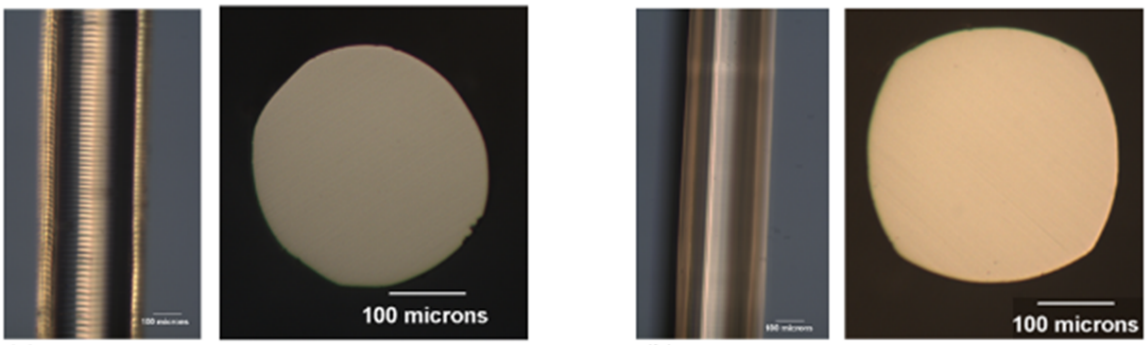

Figure 10.3: Left: Fiber grown from randomly oriented seed; Right: Fiber grown from oriented seed with [100] growth direction

In spite of not observing any noticeable improvements in transmission using oriented seeds, their use was still continued for two different reasons, both of which are concerned with a degree of standardization of the crystal growth process. Such seeds had a peculiar cross-section, which resembled a square with convex sides (see

Fig. 10.3). If an end face of a grown fiber did not resemble such a shape, it can be claimed that the growth direction had wandered off from the orientation of the seed to a different orientation. The standardization of the growth process also allowed the easier mathematical analysis for higher order modes generated in such fibers.

Crystal orientation for certain fibers have been determined using a Bruker SMART APEX diffractometer. It was observed that in fibers where the ends resemble the cross-section described previously, the growth orientation was maintained throughout the length of the fiber. Either ends of the crystal fiber were analyzed, and instead of the expected crystal orientation of 15° from the [100] to the [110] direction, both fiber ends had a growth direction of [100].

10.2 Single-crystallinity

Single crystalline hosts are considered to be better laser host materials than ceramic materials due to the absence of grain boundaries. Not only can grain boundaries act as centers for scattering and increase transmission losses, dopant ions have a tendency to concentrate around grain boundaries, giving rise to localized centers of uniform doping in the material. Since having a single crystalline host was a central premise to the project, experiments were conducted to verify the crystallinity of the grown fibers. Crystallinity was determined using X-ray rocking curve measurements. The rocking curve, obtained by using a nearly parallel source, shows excellent crystallinity with no indication of twining or amorphous phase inclusion. The single-crystal rocking curves for certain reflections were obtained by use of a Bruker Vantec-500 area detector and a Bruker FR571 rotating-anode x-ray generator operating at 40 kV and 50 mA and equipped with a 3-circle Azlan goniometer.

In the rocking curve collected from the Er:YAG rod-in-tube sample, shown in Fig. 10.4, the shaded area represent the signal due to the source. The two peaks are

due to the source. In more advanced systems, the higher angle peak is removed by use of a sophisticated monochromator. It can be observed that the FWHM of the measured signal peak was principally due to the dispersion of the source used in the measurement. This meant that the crystal quality is so good that it does not affect the measured signal. If the sample was a poorer quality single crystal, the FWHM would have been higher than the obtained value of 0.052. The presence of twins or amorphous phases would have increased the width of the measured signal to a higher FWHM. The degree of deviation from single-crystal behavior of the SC fiber is below the detection limit of the apparatus used, hence proving the high crystallinity of these samples.

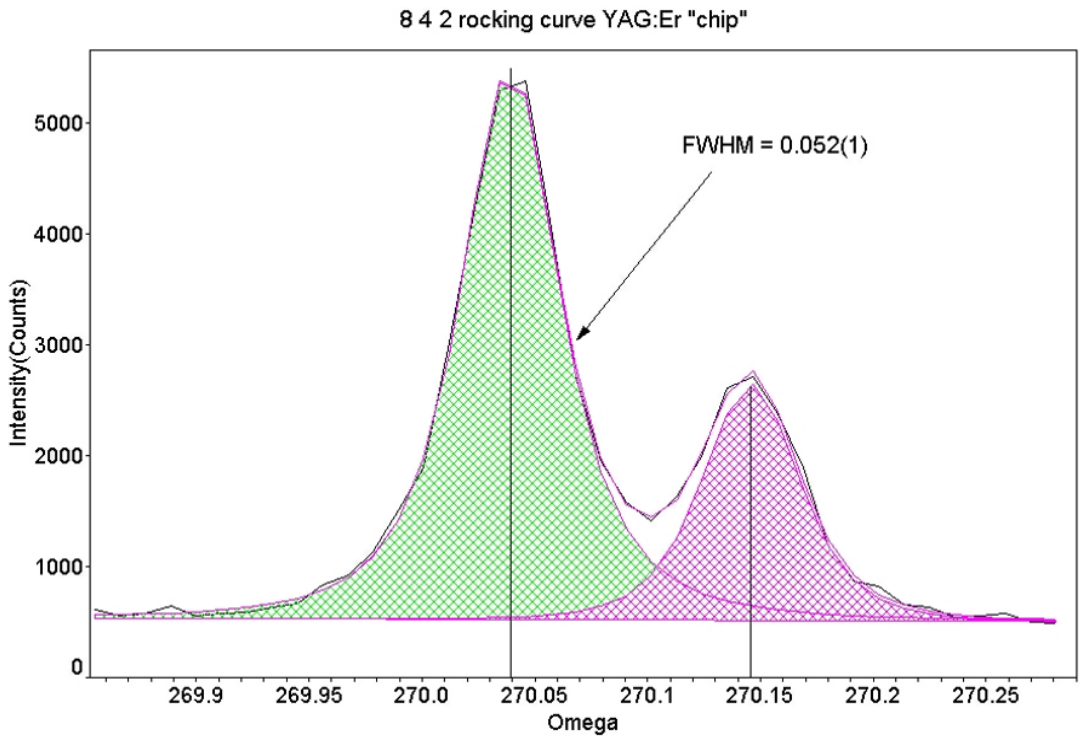

Figure 10.4: Rocking curve of a Er:YAG SC fiber

10.3 Crystal Surface Quality

The surface roughness of the SC fibers measured by atomic force microscopy (AFM) revealed that fibers which showed no visible facets demonstrated very smooth surfaces with surface roughness of about 2 nm (see Fig. 10.5). Fibers which displayed visible facets showed very periodic variation of the surface, with facet height of about 30 nm to 60 nm. Such variations are small compared to the wavelength of light in the visible and infrared spectra and are not likely to affect transmission characteristics of the fibers. Surface of some small diameter YAG SC fibers exhibited features that represented blisters (see Fig. 10.6). However, no other details about the origin of these features could be gleaned. Surface roughness of the cladding layer grown by hydrothermal growth was also characterized using AFM. The surface of the hydrothermal layer did not exhibit any periodic waviness associated with faceted fibers, but it was not as smooth as the unclad fiber surface (see Fig. 10.7). For the unclad fibers, loss measurements showed no direct correlation between faceting and transmission losses. However, transmission losses likely to arise out of facet-induced stress in the fibers were not characterized.

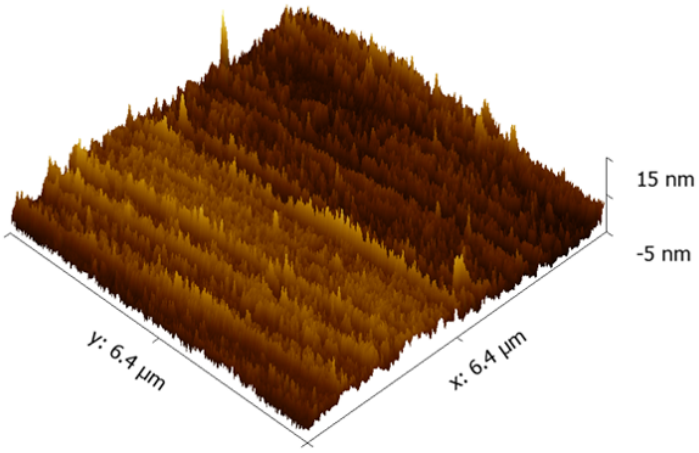

Figure 10.5: AFM image of 330 μm YAG SC fiber showing no visible faceting

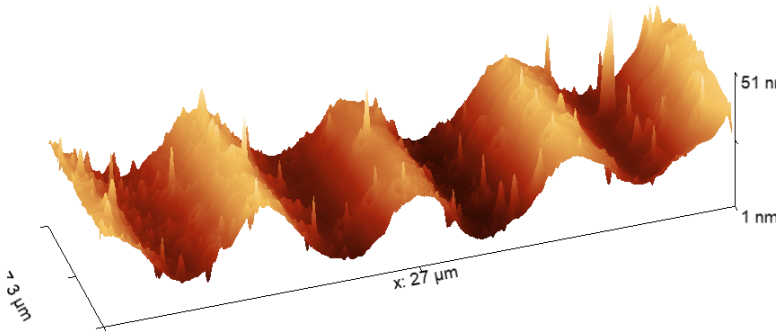

Figure 10.6: AFM image of 120 μm Nd, Ho codoped YAG SC fiber showing visible faceting. The peak-to-peak distance of the facets is 6.5 μm. The average height of the peaks, measured from the trough, is about 25 nm. RMS value of surface roughness is 8.5 nm

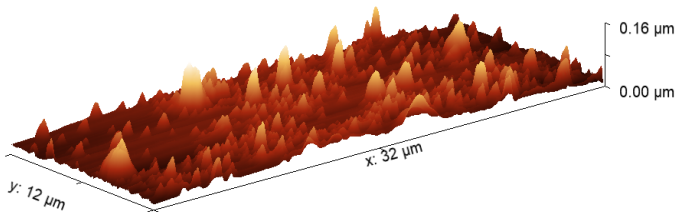

Figure 10.7: AFM image of 120 μm YAG SC fiber with 25 μm YAG cladding grown by hydrothermal crystal growth. RMS value of surface roughness is 14.5 nm

Chapter 11

X-Ray Topography

The output power obtained from a fiber laser depends strongly on the optical quality of the doped fiber. Due to defects in the crystal, optical energy from both the pump and laser wavelengths can be lost as heat. General optical characterization techniques like attenuation measurements and scattering measurements allow us to assess the quality of a fiber but they don't provide any information on the origin of these losses. In order to improve the quality of the fibers, it is important to learn about the imperfections present in it, so suitable remedial measures can be taken. Analysis should be done to understand the nature, origin, and distribution of defects present in the single crystals.

Among different microscopy-based characterization techniques like SEM, TEM, AFM, etc., x-ray diffraction topography has emerged as a comprehensive analysis technique for large single crystals. X-ray diffraction topography, or x-ray topography in short, is a non-destructive technique to characterize the microstructure of large crystalline samples. Using a high brightness x-ray source, this technique can be used to map the microstructure of a crystal and hence study the nature and distribution of defects in the bulk as well as the surface for samples ranging from microns to tens of centimeters [110].

In this technique, a collimated ribbon of x-ray illuminates a crystalline sample to yield a diffraction pattern. Depending on the shape and dimensions of the sample the diffraction pattern can be recorded in the transmission as well as in the back-reflection geometry. The diffraction pattern, which arises as different crystallographic planes satisfy the Bragg condition, can be projected onto a detector or film and can be recorded for further analysis. Variation in the intensity of the diffraction images as a function of position can be observed due to local diffracting condition in the crystal. Different types of defects in crystals can be identified and studied by analyzing the diffraction contrast which arise due to variation in local diffraction conditions. Since there is no magnification involved in the measurement process, a direct correlation can be made between a defect and its position with respect to a crystal. Further rigorous quantitative investigation of defect direction is also possible by studying the contrast in the x-ray topographs. Such an analysis would require detailed understanding of the mechanism of formation of different defects using kinematical and dynamical theories of diffraction.

While x-ray topography experiments can be performed using ordinary lab-based x-ray sources, they are limited by the considerable divergence and low intensity of the x-ray beam that may not be adequate for the proper analysis of large scale crystals. This has prompted the development of x-ray topography techniques based on sources of synchrotron radiation. Such sources have several advantages like high brightness, negligible divergence, tunability, etc. There are two different synchrotron-radiation-based x-ray topography techniques that are generally used to study single crystals, white-beam x-ray topography and monochromatic-beam x-ray topography. For the analysis of YAG SC fibers, synchrotron white-beam x-ray topography (SWBXT) was used.

SWBXT experiments were carried out at Beamline 1-BM-B,C, Advanced Photon Source at the Argonne National Laboratory. Due to the highly curved surface

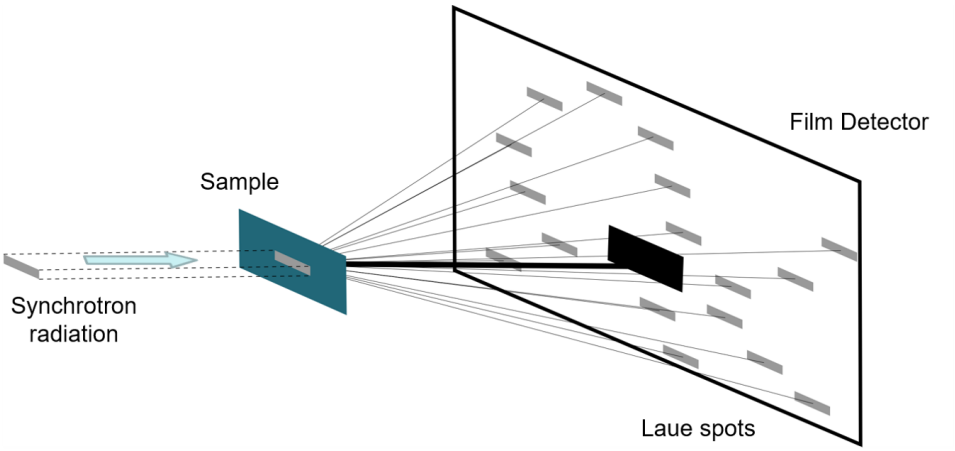

Figure 11.1: Schematic for recording projection x-ray topographs

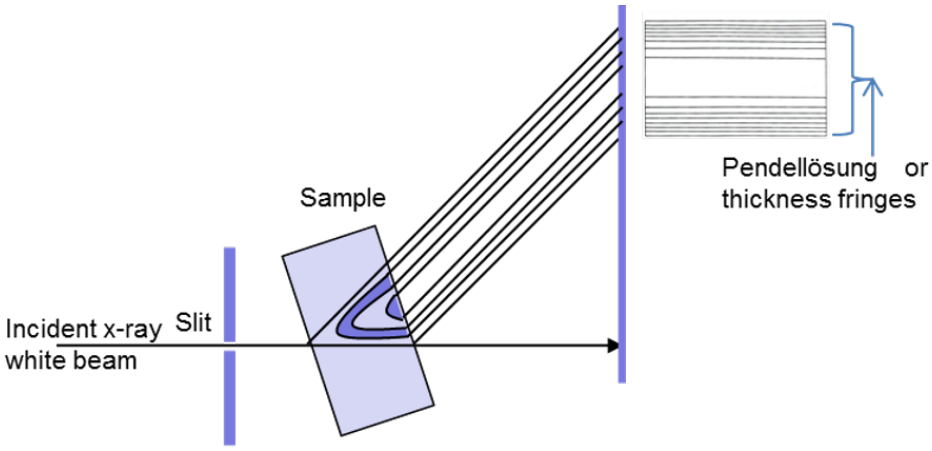

Figure 11.2: Schematic for recording section x-ray topographs

of the crystal fibers, back-reflection geometry topographs were difficult to record and hence only transmission geometry was employed. The transmission topographs were recorded in two different configurations, projection topographs and section topographs. While in the projection configuration the entire available beam of the syncrotron radiation is used to image sample, in the section topograph configuration, a slit is used to allow a very narrow ribbon of x-ray to hit the sample (see Figs. 11.1 & 11.2). Section topography is used for imaging the cross-section of a sample. Topographs were recorded on Agfa D3-SC high-resolution x-ray films, placed 15 cm behind the sample. The recorded Laue patterns were analyzed in LauePt, a software for simulating X-ray diffraction patterns in various geometries [111]. Since the diffraction measurements provided no magnification, the topographs were analyzed under an optical microscope to reveal contrast variations. Analysis of the topographs were done with the assistance of Dr. Balaji Raghothamachar of Stony Brook University.

Topographs of most of the YAG SC fibers showed that the samples were dislocation-free single crystals with no evidence of amorphous phases or twinning. For the dislocation-free samples, the shape of the x-ray topograph corresponded to the actual shape of the fiber indicating that there was no significant strain in the crystal lattices. A common feature observed in the samples was the presence of growth striations. These striations, which originate from fluctuations in the melt flux, appeared like alternate bands on the topographs. They represented the history of the crystal growth by recording the shape and changes of the solid-liquid interface of the growth. In the case of SC fibers, the fluctuations in the melt were most likely due to variation in pulling rate and temperature changes in the melt. In order to maintain a constant fiber diameter, the automatic diameter control changed the pulling rate of the fiber instantaneously. This induced changes in the volume flux of the melt, introducing inhomogeneous strain along the fiber length. The other source of the fluctuations was due to temperature changes near the solid-liquid interface. These could arise

from fluctuations in laser power and non-centrosymmetric heat in the melt due to misalignment of optical components. Apart from regions of varying strain, growth variations could also cause inhomogeneous incorporation of dopants which have a non-unity segregation coefficient [112]. Hence, in doped YAG SC fibers the striations were associated with variation in both strain as well as dopant concentration and were usually very pronounced (see Fig. 11.3, 11.4, and 11.5).

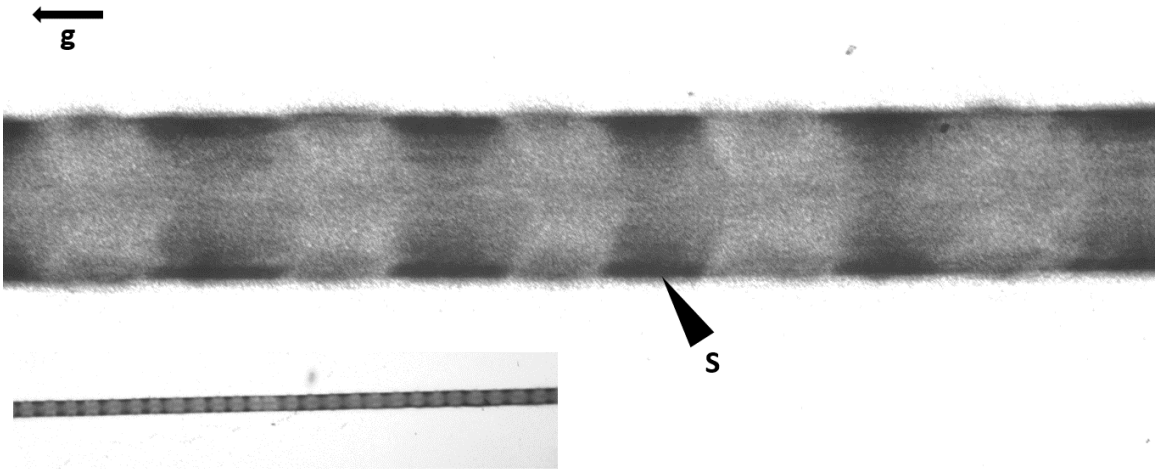

Figure 11.3: X-ray topograph ($g = 00\bar{4}$) of 330 μm diameter 1.5% Nd:YAG SC fiber with periodic striations showing incorporation of Nd^{3+} ions in the fiber. The inset shows the longer section of the fiber.

Significant distortion of the crystal lattice was noted for the 330 μm Nd:YAG SC fibers(see Fig. 11.6). Since the Nd^{3+} ions are about 12% larger than the host Y^{3+} ions, they caused observable distortion of the lattice. This particular sample also displayed dislocation lines running through the center of the fiber. The auto-segregation phenomenon of Nd ions in YAG has been discussed in a previous chapter. Increased concentration of Nd ions in the center of the crystal growth front leads to constitutional super-cooling [113]. Liu *et al.* [98], in their work on Mg doped sapphire SC fibers, have suggested that if the concentration of dopant does not increase in the solid phase, the interface breaks down at the center, leading to dislocations and ultimately cracking at the center of the fiber. The same phenomenon is likely to be

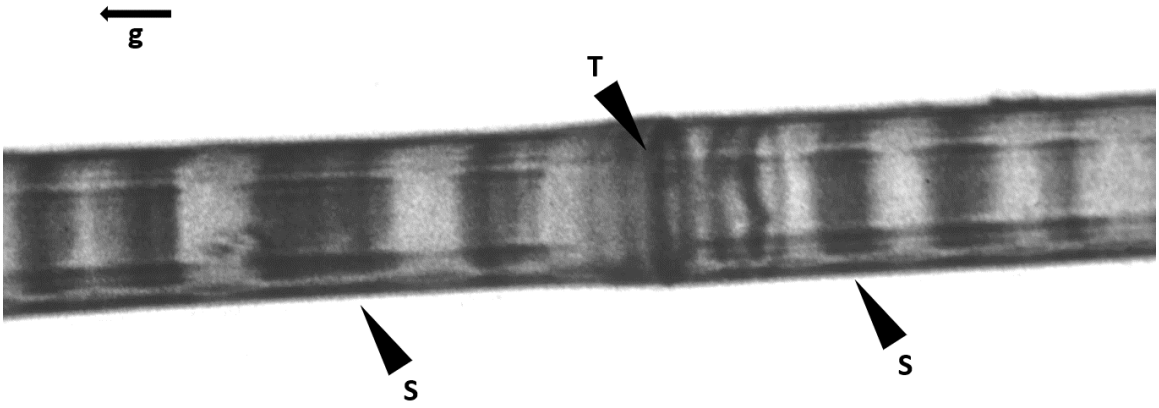

Figure 11.4: X-ray topograph ($g = 00\bar{4}$) of 380 μm diameter Er:YAG SC fiber showing periodic striations showing incorporation. The sample shows significant stress at point at region T which is at the transition point of two tube sections. (Please refer to 7.4.1 for more details of growth)

at play for Nd doped YAG. Constitutional supercooling arising from segregation of the Nd ions in the center of the fiber leads to cracking in the center of the fiber. Since constitutional supercooling can be controlled by adjusting factors like crystal diameter, temperature gradient, and pulling rates, cracking at the center of the crystal fiber can be avoided. This is perhaps the reason why a similar result could not be verified for the 120 μm Nd, Ho co-doped YAG SC fibers. Although the sample displayed striations, it did not show the significant lattice distortion due to the Nd ions.

Samples of varying thickness (or wedge-shaped samples) with high crystalline perfection give rise to very fine fringes called Pendellösung fringes. Such fringes are produced as dynamical effects of x-ray diffraction and can be only seen in single crystals where the lattice planes are exactly parallel to each other. Any strain or defects that affect the orientation of the planes will cause the effect not to be observed. Topographs of two different 330 μm diameter undoped YAG SC fiber samples exhibited this effect (see Fig. 11.7). These fringes were visible as parallel horizontal lines run-

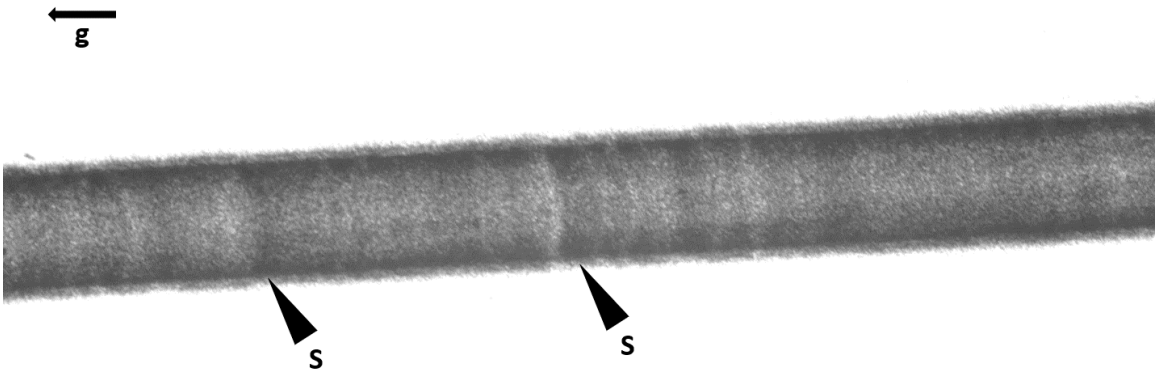

Figure 11.5: X-ray topograph of ($g = 00\bar{4}$) 120 μm diameter Nd, Ho co-doped YAG SC fiber showing periodic striations showing incorporation of Nd^{3+} ions in the fiber. Blurring of the topograph signifies significant strain the crystal.

ning along the length of the fiber. It was unsurprising to note that these samples were obtained from two fibers with very low losses. If significant strain is present in the fibers, Pendellösung fringes are not visible, even if no other defects or boundaries are present. From the samples analyzed in this study, a strong correlation could be drawn between losses and strain in fibers. While the strain-free fibers shown in Fig. 11.8 a) had losses less than 0.3 dB/m (at 1064 nm), the fiber shown in Fig. 11.8 b), which was characterized by strain, had an attenuation loss of 1.2 dB/m. The presence of other defects deteriorated the losses even further. The topograph of a 330 μm diameter undoped YAG SC fiber with losses more than 1.8 dB/m is shown in Fig 11.9. It displayed several defects which resemble inclusions. Compared to the 330 μm diameter YAG SC fibers, the topographs of the 120 μm diameter fibers were characterized by higher degree of strain. This was very reasonable as a tighter focus of the laser beam was required to form a uniform melt from which good quality small diameter fibers could be grown.

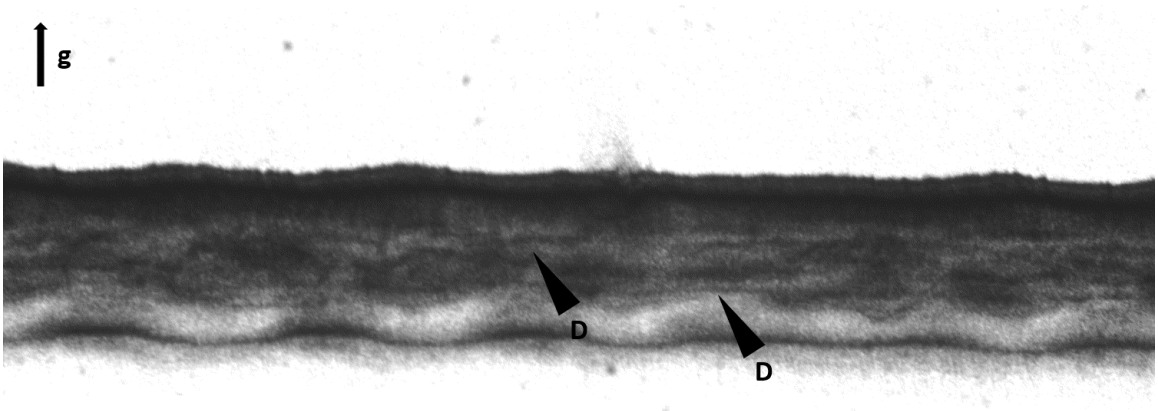

Figure 11.6: X-ray topograph ($g = 2\bar{2}0$) of 330 μm diameter 1.5% Nd:YAG SC fiber showing dislocation lines running through the center of the fiber (D). The sample also shows the strain in the lattice due to periodic incorporation of Nd^{3+} ions in the fiber

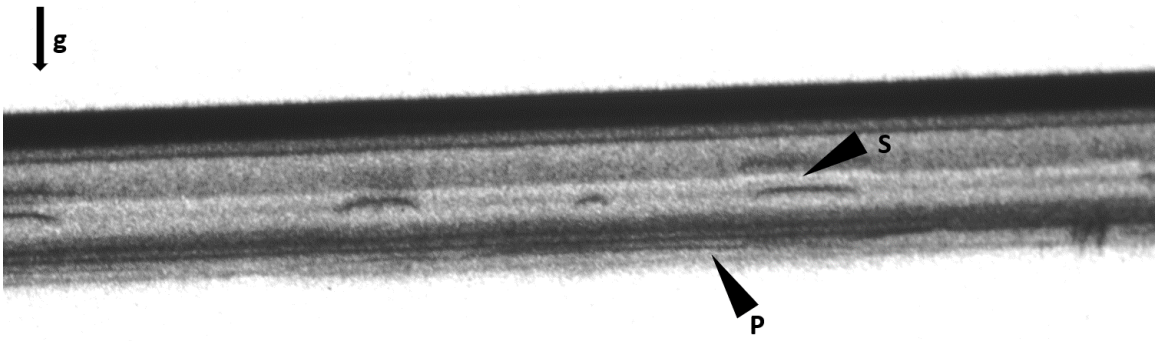

Figure 11.7: X-ray topograph ($g = 040$) of 330 μm diameter undoped YAG SC fiber showing Pendellösung fringes (P). S - Surface defects on the fiber surface

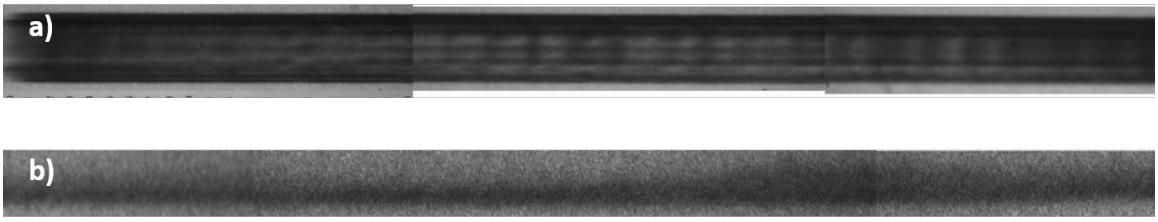

Figure 11.8: X-ray topograph of two 330 μm diameter undoped YAG SC fibers. a) Strain-free fiber with transmission losses of 0.3 dB/m. Horizontal lines are Pendellösung or thickness fringes produced by dynamical diffraction effects indicative of high crystalline perfection. b) Fiber is characterized by strains resulting in blurred images.

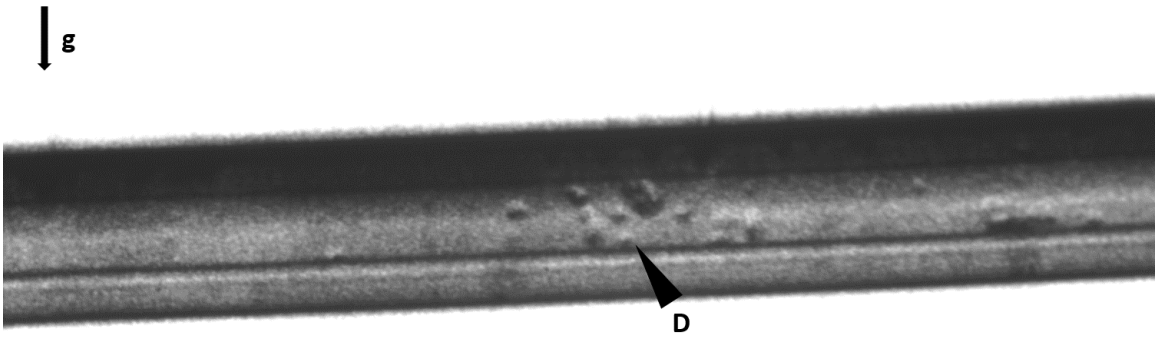

Figure 11.9: X-ray topograph ($g = 2\bar{2}0$) of 330 μm diameter undoped YAG SC fiber showing inclusion defects (D).

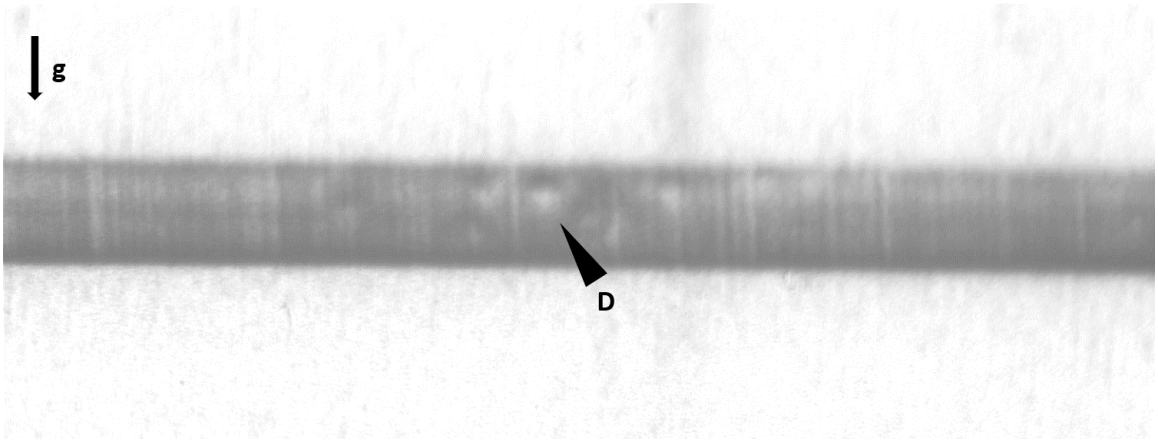

Figure 11.10: Section X-ray topograph ($g = 2\bar{2}0$) of 330 μm diameter undoped YAG SC fiber showing inclusion defects (D).

X-ray topograph of YAG SC fibers with a hydrothermal layer of cladding revealed some interesting details about the composite crystal structure (see Fig. 11.11 and 11.12). The cladding layer was observed to be highly strained. This could be inferred from the fact that the shape of the topograph was not representative of the actual sample.

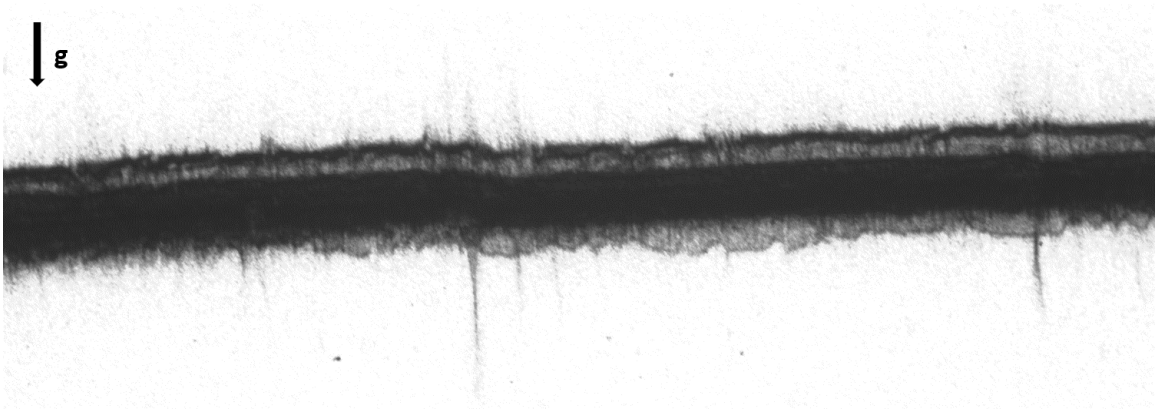

Figure 11.11: X-ray topograph ($g = 040$) of 120 μm diameter undoped YAG SC fiber with 25 μm cladding layer grown by hydrothermal method.

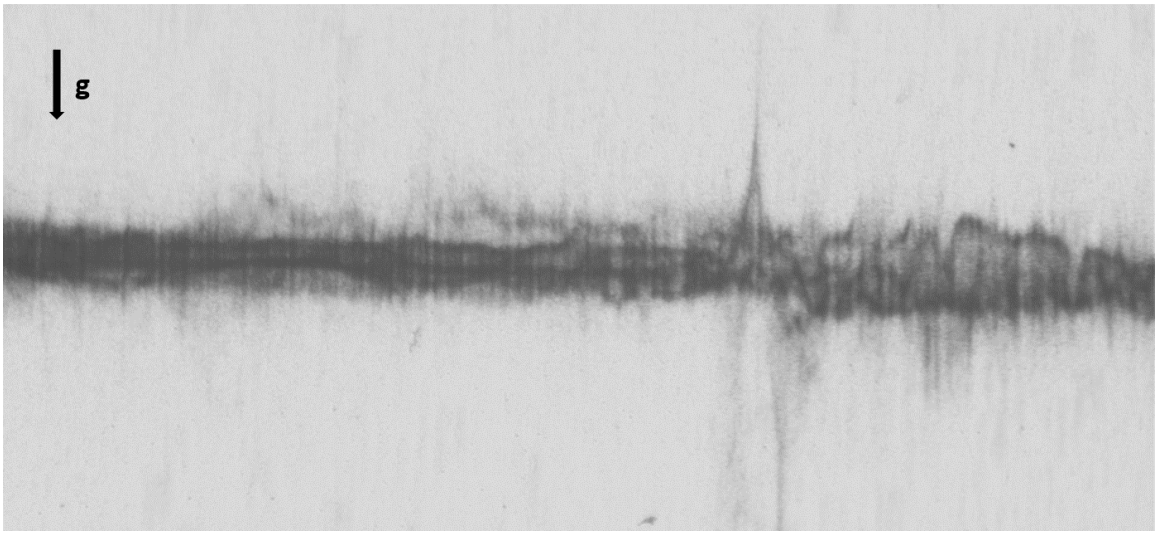

Figure 11.12: Section X-ray topograph ($g = 040$) of 120 μm diameter undoped YAG SC fiber with 25 μm cladding layer grown by hydrothermal method.

Part V

Summary and Conclusions

Chapter 12

Conclusion and Future Work

Significant improvements in the LHPG technique have led to the growth of low-loss YAG SC fibers of consistent excellent single-crystalline quality. Modifications to the LHPG system have included installation of a double axicon system, height adjustable laser micrometer, and three-axis viewing among others. Aided by simulations of beam propagation through different components of the LHPG apparatus, the alignment of the optics was fine-tuned to achieve a tight and highly symmetric focal spot. The improved focusing of the CO_2 laser radiation resulted in a uniform melt which was crucial to growing high-quality SC YAG fibers. Attenuation losses in 330 μm YAG SC fibers have been lowered from more than 15 dB/m (at 1064 nm) to less than 0.1 dB/m. Using the optimized LHPG apparatus, low-loss 120 μm YAG SC fibers were also grown. The losses of these fibers were comparable to the losses measured in 330 μm YAG SC fibers. The lowest loss measured for a 120 μm fiber was 0.3 dB/m at 1064 nm.

Improvements in optical alignment of the LHPG system led to the reduction of scattering losses in the YAG SC fibers. This was very well demonstrated in the low-loss 330 μm YAG SC fibers where there was no strong dependence of attenuation loss on fiber length. One such fiber was a 1-meter long YAG SC fiber which had a loss

of 0.3 dB/m (at 1064 nm) with scattering losses less than 0.2 dB/m for most part of its length. Compared to these fibers the low-loss 120 μm YAG SC fibers showed a stronger dependence of attenuation losses on fiber length. This is most likely due to coupling of optical power into higher order modes which results from the increased diameter variation. The scattering losses in all the YAG SC fibers demonstrated a strong dependence on wavelength with scattering varying as λ^{-n} where n lies in the interval from 2.4 to 3.8. This signified that the scattering mechanism was neither purely Rayleigh scattering ($n = 4$) nor Rayleigh-Gans scattering ($n = 2$). Apart from this, no further conclusions could be made regarding the mechanism of such scattering process.

Several methods for growing crystalline cladding for SC YAG fibers were attempted with varying degrees of success. Cladding layers of alumina and YAG were grown using sol-gel methods. Despite optimizing the sol-gel dip coating technique to yield crack-free consistent layers, the thickness of the cladding layers was not close to the desired thickness required for a double-clad fiber. Liquid phase deposition was used to deposit a layer of germania on a YAG SC fiber as a cladding layer. While the thickness of the GeO_2 layer achieved by this method was sufficient, the quality of the crystalline cladding layer was below required standards. The most promising cladding approach was by using hydrothermal crystal growth technique. A 25 μm thick cladding layer of YAG was deposited around a 120 μm YAG SC fiber. While at present this technique only allows for the cladding of fiber sections less than 5 cm, it can be optimized for cladding longer fiber lengths. In-situ cladding growth was attempted by growing fibers from RiT preform with 50% Er:YAG core. The radial gradient of dopant distribution exhibited in these fibers can be used as a basis for growing monolithic SC fibers with graded index profile.

While the ultimate goal to develop a double-clad SC fiber laser was not achieved, significant improvements in the fabrication of 330 μm diameter 0.5% Ho:YAG SC

fiber have led to the demonstration of optical-to-optical slope efficiency of 72.3% at 2090.6 nm. This is the highest slope efficiency reported for a holmium doped crystal fiber. Using a simple low-cost sol-gel based approach, SC YAG fibers of 120 μm diameter and with varied Ho^{3+} ion concentrations have been grown. When pumped at 1.908 μm, the fibers show significant output at the lasing wavelength of 2.09 μm, with a maximum of 58.5% optical-to-optical slope efficiency. Compared to results for 330 μm YAG fibers, the slope efficiency is lower. This is likely due to increased scattering losses for the smaller diameter fibers. Additionally, the 120 μm fibers were observed to have a lower lasing threshold compared to the 330 μm fibers.

Effect of seed orientation on fiber faceting was explored and was determined that using an oriented seed was neither the necessary, nor the sufficient condition for growing facet-free fibers. SWBXT in conjunction with single crystal x-ray diffraction was successfully used to characterize the quality of the crystals. The different analyses show that the LHPG grown YAG SC fibers are mostly defect-free with very high crystallinity, free from twinning or amorphous phases.

Future Work

RE doped SC fibers offer great potential as gain medium for high power lasers due to their superior material quality. The two main hindrances that have prevented this technology from being commercially adopted are the high losses in SC fibers and the absence of a core-clad structured all-crystalline SC fiber. While the work done in this project has addressed the loss issue to a satisfactory degree, despite our best efforts much needs to be done to develop an effective crystalline cladding for SC fibers. Further research into the development of cladding would be immensely beneficial to this field.

Hydrothermal growth of crystal has been shown to be an effective approach to

growing a crystalline cladding for SC fibers. At present, the length of the fiber section that can be clad by this technique is limited by the dimension of the autoclave available. Future projects could look into the most effective approach to using hydrothermal growth to clad fibers of longer lengths. These studies could also look into refining the hydrothermal growth process so as to reduce the strain in the hydrothermal layer to allow for more flexibility of the SC fiber.

The auto-segregation of dopant like Nd^{3+} ions in YAG was one of the most interesting phenomenon observed during the project. This particular observation presents a lot of potential and possibilities. Further studies could investigate the movement of ions during the LHPG of different doped materials in more detail, using simulations to develop a definite relation between radial dopant distribution and factors like dopant ion size, host ion size, growth speed, operating power of processing laser, etc. In particular, since it has been observed that ions which are significantly larger than the host ion they replace demonstrate considerable segregation, different host matrices can be explored to study the behavior of different dopant ions. Two of the most interesting systems would be Ho:LuAG and Ho,Th:LuAG. These systems present a strong possibility of demonstrating appreciable radial distribution of the lasing Ho^{3+} ions, forming graded-index SC fibers.

The use of electric-field assisted diffusion to achieve an in-situ cladding had been discussed during the project. The idea was to use a strong centro-symmetric electric field at the solid-liquid junction during the LHPG to affect the preferential movement of the dopant ions. While the idea showed positive results on simulation, the idea was eventually dropped due to the difficulties in incorporating the electric field generating elements in the present LHPG apparatus. A future project could be designed to study the behavior of dopants under such an electric field.

Last but not least, the idea of using sol-gel based techniques to vary dopant ion concentration in SC fibers can be explored in detail. This low-cost technique offers the

possibility of not only varying dopant concentration in SC fibers without sacrificing crystal quality, it allows for the easy growth of SC fibers with regions of different dopants and multi-ion co-doped SC fibers. This opens the exciting possibility of fabricating a monolithic all-SC-fiber architecture including components like saturable absorbers, gain media, faraday rotators, sensors, etc.

References

[1] H. Jelínková, editor. *Lasers for medical applications: diagnostics, therapy and surgery*. Elsevier, 2013.

[2] T. Fujii and T. Fukuchi. *Laser remote sensing*. CRC press, 2005.

[3] A. K. Majumdar and J. C. Ricklin. *Free-space laser communications: principles and advances*, volume 2. Springer Science & Business Media, 2010.

[4] A. Yariv and P. Yeh. *Photonics: optical electronics in modern communications*, volume 6. Oxford University Press New York, 2007.

[5] C. Weitkamp. *Lidar: range-resolved optical remote sensing of the atmosphere*, volume 102. Springer Science & Business, 2006.

[6] J. Sanghera and I. D. Aggarwal. *Infrared fiber optics*. CRC Press, 1998.

[7] S. Chénais, F. Druon, S. Forget, F. Balembois, and P. Georges. On thermal effects in solid-state lasers: The case of ytterbium-doped materials. *Progress in quantum electronics*, 30(4):89–153, 2006.

[8] G. P. Agrawal. *Nonlinear Fiber Optics*. Academic Press, 2013.

[9] R. G. Smith. Optical power handling capacity of low loss optical fibers as determined by stimulated Raman and Brillouin scattering. *Appl. Opt.*, 11(11):2489, Jan 1972.

[10] P. Moulton. Ti-doped sapphire: tunable solid-state laser. *Optics News*, 8(6):9–9, 1982.

[11] R. Chesler, J. Geusic, and M. Karr. A practical, high-repetition rate Q-switched Nd:YAG laser. *IEEE J. Quant. Electron*, 5(6):345–345, 1969.

[12] R. C. Linares. Growth of garnet laser crystals. *Solid State Communications*, 2(8):229–231, 1964.

[13] B. R. Sutherland and E. H. Sargent. Perovskite photonic sources. *Nature Photonics*, 10(5):295–302, 2016.

[14] C. Kränkel. Rare-earth-doped sesquioxides for diode-pumped high-power lasers in the 1-, 2-, and 3-μm spectral range. *IEEE Journal of Selected Topics in Quantum Electronics*, 21(1):250–262, 2015.

[15] L. DeShazer. Vanadate crystals exploit diode-pump technology. *Laser Focus World*, 30(2):88 – 90, 1994.

[16] L. I. Ivleva, T. T. Basiev, I. S. Voronina, P. G. Zverev, V. V. Osiko, and N. M. Polozkov. $SrWO_4$: Nd^{3+}- new material for multifunctional lasers. *Optical Materials*, 23(1):439–442, 2003.

[17] T. A. Parthasarathy, R. S. Hay, G. Fair, and F. K. Hopkins. Predicted performance limits of yttrium aluminum garnet fiber lasers. *Optical Engineering*, 49(9):094302–094302–8, 2010.

[18] J. Aus Der Au, G. J. Spühler, T. Südmeyer, R. Paschotta, R. Hövel, M. Moser, S. Erhard, M. Karszewski, A. Giesen, and U. Keller. 16.2-w average power from a diode-pumped femtosecond Yb:YAG thin disk laser. *Optics Letters*, 25(11):859–861, 2000.

[19] A. Dergachev, J. H. Flint, Y. Isyanova, B. Pati, E. V. Slobodtchikov, K. F Wall, and P. F. Moulton. Review of multipass slab laser systems. *IEEE Journal of Selected Topics in Quantum Electronics*, 13(3):647–660, 2007.

[20] J. S. Haggerty. Production of fibers by a floating zone fiber drawing technique. Report, Final Report NASA-CR-120948, 1972.

[21] C. A. Burrus and J. Stone. Single crystal fiber optical devices: A Nd:YAG fiber laser. *Applied Physics Letters*, 26(6):318–320, 1975.

[22] M. Fejer, R. L. Byer, R. Feigelson, and W. Kway. Growth and characterization of single crystal refractory oxide fibers. *Advances in Infrared Fibers II*, 1982.

[23] R. S. Feigelson, W. L. Kway, and R. K. Route. Single crystal fibers by the laser-heated pedestal growth method. *Optical Engineering*, 24(6):241102–241102–, 1985.

[24] R. K. Nubling and J. A. Harrington. Optical properties of single-crystal sapphire fibers. *Appl. Opt.*, 36(24):5934, 1997.

[25] C. Y. Lo, P. L. Huang, T. S. Chou, L. M. Lee, T. Y. Chang, S. L. Huang, L. Lin, H. Y. Lin, and F. C. Ho. Efficient Nd:$Y_3Al_5O_{12}$ crystal fiber laser. *Japanese Journal of Applied Physics*, 41(11A):L1228, 2002.

[26] I. Martial, S. Bigotta, M. Eichhorn, C. Kieleck, J. Didierjean, N. Aubry, R. Peretti, F. Balembois, and P. Georges. Er:YAG fiber-shaped laser crystals (single crystal fibers) grown by micro-pulling down: Characterization and laser operation. *Optical Materials*, 32(9):1251–1255, 2010.

[27] X. Délen, S. Piehler, J. Didierjean, N. Aubry, A. Voss, M. A. Ahmed, T. Graf, F. Balembois, and P. Georges. 250 w single-crystal fiber Yb:YAG laser. *Optics letters*, 37(14):2898–2900, 2012.

[28] Y. Li, K. Miller, E. G. Johnson, C. D. Nie, S. Bera, J. A. Harrington, and R. Shori. Lasing characteristics of Ho:YAG single crystal fiber. *Optics express*, 24(9):9751–9756, 2016.

[29] S. Ishibashi, K. Naganuma, and I. Yokohama. Cr, Ca :$Y_3Al_5O_{12}$ laser crystal grown by the laser-heated pedestal growth method. *Journal of Crystal Growth*, 183(4):614–621, 1998.

[30] J. W. Dawson, M. J. Messerly, R. J. Beach, M. Y. Shverdin, E. A. Stappaerts, A. K. Sridharan, P. H. Pax, J. E. Heebner, C. W. Siders, and C. P. J. Barty. Analysis of the scalability of diffraction-limited fiber lasers and amplifiers to high average power. *Optics Express*, 16(17):13240–13266, 2008.

[31] J. W. Dawson, M. J. Messerly, J. E. Heebner, P. H. Pax, A. K. Sridharan, A. L. Bullington, R. J. Beach, C. W. Siders, C. P. J. Barty, and M. Dubinskii. Power scaling analysis of fiber lasers and amplifiers based on non-silica materials, 2010.

[32] V. Fomin, V. Gapontsev, E. Shcherbakov, A. Abramov, A. Ferin, and D. Mochalov. 100 kw cw fiber laser for industrial applications. In *2014 International Conference Laser Optics*, pages 1–1, June 2014.

[33] D. B. Keck. Optical fiber spans 30 years. *Lightwave*, 17(8):78–82, 2000.

[34] Corning Inc. Corning® SMF-28® Ultra optical fiber, 2014.

[35] J. Ballato, T. Hawkins, P. Foy, B. Kokuoz, R. Stolen, C. McMillen, M. Daw, Z. Su, T. M. Tritt, M. Dubinskii, J. Zhang, T. Sanamyan, and M. J. Matthewson. On the fabrication of all-glass optical fibers from crystals. *Journal of Applied Physics*, 105(5):053110, 2009.

[36] G. Mueller. The czochralski method-where we are 90 years after Jan Czochralski's invention. *Crystal Research and Technology*, 42(12):1150–1161, 2007.

[37] K. Kakimoto. Czochralski silicon single crystals for semiconductor and solar cell applications. In *Springer Handbook of Crystal Growth*, pages 231–243. Springer, 2010.

[38] V. V. Osiko, M. A. Borik, and E. E. Lomonova. Synthesis of refractory materials by skull melting technique. In *Springer handbook of crystal growth*, pages 433–477. Springer, 2010.

[39] V. A. Tatartchenko. Shaped crystal growth. In *Springer Handbook of Crystal Growth*, pages 509–556. Springer, 2010.

[40] M. H. Lewis. Defects in spinel crystals grown by the Verneuil process. *Philosophical Magazine*, 14(131):1003–1018, 1966.

[41] H. E. LaBelle. Growth of controlled profile crystals from the melt: Part ii-edge-defined, film-fed growth (EFG). *Materials Research Bulletin*, 6(7):581–589, 1971.

[42] B. Chalmers, H. E. LaBelle, and A. I. Mlavsky. Edge-defined, film-fed crystal growth. *Journal of Crystal Growth*, 13:84–87, 1972.

[43] T. Fukuda and V. I. Chani. *Shaped Crystals: Growth by Micro-Pulling-Down Technique*. Springer Berlin Heidelberg, 2007.

[44] A. Yoshikawa, B. M. Epelbaum, T. Fukuda, K. Suzuki, and Y. Waku. Growth of $Al_2O_3/Y_3Al_5O_{12}$ eutectic fiber by micro-pulling-down method and its high-temperature strength and thermal stability. *Japanese Journal of Applied Physics*, 38(1A):L55, 1999.

[45] A. Yoshikawa, M. Nikl, G. Boulon, and T. Fukuda. Challenge and study for developing of novel single crystalline optical materials using micro-pulling-down method. *Optical Materials*, 30(1):6–10, 2007.

[46] J. Didierjean, M. Castaing, F. Balembois, P. Georges, D. Perrodin, J. M. Fourmigué, K. Lebbou, A. Brenier, and O. Tillement. High-power laser with Nd:YAG single-crystal fiber grown by the micro-pulling-down technique. *Optics letters*, 31(23):3468–3470, 2006.

[47] W. Kim, B. Shaw, S. Bayya, C. Askins, J. Peele, D. Rhonehouse, J. Meyers, R. Thapa, D. Gibson, and J. Sanghera. Cladded single crystal fibers for high power fiber lasers, 2016.

[48] T. Akashi, K. Matumi, T. Okada, and T. Mizutani. Preparation of ferrite single crystals by new floating zone technique. *IEEE Transactions on Magnetics*, 5(3):285–289, 1969.

[49] R. E. De La Rue and F. A. Halden. Arc-image furnace for growth of single crystals. *Review of Scientific Instruments*, 31(1):35–38, 1960.

[50] H. A. Dabkowska and A. B. Dabkowski. Crystal growth of oxides by optical floating zone technique. In *Springer Handbook of Crystal Growth*, pages 367–391. Springer, 2010.

[51] C. D. Nie, S. Bera, and J. A. Harrington. Attenuation and scattering loss of single-crystal YAG fiber optics. Manuscript in preparation.

[52] J. A. Harrington. *Infrared fibers and their applications*. SPIE Optical Engineering Press, Bellingham, Wash., 2004.

[53] A Sa'ar and A Katzir. Scattering effects in crystalline infrared fibers. *JOSA A*, 5(6):823–833, 1988.

[54] A. W. Snyder and J. Love. *Optical waveguide theory*. Springer Science & Business Media, 2012.

[55] C. A. Morrison. *Crystal fields for transition-metal ions in laser host materials*. Springer Science & Business Media, 2012.

[56] R. Moncorgé. Laser materials based on transition metal ions. *Optical Materials*, 63(Supplement C):105 – 117, 2017. In honor of Professor Georges Boulon for his outstanding contributions to Optical Materials.

[57] M. J. F. Digonnet. *Rare-earth-doped fiber lasers and amplifiers, revised and expanded*. CRC press, 2001.

[58] A. J. Kenyon. Recent developments in rare-earth doped materials for optoelectronics. *Progress in Quantum Electronics*, 26(4):225–284, 2002.

[59] A. A. Kaplyanskii and R. M. McFarlane. *Spectroscopy of Crystals Containing Rare Earth Ions*, volume 21. Elsevier, 2012.

[60] K. W. Krämer, P. Dorenbos, H. Güdel, and C. W. E. Van Eijk. Development and characterization of highly efficient new cerium doped rare earth halide scintillator materials. *Journal of Materials Chemistry*, 16(27):2773–2780, 2006.

[61] P. C. de Sousa Filho, J. F. Lima, and O. A. Serra. From lighting to photoprotection: Fundamentals and applications of rare earth materials. *Journal of the Brazilian Chemical Society*, 26(12):2471–2495, 2015.

[62] R. Reisfeld and C. K. Jorgensen. *Lasers and excited states of rare earths*, volume 1. Springer Science & Business Media, 2012.

[63] B. M. Walsh. Judd-Ofelt theory: principles and practices. In *Advances in Spectroscopy for Lasers and Sensing*, pages 403–433. Springer, 2006.

[64] M. P. Hehlen, M. G. Brik, and K. W. Krämer. 50th anniversary of the Judd-Ofelt theory: An experimentalist's view of the formalism and its application. *Journal of luminescence*, 136:221–239, 2013.

[65] G. H. Dieke and H. M. Crosswhite. The spectra of the doubly and triply ionized rare earths. *Applied Optics*, 2, 1963.

[66] E. Snitzer, H. Po, F. Hakimi, R. Tumminelli, and B. C. McCollum. Erbium fiber laser amplifier at 1.55 μm with pump at 1.49 μm and Yb sensitized Er oscillator. In *Optical Fiber Communication Conference*, page PD2. Optical Society of America, 1988.

[67] A. A. Kaminskii. *Laser crystals: their physics and properties*, volume 14. Springer, 2013.

[68] C. K. Asawa and M. Robinson. Temperature-dependent concentration quenching of fluorescence by cross relaxation of Nd^{3+} in LaF_3. *Physical Review*, 141(1):251, 1966.

[69] P. Blixt, J. Nilsson, T. Carlnas, and B. Jaskorzynska. Concentration-dependent upconversion in Er^{3+}-doped fiber amplifiers: Experiments and modeling. *IEEE photonics technology letters*, 3(11):996–998, 1991.

[70] R. S. Feigelson. Opportunities for research on single-crystal fibers. *Materials Science and Engineering: B*, 1(1):67–75, 1988.

[71] M. R. B. Andreeta and A. C. Hernandes. Laser-heated pedestal growth of oxide fibers. In *Springer Handbook of Crystal Growth*, pages 393–432. Springer, 2010.

[72] R. K. Nubling. *Sapphire fibers for erbium:YAG and hollow waveguides for industrial carbon dioxide laser power delivery.* Thesis, Rutgers University, 1996.

[73] V. Phomsakha, R. S. F. Chang, and N. Djeu. Novel implementation of laser heated pedestal growth for the rapid drawing of sapphire fibers. *Review of Scientific Instruments*, 65(12):3860–3861, 1994.

[74] M. M. Fejer, G. A. Magel, and R. L. Byer. High-speed high-resolution fiber diameter variation measurement system. *Applied Optics*, 24(15):2362–2368, 1985.

[75] M. R. B. Andreeta, L. C. Caraschi, and A. C. Hernandes. Automatic diameter control system applied to the laser heated pedestal growth technique. *Materials Research*, 6:107–110, 2003.

[76] L. Laversenne, Y. Guyot, C. Goutaudier, M. T. Cohen-Adad, and G. Boulon. Optimization of spectroscopic properties of Yb^{3+}-doped refractory sesquioxides: cubic Y_2O_3, Lu_2O_3 and monoclinic Gd_2O_3. *Optical materials*, 16(4):475–483, 2001.

[77] S. Bera, C. D. Nie, M. G. Soskind, Y. Li, J. A. Harrington, and E. G. Johnson. Growth and lasing of single crystal YAG fibers with different Ho^{3+} concentrations. *Optical Materials*, 75:44–48, 2018.

[78] G. N. Merberg. *Optical properties of single-crystal sapphire fibers.* PhD thesis, Rutgers University, 1992.

[79] Z. Lu, L. V. Moulton, R. S. Feigelson, R. J. Raymakers, and P. N. Peszkin. Factors affecting the growth of single crystal fibers of the superconductor $Bi_2Sr_2CaCu_2O_8$. *Journal of crystal growth*, 106(4):732–741, 1990.

[80] M. M. Fejer. *Single Crystal Fibers: Growth Dynamics and Nonlinear Optical Interactions.* PhD thesis, Stanford University, 1986.

[81] C. D. Nie, S. Bera, and J. A. Harrington. Growth of single-crystal YAG fiber optics. *Optics Express*, 24(14):15522–15527, 2016.

[82] S. Bera, C. D Nie, M. G. Soskind, and J. A. Harrington. Optimizing alignment and growth of low-loss YAG single crystal fibers using laser heated pedestal growth technique. *Applied optics*, 56(35):9649–9655, 2017.

[83] K. Y. Huang, K. Y. Hsu, D. Y. Jheng, W. J. Zhuo, P. Y. Chen, P. S. Yeh, and S. L. Huang. Low-loss propagation in Cr^{4+}:YAG double-clad crystal fiber fabricated by sapphire tube assisted CDLHPG technique. *Optics Express*, 16(16):12264–12271, 2008.

[84] J. Ballato and P. Dragic. Rethinking optical fiber: new demands, old glasses. *Journal of the American Ceramic Society*, 96(9):2675–2692, 2013.

[85] Y. S. Lin, C. C. Lai, and S. L. Huang. High-resolution transmission electron microscopy analysis of the microstructures of Cr^{4+}:$Y_3Al_5O_{12}$ double-clad crystal fibers prepared by lhpg method. *Journal of Materials Science: Materials in Electronics*, 24(3):911–915, 2013.

[86] M. J. F. Digonnet, C. J. Gaeta, D. Omeara, and H. J. Shaw. Clad Nd:YAG fibers for laser applications. *Journal of Lightwave Technology*, 5(5):642–646, 1987.

[87] B. Shaw, C. Askins, W. Kim, S. Bayya, J. Peele, R. Thapa, S. R. Bowman, R. R. Gattass, and J. S. Sanghera. Cladding pumped single crystal Yb:YAG fiber amplifier. In *Advanced Solid State Lasers*, pages AM4A–4. Optical Society of America, 2015.

[88] X. Mu, S. Meissner, H. Meissner, and W. Y. Anthony. High efficiency Yb:YAG crystalline fiber-waveguide lasers. *Optics letters*, 39(21):6331–6334, 2014.

[89] C. J. Brinker, G. C. Frye, A. J. Hurd, and C. S. Ashley. Fundamentals of sol-gel dip coating. *Thin solid films*, 201(1):97–108, 1991.

[90] R. L. Kozodoy-Pins. *Development and evaluation of fiber optic delivery systems for laser surgical applications.* PhD thesis, Rutgers University, 1996.

[91] M. Veith, S. Mathur, A. Kareiva, M. Jilavi, M. Zimmer, and V. Huch. Low temperature synthesis of nanocrystalline $Y_3Al_5O_{12}$ (YAG) and Ce-doped $Y_3Al_5O_{12}$ via different sol–gel methods. *Journal of Materials Chemistry*, 9(12):3069–3079, 1999.

[92] N. Soleimani, B. Ponting, E. Gebremichael, A. Ribuot, and G. Maxwell. Coilable single crystals fibers of doped-YAG for high power laser applications. *Journal of Crystal Growth*, 393:18–22, 2014.

[93] C. Jing, J. Hou, and Y. Zhang. Fabrication of thick (>10 μm) Geo_2 ceramic films by a facile liquid phase deposition process. *Journal of the American Ceramic Society*, 90(11):3646–3650, 2007.

[94] K. V. K. Rao, S. V. N. Naidu, and L. Iyengar. Thermal expansion of rutile-type GeO, by the x-ray method. *Journal of the American Ceramic Society*, 51(8):467–468, 1968.

[95] B. Ferrand, B. Chambaz, and M. Couchaud. Liquid phase epitaxy: A versatile technique for the development of miniature optical components in single crystal dielectric media. *Optical Materials*, 11(2):101–114, 1999.

[96] C. D. McMillen, M. Mann, J. Fan, L. Zhu, and J. W. Kolis. Revisiting the hydrothermal growth of YAG. *Journal of Crystal Growth*, 356:58–64, 2012.

[97] R. A. Laudise and J. W. Nielsen. Hydrothermal crystal growth. In *Solid state physics*, volume 12, pages 149–222. Elsevier, 1961.

[98] C. M. Liu, J. C. Chen, C. H. Chiang, L.J. Hu, and S. P. Lin. Mg-doped sapphire crystal fibers grown by laser-heated pedestal growth method. *Japanese journal of applied physics*, 45(1R):194, 2006.

[99] C. L. Chang, S. L. Huang, C. Y. Lo, K. Y. Huang, C. W. Lan, W. H. Cheng, and P. Y. Chen. Simulation and experiment on laser-heated pedestal growth of chromium-doped yttrium aluminum garnet single-crystal fiber. *Journal of Crystal Growth*, 318(1):674–678, 2011.

[100] R. Simura, A. Yoshikawa, and S. Uda. The radial distribution of dopant (Cr, Nd, Yb, or Ce) in yttrium aluminum garnet ($Y_3Al_5O_{12}$) single crystals grown by the micro-pulling-down method. *Journal of Crystal Growth*, 311(23):4763–4769, 2009.

[101] C. H. Chun. Experiments on steady and oscillatory temperature distribution in a floating zone due to the marangoni convection. *Acta Astronautica*, 7(4-5):479–488, 1980.

[102] N. Dubnikova, E. Garskaite, A. Beganskiene, and A. Kareiva. Sol–gel synthesis and characterization of sub-microsized lanthanide (Ho, Tm, Yb, Lu) aluminium garnets. *Optical Materials*, 33(8):1179 – 1184, 2011.

[103] L. V. Soboleva and A. P. Chirkin. Y_2O_3-Al_2O_3-Nd_2O_3 phase diagram and the growth of $(Y,Nd)_3Al_5O_{12}$ single crystals. *Crystallography Reports*, 48(5):883–887, Sep 2003.

[104] M. E. Innocenzi, R. T. Swimm, M. Bass, R. H. French, and M. R. Kokta. Optical absorption in undoped yttrium aluminum garnet. *Journal of Applied Physics*, 68(3):1200–1204, 1990.

[105] M. Malinowski, Z. Frukacz, M. Szuflińska, A. Wnuk, and M. Kaczkan. Optical transitions of Ho^{3+} in YAG. *Journal of alloys and compounds*, 300:389–394, 2000.

[106] J. Caird and L. DeShazer. Analysis of laser emission in Ho^{3+}-doped materials. *IEEE Journal of Quantum Electronics*, 11(3):97–99, 1975.

[107] L. F. Johnson, J. E. Geusic, and L. G. Van Uitert. Coherent oscillations from Tm^{3+}, Ho^{3+}, Yb^{3+} and Er^{3+} ions in yttrium aluminum garnet. *Applied Physics Letters*, 7(5):127–129, 1965.

[108] K. Kitamura, S. Kimura, Y. Miyazawa, Y. Mori, and O. Kamada. Stress-birefringence associated with facets of rare-earth garnets grown from the melt; a model and measurement of stress-birefringence observed in thin sections. *Journal of Crystal Growth*, 62(2):351–359, 1983.

[109] J. C. Brice. Facet formation during crystal pulling. *Journal of Crystal growth*, 6(2):205–206, 1970.

[110] B. Raghothamachar, G. Dhanaraj, J. Bai, and M. Dudley. Defect analysis in crystals using x-ray topography. *Microscopy research and technique*, 69(5):343–358, 2006.

[111] X. R. Huang. LauePt, a graphical-user-interface program for simulating and analyzing white-beam x-ray diffraction laue patterns. *Journal of Applied Crystallography*, 43(4):926–928, 2010.

[112] J. A. Burton, R. C. Prim, and W. P. Slichter. The distribution of solute in crystals grown from the melt. part i. theoretical. *The journal of chemical physics*, 21(11):1987–1991, 1953.

[113] W. A. Tiller, K. A. Jackson, J. W. Rutter, and B. Chalmers. The redistribution of solute atoms during the solidification of metals. *Acta metallurgica*, 1(4):428–437, 1953.